Single-Atom Resolved Imaging and Manipulation in an Atomic Mott Insulator

Christof Weitenberg

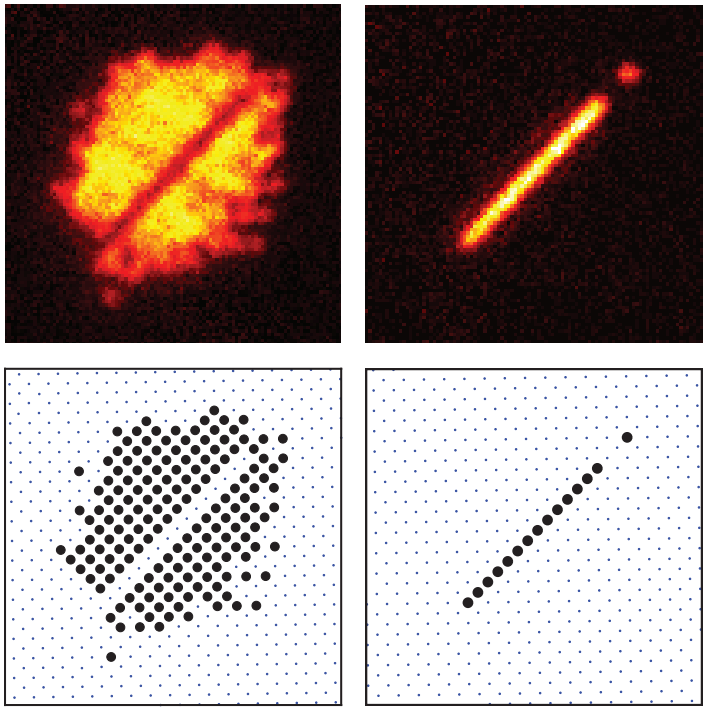

Dissertation der Fakultät für Physik
der Ludwig-Maximilians-Universität München

München, April 2011

Erstgutachter: Prof. Dr. Immanuel Bloch
Zweitgutachter: Prof. Dr. Walter Hofstetter

Tag der mündlichen Prüfung: 26. Mai 2011

Single-Atom Resolved Imaging and Manipulation in an Atomic Mott Insulator

Dissertation der Fakultät für Physik
der Ludwig-Maximilians-Universität München

vorgelegt von

Christof Weitenberg

geboren in Rhede

München, April 2011

Abstract

This thesis reports on new experimental techniques for the study of strongly correlated states of ultracold atoms in optical lattices. We used a high numerical aperture imaging system to probe ^{87}Rb atoms in a two-dimensional lattice with single-site resolution. Fluorescence imaging allows to detect single atoms with a large signal to noise ratio and to reconstruct the atom distribution on the lattice.

We applied this new technique to a two-dimensional Mott insulator and directly observed number squeezing and the emerging shell structure. A comparison of the radial density and variance distributions to theory provides a precise in situ temperature and entropy measurement from single images. We find entropies around the critical value for quantum magnetism.

In a second series of experiments, we demonstrated two-dimensional single-site spin control in the optical lattice. The differential light shift of a tightly focused laser beam shifts selected atoms into resonance with a microwave field driving a spin flip. In this way, we reach sub-diffraction limited spatial resolution well below the lattice spacing. Starting from a Mott insulator with unity filling we were able to create arbitrary spin patterns. We used this ability to prepare atom distributions to study one-dimensional single-particle tunneling dynamics in a lattice. By discriminating the dynamics of the ground state and of the first excited band, we find that our addressing scheme leaves most atoms in the vibrational ground state.

Moreover, we studied coherent light scattering from the atoms in the optical lattice and found diffraction maxima in the far-field. We showed that an antiferromagnetic order leads to additional diffraction peaks which can be used to detect this order also when single-site resolution is not available.

The new techniques described in this thesis open the path to a wide range of novel applications from quantum dynamics of spin impurities, entropy transport, implementation of novel cooling schemes, and engineering of quantum many-body phases to quantum information processing.

Zusammenfassung

In dieser Arbeit werden neue experimentelle Techniken für die Untersuchung von stark korrelierten Zuständen von ultrakalten Atomen in optischen Gittern vorgestellt. Wir untersuchen ^{87}Rb Atome in einem zwei-dimensionalen Gitter und erreichen dabei eine Auflösung der einzelnen Gitterplätze mit Hilfe eines hochauflösenden Abbildungssystems. Fluoreszenzabbildung erlaubt es, einzelne Atome mit großem Signal-zu-Rausch-Verhältnis zu detektieren und die Verteilung der Atome auf dem Gitter zu rekonstruieren.

Wir wenden diese neue Technik auf einen zwei-dimensionalen Mott-Isolator an and beobachten direkt das *number squeezing* und die Schalenstrukur. Ein Vergleich der radialen Dichte- und Varianzverteilung mit der Theorie ermöglicht eine präzise Temperatur- und Entropiemessung an einzelnen Bildern und wir finden Entropien um den kritischen Wert für Quantenmagnetismus.

In einer zweiten Reihe von Experimenten zeigen wir, dass wir gezielt einzelne atomare Spinzustände im Gitter manipulieren können ohne die benachbarten Atome zu beeinflussen. Wir benutzen den differentiellen *light shift* eines stark fokussierten Laserstrahls, um einzelne Atome in Resonanz mit einem Mikrowellenfeld zu bringen, das den Spin umklappt. Auf diese Weise erreichen wir eine Ortsauflösung unter der Beugungsgrenze. Wir beginnen mit einem Mott-Isolator mit einem Atom pro Gitterplatz und können darin beliebige Spinmuster erzeugen. Diese neuen Möglichkeiten zur Präparation atomarer Verteilungen nutzen wir, um die eindimensionale Einteilchen-Tunneldynamik in einem Gitter zu untersuchen. Wir unterscheiden die Dynamik von Atomen im Grundzustand und im ersten angeregten Band und zeigen so, dass unser Adressierschema die meisten Atome im Grundzustand lässt.

Darüber hinaus untersuchen wir kohärente Lichtstreuung an den Atomen im Gitter und finden Beugungsmaxima im Fernfeld. Wir zeigen, dass eine antiferromagnetische Ordnung der Atome zu zusätzlichen Beugungsmaxima führt, die man auch ohne unsere hohe Auflösung zum Nachweis dieser Ordnung nutzen könnte.

Die neuen Techniken, die in dieser Arbeit vorgestellt werden, öffnen den Weg für viele neue Anwendungen von der Quantendynamik von Spin-Defekten, Entropietransport, der Umsetzung neuer Kühlschemata sowie der Realisierung von Quanten-Vielteilchenphasen bis hin zur Quanteninformationsverarbeitung.

Contents

1 Introduction

Ultracold atoms in optical lattices are a versatile tool for the simulation of condensed matter systems. After the proposal [1] and the subsequent realization [2] of the Bose-Hubbard model with ultracold atoms, the field has attracted much attention [3, 4]. The paradigm is to use the atoms in the lattice as a quantum simulator for condensed matter physics in the spirit of Feynman's famous proposal [5] to use one well-controlled quantum system to simulate another quantum system. With ultracold atoms, one can implement simple model Hamiltonians, which contain the relevant physics, but are intractable on a classical computer.

To simulate a solid state system with ultracold atoms, one replaces the electrons by the ultracold atoms and the potential formed by the periodically spaced ions by an optical lattice potential. Although these systems are quite different in the absolute energy and length scales and in the details of the potentials, both can be described by the same models. The single band Hubbard model, for example, contains only the two parameters hopping rate and on-site interaction, which comprise all the details of the interactions and potentials. While the electrons in a solid state crystal are Fermions, the atoms in an optical lattice can either be bosonic or fermionic, depending on their spin.

Ultracold atoms in optical lattices have several experimental advantages over solid state systems. In the first place, they constitute a very clean and simple system without any lattice defects. Also the effective parameters in the model Hamiltonians can be calculated from first principles. A second advantage of ultracold atoms is their high degree of controllability not found in solid state crystals. The lattice parameters can be tuned dynamically and over a wide range. The interactions can be tuned via Feshbach resonances [6] and the internal states can be controlled to high precision. Also the time scales are much larger, usually in the range of milliseconds such that the dynamics becomes easily accessible.

Ultracold atoms currently face one major challenge: due to the much lower density, the energy scales for the atoms are much smaller than in solid state crystals. While the Fermi energy in real materials is on the order of a few thousand Kelvin, such that quantum phenomena can already be observed at room temperature, the typical energy scales for atoms in optical lattices are on the order of nanokelvin. This has so far prevented the observation of the interesting phases of antiferromangetic order and the d-wave superfluid. Novel cooling schemes to reach the required temperatures are under investigation [7, 8]

Spectacular experimental progress has been made in the last years, diversifying the field in many different directions. Fermionic atoms have been brought to degen-

eracy [9] and were used to produce a fermionic Mott insulator [10, 11]. Now the challenge is to realize the antiferromagnetic phase. In a reduced dimensionality, quantum fluctuations play a larger role leading to different physics like the Tonks-Girardeau gas in 1D [12, 13] and the Berezinskii-Kosterlitz-Thouless cross over in 2D [14]. The recent production of ultracold ground state molecules [15, 16] has opened the path to the study of long-range and anisotropic interactions in optical lattices. Disorder can lead to Anderson localization of a BEC [17] and its effect on the phase diagram of the Hubbard model is now under investigation [18–21].

Artificial magnetic fields have been produced both via rotation of the gas [22–24] and using a geometric phase [25]. They allow to simulate orbital magnetism and the quest is to reach the fractional quantum Hall regime [26, 27]. Superexchange dynamics were already observed in double-well optical potentials [28] and they can be used to simulate quantum magnetism in ultra cold gases [29]. First observations of classical magnetism have been made in different geometries [30, 31]. Ultracold atom have also been proposed to simulate very different kinds of physics like neutron matter in the outer crust of neutron stars [32] or color superfluidity and Baryon formation of quarks [33].

While it is state of the art to detect and manipulate single ions in an ion trap [34] or single atoms in separate dipole traps [35], the application of these techniques to the strongly-correlated regime of many-body states was so far lacking. The first experiments imaging or manipulating atoms in a lattice with single-site resolution used either large lattice spacings [36–39] or thermal atoms [40–42], which made these systems not suitable for the study of many body physics in the strongly correlated regime. Other experiments did not reach full single atom sensitivity [43, 44].

Only recently was single-atom resolved imaging in a Mott insulator achieved in the group of Markus Greiner [45, 46] and in our group [47]. These advances allow to probe strongly correlated states at the single atom level and to fully access the statistics. E.g., we can measurement density-density correlations, which are complementary to the first order correlations accessible with previous methods like time-of-flight imaging.

For the first time, we have shown the manipulation of the spin of single atoms in an optical lattice in the strongly correlated regime [48]. This new techniques opens the path to a wide range of novel applications from quantum dynamics of spin impurities and entropy transport to the implementation of novel cooling schemes.

Besides the quantum simulation aspect, ultracold atoms in optical lattices have also long been considered a promising candidate for quantum information processing due to their exceptionally long coherence times and the intrinsic scalability of the system. Using the clock states as the qubit, coherence times of 58 s have recently been demonstrated [49]. For the initialization of the quantum register, a Mott insulator state with exactly one atom per site in the vibrational ground state is an ideal starting point, which is confirmed by the clouds with extremely low defect density presented in this work.

Now the newly accomplished technique of single-site addressing brings the construction of a full universal quantum computer within reach, both in the circuit-based [50] and the one-way quantum computer architecture [51, 52]. The cluster state required for the later approach has already been demonstrated using entanglement via spin dependent lattices [53, 54] and the two-qubit quantum gates required for the former approach have seen many proposals [53, 55] and successful experimental realization in dipole traps [56, 57].

Outline

The remaining thesis is organized as follows: Chapter 2 gives a short introduction to the Bose-Hubbard model. A summary of the experimental sequence for the preparation of two-dimensional degenerate gases is given in Chapter 3. Chapter 4 describes the high-resolution imaging system and the fluorescence imaging technique which we apply in Chapter 5 to obtain single-site resolved images of Mott insulators, featuring the number squeezing and the shell structure. Chapter 6 explains our scheme for addressing the spin of single atoms in the lattice, which we use to study the single-particle tunneling dynamics in a lattice, described in Chapter 7. In Chapter 8 we investigate coherent light scattering from an atomic Mott insulator and show that it could be used to detect antiferromagnetic order even if single-site resolution is not available. Finally, Chapter 9 concludes the thesis and gives an outlook on experiments that become possible with the new techniques described in this work.

List of publications

The following papers have been published in refereed journals in the context of this thesis.

- **Single-atom-resolved fluorescence imaging of an atomic Mott insulator.**
  J. F. Sherson*, C. Weitenberg*, M. Endres, M. Cheneau, I. Bloch, S. Kuhr.
  Nature **467**, 68 (2010).
  *these authors contributed equally to this work

- **Single-spin addressing in an atomic Mott insulator.**
  C. Weitenberg, M. Endres, J. F. Sherson, M. Cheneau, P. Schauß, T. Fukuhara, I. Bloch, S. Kuhr.
  Nature **471**, 319 (2011).

- **Coherent light scattering from a two-dimensional Mott insulator.**
  C. Weitenberg, P. Schauß, T. Fukuhara, M. Cheneau, M. Endres, I. Bloch, S. Kuhr.
  Phys. Rev. Lett. **106**, 215301 (2011).

2 Bose-Hubbard physics with ultracold atoms

This chapter will give a short introduction to the Bose-Hubbard model and its implementation with ultracold atoms. A more detailed description can be found, e.g., in Refs. [58–62].

2.1 Bose-Hubbard model

The Hubbard model was originally developed in solid state physics to describe the behavior of the valence electron gas in the periodic lattice of the atoms [63]. A bosonic version was studied to describe the superfluid-to-insulator transition in liquid helium [64]. Finally, it was proposed that this Hamiltonian can be realized with interacting atoms in periodic potentials [1], which was subsequently realized [2]. Since then, mimicking condensed matter physics with ultracold atoms in optical lattice has become an active field of research [3, 4].

The Bose-Hubbard Hamiltonian $\hat{H}$ is written in terms of the annihilation and creation operators $\hat{a}_i$ and $\hat{a}_i^\dagger$ for particles localized at a lattice site i as

$$\hat{H} = -J \sum_{<i,j>} \hat{a}_i^\dagger \hat{a}_j + \sum_i (\epsilon_i - \mu)\hat{n}_i + \sum_i \frac{U}{2}\hat{n}_i(\hat{n}_i - 1), \tag{2.1}$$

where $\hat{n}_i = \hat{a}_i^\dagger \hat{a}_i$ is the number operator and $< i, j >$ denotes the sum over all next neighboring lattice sites. The Hamiltonian consists of three terms. The first term describes the kinetic energy given by the nearest neighbor hopping from site j to site i with the hopping rate $J/\hbar$. The second term describes an external potential with energy ϵ_i at site i and introduces the chemical potential μ which sets the particle number in a grand canonical description. The third term describes the on-site interaction energy with the energy U for each pair of particles at a site.

2.2 Implementation with ultracold atoms

The Hubbard Hamiltonian can be realized with ultracold atoms in optical lattices. The potential of a cubic optical lattice can be factorized and reduced to a one-dimensional problem. In each dimension, it has the form $V_{\mathrm{lat}}(x) = V_0 \cdot \sin^2(k_{\mathrm{lat}} \cdot x)$, where $k_{\mathrm{lat}} = 2\pi/\lambda_{\mathrm{lat}} = \pi/a_{\mathrm{lat}}$ is the wave vector of the lattice light of wavelength λ_{lat} and the depth V_0 is usually given in units of the recoil energy $E_r = (\hbar k_{\mathrm{lat}})^2/(2m)$ with the atomic mass m.

The periodic potential leads to a band structure in the energy spectrum and the eigenfunctions are delocalized Bloch waves with quasimomenta $|q| < \pi/a_{\mathrm{lat}} \cdot \hbar$. For experimentally achieved temperatures, one can restrict the description to the lowest band, and we do not introduce a band index here. The Bloch waves can be combined to form the localized Wannier functions $w(x - x_i)$ at site i as a new orthonormal basis.

Tight binding approximation

For sufficiently deep lattices, the Wannier functions are tightly localized and they have a significant overlap only with the Wannier function localized at the nearest neighboring lattice site. In the tight binding approximation, all overlap integrals but those between next neighboring sites are neglected.

The tunnel coupling J between next neighbors can then be obtained as the exchange integral

$$J = \int w^*(x - x_{i+1}) \left(\frac{-\hbar^2}{2m} \nabla^2 + V_{\mathrm{lat}}(x) \right) w(x - x_i) \mathrm{d}x. \tag{2.2}$$

In this approximation, it is directly related to the energy spectrum, which has a band width of $4J$ [58].

Ultracold atoms interact with a point-contact interaction quantified by the scattering length a_s. For two atoms localized on the same site with a wave function $w(x)$, the interactions lead to an energy shift U given by

$$U = 4\pi\hbar a_s/m \cdot \int |w(x)|^4 \mathrm{d}x. \tag{2.3}$$

Both J and U can be tuned by changing the lattice depth. In ultracold atoms, the ratio U/J can easily be changed over several orders of magnitude. There are also approximative formulas for U and J as a function of the lattice depth valid for deep lattices [59].

Limitations of the Bose-Hubbard description

Ultracold atoms in optical lattices are a nearly ideal realization of the Bose-Hubbard model. The restriction to the lowest band is well justified, because the vibrational spacing is one order of magnitude larger than the energies relevant for the dynamics. Only for very low lattice depths ($V_0 < 5\, E_r$) do tunneling processes to the second and third neighboring site play a role [58]. The interactions of ultracold atoms are very short ranged and the purely on-site interactions are an excellent approximation.

The calculation of J and U in Eqs. (2.2) and (2.3) use the single particle wave function $w(x)$. However, the interaction can induce a change of the wave function, which changes U and J. The changes in U have recently been precisely measured [65] and can be described by effective multi-body interactions.

2.3 Ground state of the Bose-Hubbard model

For the two limiting cases of $U \ll J$ (infinitely shallow lattices) and $U \gg J$ (infinitively deep lattices) the description of the ground state of the Bose-Hubbard model is simple. The cases correspond to a superfluid state and a Mott insulating state, respectively. We first discuss the homogeneous case, i.e. without an external potential.

Infinitely shallow lattice

Let N and N_{L} denote the total number of atoms and the total number of available sites, respectively. In the limit where the tunneling energy is much larger that the interaction energy, all the atoms are condensed in the Bloch wave with zero quasi-momentum

$$|\psi\rangle = \frac{1}{\sqrt{N!}} \left(\hat{a}^{\dagger}_{q=0}\right)^{N} |0\rangle \,, \quad \text{with} \quad \hat{a}^{\dagger}_{q=0} = \frac{1}{\sqrt{N_{\mathrm{L}}}} \sum_{i}^{N_{\mathrm{L}}} \hat{a}^{\dagger}_{i} \,. \tag{2.4}$$

When the atom number is large, this state becomes indistinguishable from a coherent state

$$|\psi\rangle = \exp\left(\sqrt{N}\hat{a}^{\dagger}_{q=0}\right)|0\rangle = \exp\left(\sqrt{\frac{N}{N_{\mathrm{L}}}} \sum_{i}^{N_{\mathrm{L}}} \hat{a}^{\dagger}_{i}\right)|0\rangle \,. \tag{2.5}$$

Since the operators $\hat{a}^{\dagger}_{i}$ commute at different lattice sites, the above state can be factorized into a product of identical local coherent states

$$|\psi\rangle = \prod_{i}^{N_{\mathrm{L}}} \exp\left(\sqrt{\frac{N}{N_{\mathrm{L}}}}\hat{a}^{\dagger}_{i}\right)|0\rangle_{i} \,. \tag{2.6}$$

The on-site number fluctuations of such a state are known to be Poissonian, with a mean value $\bar{n} = N/N_{\mathrm{L}}$ and a variance $\sigma^2 = \bar{n}$.

Infinitely deep lattice

We consider here a commensurate filling $n = N/N_{\mathrm{L}}$. Deep in the Mott regime (the so called atomic limit), the atoms are localized at the node of the lattice and the state of the system can be expressed as a product of local Fock states

$$|\psi\rangle = \left(\prod_{i}^{N_{\mathrm{L}}} (\hat{a}^{\dagger}_{i})^{n}\right)|0\rangle \,. \tag{2.7}$$

The mean occupation is $\bar{n} = n$ with a variance $\sigma^2 = 0$. The reduction of the variance compared to the Poissonian case is called number squeezing. Perfect number

squeezing is only expected for zero temperature and zero tunneling. A finite tunneling will lead to the coherent admixture of particle hole pairs and the number squeezing continuously changes between the two limiting cases. A finite temperature will also reduce the amount of number squeezing by inducing thermal excitations (see Sec. 5.4).

Phase transition

Between the above-mentioned two limits, there is a quantum phase transition from the superfluid state to the Mott insulating state occurring at a critical ratio $(U/J)_c$. This continuous quantum phase transition is driven by quantum fluctuations and also exists at zero temperature, when all thermal fluctuations are frozen out. For homogeneous conditions and a 2D simple square lattice, the transition is expected to occur at $(U/J)_c \simeq 16.4$ (see Ref. [66]), where small shifts of this critical value have been reported when the system is additionally exposed to an underlying harmonic trapping potential [67].

Influence of the confining potential

In the homogeneous case, a pure Mott insulating state will only be reached for a commensurate filling, i.e. an integer number of atoms per lattice cite, because any additional atoms can freely move on top of the incompressible phase. Fortunately, the situation is more favorable in real experiments which always have an external confining potential. In this case, the atoms can distribute over the lattice and change the local filling factor. The density is then locally pinned to integer values and a shell structure emerges [68].

One can describe the system in the local density approximation which assigns a local chemical potential $\mu_i = \mu - \epsilon_i$ to a site i with energy ϵ_i. If the external confinement varies slowly, the system will locally behave like a homogeneous system, however with a fixed chemical potential rather than atom number.

3 Experimental setup

Sixteen years after the first realization of a Bose-Einstein condensate (BEC) with ultracold gases [69, 70] there is now an impressive number of experiments with ultracold atoms and many descriptions of the apparatuses and techniques can be found (see e.g. Refs. [60, 62, 71, 72]). This chapter will give a short summary of our experimental sequence (Sec. 3.1) and detail on a few selected aspects (Sec. 3.2-3.5).

3.1 Experimental sequence

Our experimental setup consists of a steel vacuum chamber with two distinct regions, called the "MOT chamber" and the "science chamber" (see Fig. 3.1). A differential pumping stage connects the MOT chamber with a 2D-MOT chamber. In the MOT chamber, there is a pair of water-cooled gradient coils with the strong axis along the transversal direction. It is used both for the 3D-MOT and a magnetic quadrupole trap. Six MOT beams are aligned along the transversal, longitudinal and vertical direction.

In the science chamber, there are optical lattices along the x, y and z directions. The z lattice beam is reflected from the vacuum window, under which the high-resolution objective is situated. A single gradient coil is placed above the atoms and an additional pair of vertical offset coils is used to shift the position of the magnetic field zero close to the center of the chamber. An optical dipole trap along the longitudinal directions connects the MOT chamber and the science chamber. It has a wavelength $\lambda = 1064\,\mathrm{nm}$ and waist radius $w_0 = 40\,\mu\mathrm{m}$. The focus position can be moved along the optical axis to transport the atoms.

The experimental sequence is sketched in Fig. 3.2. It has a total duration of 22.5 s and consists of the following steps (the duration of each step is given in parenthesis).

1. **MOT phase** (2.3 s)
   We load the 3D-MOT from an atomic beam produced in the 2D-MOT (described in [73]). We end with $\sim 10^9$ atoms.

2. **Magnetic trap and microwave evaporation** (9.8 s)
   We load the atoms into the magnetic quadrupole trap by switching the field gradient to to 30 G/cm in 300 μs and then ramping it to 120 G/cm in 5 ms. We trap about 50% of the atoms in the $|F = 1, m_F = -1\rangle$ state without additional optical pumping. We apply a microwave evaporation knife (on the transition to $|F = 2, m_F = -2\rangle$) from -150 MHz down to -10 MHz, just before the onset of Majorana losses and end up with $\sim 10^8$ atoms at 20μK.

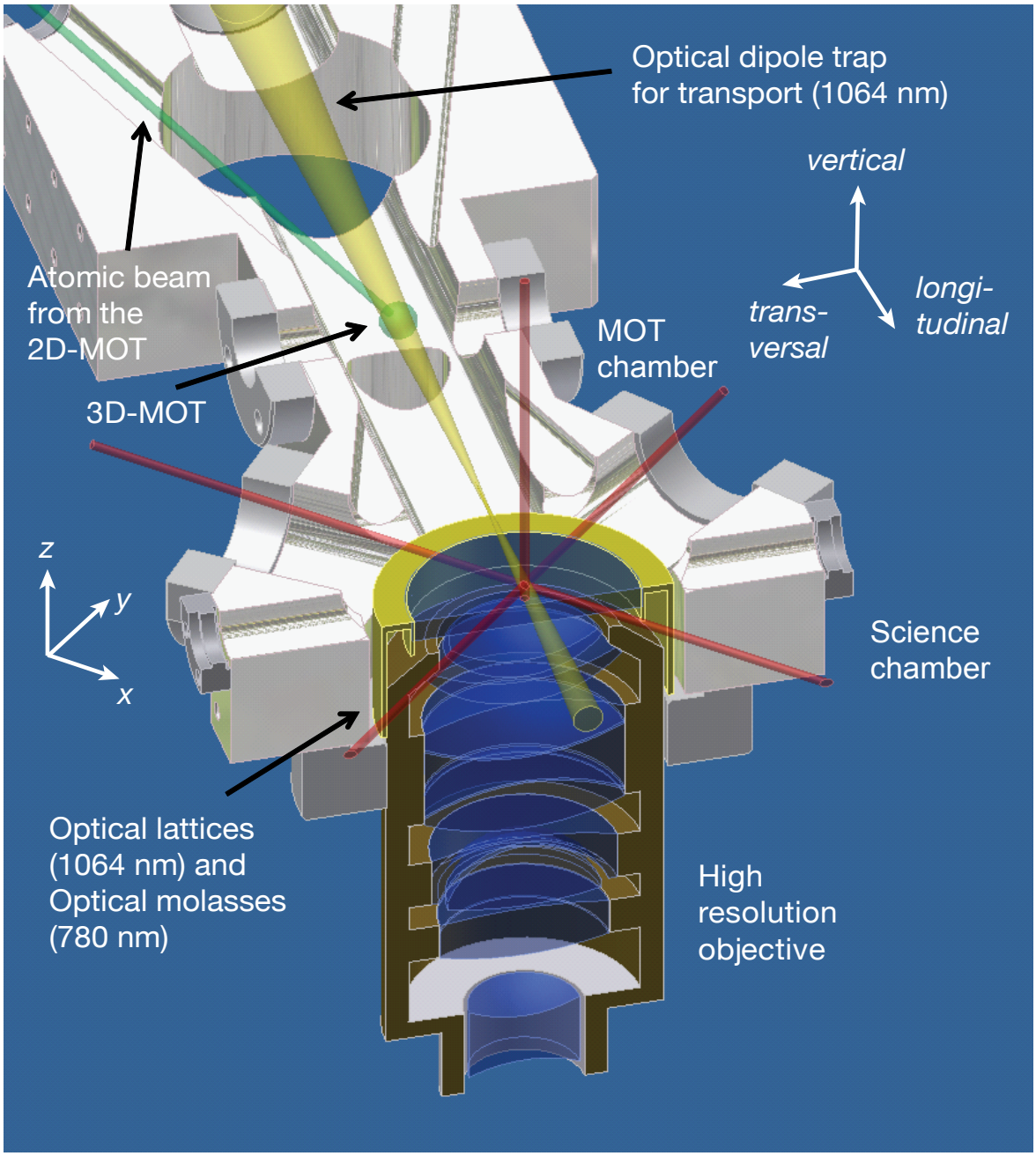

Figure 3.1: Schematics of the experimental setup. Shown is a cut through the vacuum chamber. In the front, one sees the science chamber with the optical lattices along the x, y and z direction (red) and the imaging system from below. The optical molasses and absorption imaging beams are superimposed with the lattice beams. Behind the science chamber, one sees the MOT chamber, which has MOT beams along the vertical, transversal and longitudinal directions (not shown). The 3D-MOT is loaded from an atomic beam (green) produced in a 2D-MOT in a separate vacuum chamber. An optical dipole trap along the longitudinal direction (yellow) is used for the transport from the MOT chamber to the science chamber.

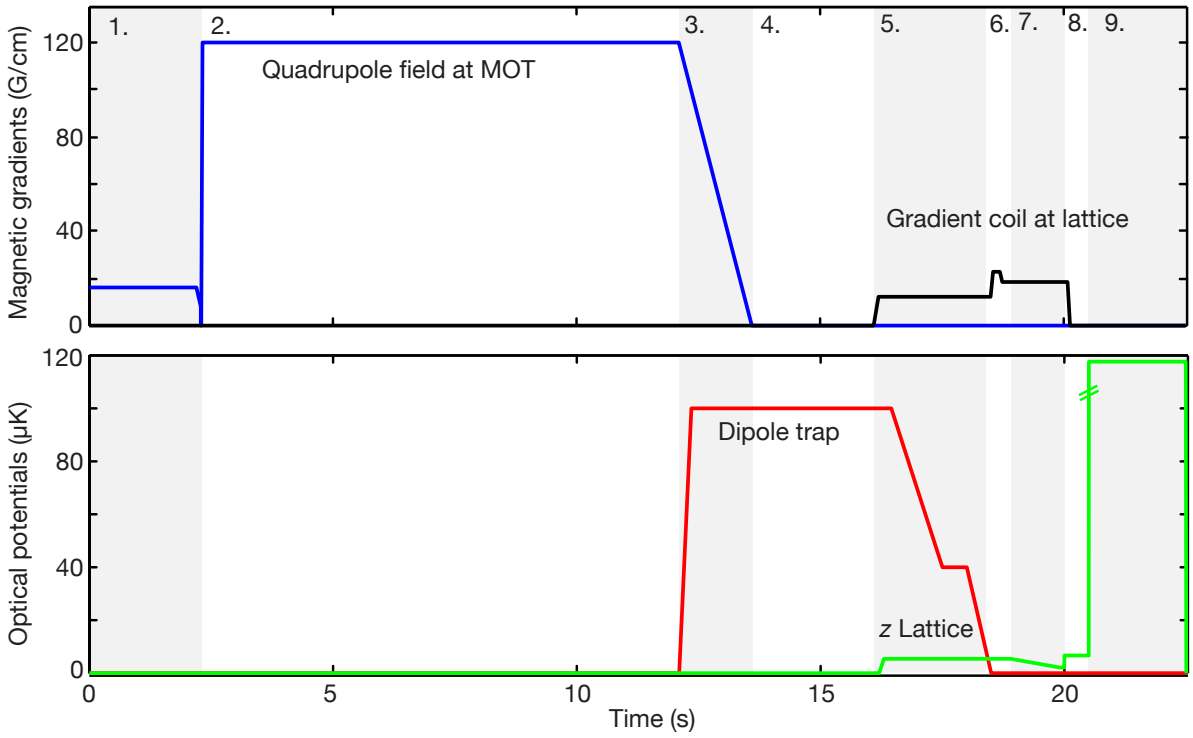

Figure 3.2: Schematics of the experimental sequence. Two exemplary magnetic field gradients and optical potentials are schematically shown. The gray shaded areas mark the division of the sequence as used in the main text.

3. **Loading of the optical dipole trap** (1.5 s)
   We position the optical dipole trap 350 μm below the position of the magnetic field zero and ramp it to a depth $U = k_B \cdot 100\,\mu$K in 250 ms. We load the dipole trap by slowly switching off the magnetic gradient within 1.5 s and end with $\sim 10^7$ atoms at $\sim 5\,\mu$K in the dipole trap.

4. **Optical transport** (2.5 s)
   We move the focus of the optical dipole trap from the MOT chamber to the science chamber within 2 s (see Sec. 3.2).

5. **Hybrid trap and evaporation** (2.3 s)
   We switch on a magnetic quadrupole field within 100 ms. The position of the magnetic zero is shifted $\sim$ 300 μm below the optical dipole trap and the field with a vertical gradient of 13 G/cm compresses the atom cloud in the axial direction of the dipole trap laser beam, which allows high collision rates. After 500 ms of evaporative cooling in this hybrid trap configuration [74, 75], we transfer the atoms into the z lattice and populate about 60 antinodes. We then evaporate again by ramping down the dipole trap intensity and finally switch

off the dipole trap. Now we have $\sim 10^5$ atoms in the vertical lattice.

6. **2D system preparation** (0.5 s)
   We prepare a single slice in the vertical lattice using magnetic resonance imaging techniques (see Sec. 3.3).

7. **Evaporation in z lattice** (1.1 s)
   We perform a final evaporation by ramping down the z lattice from $V_z = 54\,E_r$ to $V_z = 22\,E_r$ in 1 s while simultaneously tilting the potential along the horizontal direction with a magnetic field gradient. Then we move the cloud via the offset fields to a good overlap with the optical lattice. Depending on the end point of the evaporation, we are left with a few hundred to few thousand atoms in the degenerate regime in the $|F = 1, m_F = -1\rangle$ state.

8. **Horizontal lattices** (~ 0.5 s)
   We ramp up the x and y lattice depths in an s-shaped ramp of 75 ms to create a Mott insulator (see Ch. 5) and perform the desired experiment.

9. **Fluorescence imaging** (2.0 s)
   Finally we freeze the distribution by ramping all three lattices to $\sim k_B \cdot 300\,\mu$K depth in 2 ms and apply the push out pulse to remove the atoms from doubly occupied sites. We illuminate with an optical molasses and take a fluorescence image for 900 ms. Then we drop the atoms and record an image of the background light (see Ch. 4).

3.2 Optical transport

Most experiments with ultracold atoms in lattices use two separate regions for the MOT and for the lattices, because both require a large optical access. Often, the transport between the two regions is accomplished by moving the position of the zero of a magnetic field gradient either using many coil pairs [76, 77] or by translating a single pair of coils [78]. A different approach is to transport optically, either by moving the focus [79–81] or shifting the phase of an optical lattice [82, 83]. This has the advantage of stealing less optical access in the science chamber.

We transport the atoms in a single beam optical dipole trap (1064 nm, beam waist radius $w_0 = 40\,\mu$m, axial trap frequency 5 Hz at $k_B\,100\,\mu$K trap depth). The atoms are transported within 2 s by a distance of 130 mm by translating the focus position of the dipole trap using mirrors on a motorized micrometer stage (Newport Motion Controller XMS160, range 160 mm). We use a rather smooth transport profile, i.e. the focus position as a function of time, which is a concatenated polynomial continuous to third order and has a maximum velocity of 300 mm/s and a maximum acceleration of 2.5 m/s^2 [84]. The transport is slightly non-adiabatic with respect to the axial trapping frequency of 5 Hz and in this regime one expects to excite oscillations, whose

amplitude depend on the precise timing of the transport profile [81]. Although we see some influence of the parameters of our transport profile, the interpretation is not clear [84]. After transport we have an oscillation with an amplitude of $\sim 150\,\mu$m which is damped during the subsequent evaporation in the hybrid trap.

In previous experiments the lens which produces the focus of the dipole trap was placed on the translation stage [79]. We found that the alignment was easier if we put the lens before the stage and use the stage to change the length of the subsequent beam path by changing the position of a pair of retroreflecting mirrors. This also increases the travel range by a factor of two. We want to position the stage far away from the science chamber to avoid magnetic fluctuations at the position of the atoms. Therefore we image the focus of the dipole trap into the vacuum chamber with a 1:1 telescope. One of the last mirrors before the chamber is piezo driven and smoothly changed from one position to another during the optical transport. This allows for an independent alignment of the transversal dipole trap position at the position of the MOT and the science chamber.

3.3 Preparation of 2D systems

In an optical lattice it is straight forward to reduce the dimensionality by making one or two lattice axes deep and thereby freezing the dynamics in these directions [85]. This amounts to working with many copies of the lower-dimensional system. For the imaging, however, we need a single two-dimensional system, and two different approaches have been established for its preparation.

One approach is to compress the atom cloud either magnetically [86] or optically using a light sheet [87, 88] or an evanescent wave surface trap [89, 90]. To allow the resulting high atomic densities, one can reduce the repulsive interactions via a Feshbach resonance in this step [91]. The compressed cloud can then optionally be loaded into a single antinode of an optical lattice with a few μm spacing [14, 90, 91].

Another approach is to first populate several antinodes of an optical lattice and to subsequently prepare a single slice out of it using magnetic resonance imaging techniques. For lattice spacings around 400 nm, a resolution of about 2 lattices sites has been reached for degenerate samples [68, 92] and single atoms [41, 93].

We implement this second approach, because the geometry of our chamber neither allows a larger lattice spacing (via an angle between the two vertical lattice beams) nor sufficient access to create a tightly focused light sheet. This preparation has the advantage that we can in principle create three-dimensional clouds and observe them tomographically after freezing them. Using a vertical lattice with a small spacing of 532 nm also ensures that the extension of the atomic wave packet in the direction of the imaging system (<100 nm) is much smaller than the depth of focus of our imaging system ($\Delta z = 1.7\,\mu$m). If this condition was not fulfilled we might have faced a reduction of the imaging resolution and of the addressing fidelity.

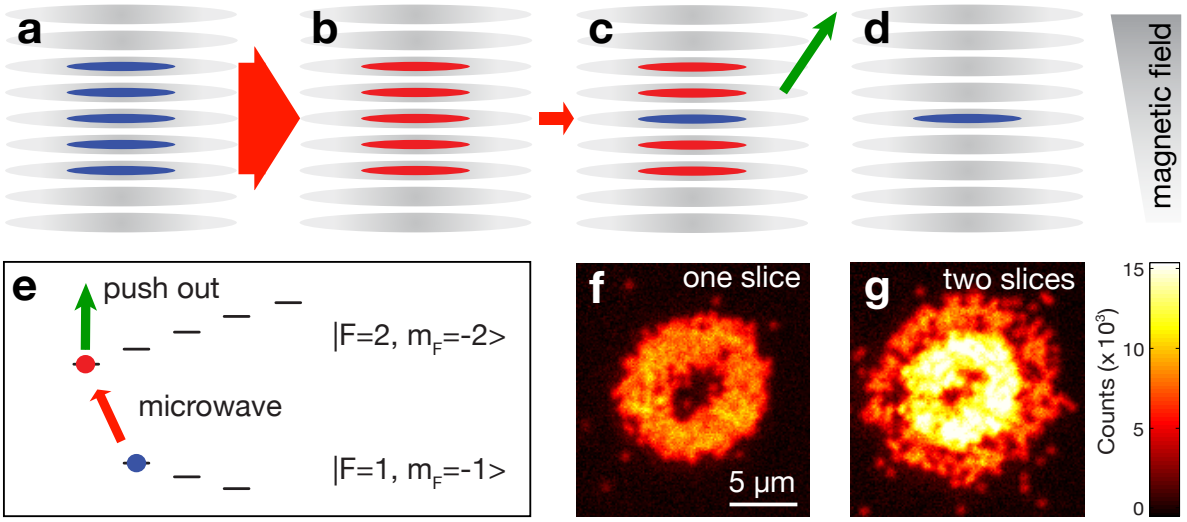

Figure 3.3: Preparation of 2D systems. (a) We initially populate many antinodes of the vertical lattice (gray ellipses) with atoms in state $|F = 1, m_F = -1\rangle$ (blue ellipses). (b) We transfer all atoms to the state $|F = 2, m_F = -2\rangle$ (red ellipses) with a global microwave sweep (indicated by the red arrow). (c) We transfer a single slice back to the state $|F = 1, m_F = -1\rangle$ making use of a magnetic field gradient to spectrally address a single slice. (d) We remove all atoms in the $F = 2$ manifold with an optical push out pulse on the $F = 2$ to $F' = 3$ transition (green arrow) and are left with atoms in a single slice. (e) Level scheme of the ground state manifold of ^{87}Rb. The states that we use for the slicing are indicated. (f) Image of a Mott insulator in a single slice. (g) Image of a two Mott insulators in two neighboring slices. It is clearly visible that signal rises to twice the value of a single slice when the two Mott insulators of different radii overlap.

The slicing procedure is illustrated in Fig. 3.3. We start with all atoms in $|F = 1, m_F = -1\rangle$, populating 60 antinodes of the vertical lattice with a spacing of $a_{\text{lat}} = 532\,\text{nm}$. We then transfer all atoms to $|F = 2, m_F = -2\rangle$ and subsequently transfer a single slice back to $|F = 1, m_F = -1\rangle$. The selective transfer is possible due to a magnetic field gradient producing a position dependent frequency shift $\partial\nu/\partial z \sim 5\,\text{kHz}/\mu\text{m}$ of the $|F = 1, m_F = -1\rangle \leftrightarrow |F = 2, m_F = -2\rangle$ transition. The atoms in $|F = 2, m_F = -2\rangle$ are then removed with an optical push out pulse.

The first transfer from $|F = 1, m_F = -1\rangle$ to $|F = 2, m_F = -2\rangle$ is performed by a microwave frequency sweep of 20 ms over 10 MHz. We additionally apply an optical repumping pulse to completely empty the $|F = 1\rangle$ manifold. The selective transfer of the atoms of one slice back to the $|F = 1, m_F = -1\rangle$ state is done by a resonant Blackman pulse of 5 ms duration. We remove all atoms remaining in $F = 2$ from the trap by a laser pulse resonant with the $F = 2 \rightarrow F' = 3$ transition. A microwave sweep of 50 ms duration and 75 kHz spectral width is used to bring any remaining atoms in $|F = 1, m_F = 0\rangle$ to $|F = 2, m_F = 0\rangle$ before removing them with a laser pulse.

The magnetic field gradient $\partial B/\partial z = 24\,\mathrm{G/cm}$ is produced by a single coil placed 50 mm above the atoms with its axis coinciding with the z-lattice beam. The vertical bias field which we usually use to shift the position of the magnetic zero close to the atoms is completely switched off to avoid noise. The bias field from the single gradient coil at the position of the atoms is then 32 G. The current supply for the gradient coil is switched to an external noise free reference during the slicing procedure. We use a current supply with a relative stability of 10^{-5} (High Finesse bipolar current source BCS 5/5). This corresponds to magnetic field fluctuations of 0.3 mG which is of the same order as typical background magnetic field noise. Before the optical push out, we ramp the magnetic fields to the configuration for the subsequent evaporation which yields a smaller field at the position of the atoms.

As we subsequently perform an evaporation in the single 2D system, we are not sensitive to efficiency of the slicing transfer or to heating. Temperature drifts of the gradient coil are important and we monitor them and give a feedback on the microwave frequency for the slicing.

One can estimate the number of populated antinodes of a vertical lattice by observing the interference pattern of the degenerate atoms after time-of-flight, where the absence of an interference indicates a single 2D system [14, 90, 91]. In our case, a second slice is directly visible in the *in situ* fluorescence images [Fig. 3.3(f),(g)].

We found that we can prepare single slices, but we have large scatter in the vertical position of the sliced cloud and in the final atom number. Recent investigations suggest that we actually prepared two slices and lost all atoms in the smaller slice by a strong nonlinearity in the subsequent evaporation. Since then we made some improvements in the sequence which also involve a water cooled gradient coil and a larger magnetic gradient, and we can now prepare the same atom number with good stability. These improvements will be described in the thesis of Manuel Endres.

3.4 Optical lattices

We use a conventional optical lattice setup with three pairs of beams, each interfering with its own reflection. The vertical lattice is reflected from the vacuum window located 5 mm below the atoms and has its waist position at the window. The horizontal lattice beams are imaged to the retro-reflecting mirror with a lens of focal length $f = 120\,\mathrm{mm}$, making the lattice position insensitive to tilting vibrations of the mirror.

After studying the Bose-Hubbard physics at a lattice depth of a few E_r, we freeze the distribution for the fluorescence imaging by ramping the lattices to a depth of about $k_B \cdot 300\ \mu\mathrm{K} = 3000\,E_r$. In order to obtain such a large depth, we chose a relatively small focus size ($1/e^2$ waist radius of 75 μm) and bring a power of 10 W per axis to the atoms. We apply an intensity stabilization only up to a depth of$\sim 50\,E_r$.

The very deep lattices allow a convenient method for the alignment of the lattices onto the atoms. After switching off the potential, we apply a short pulse of a hori-

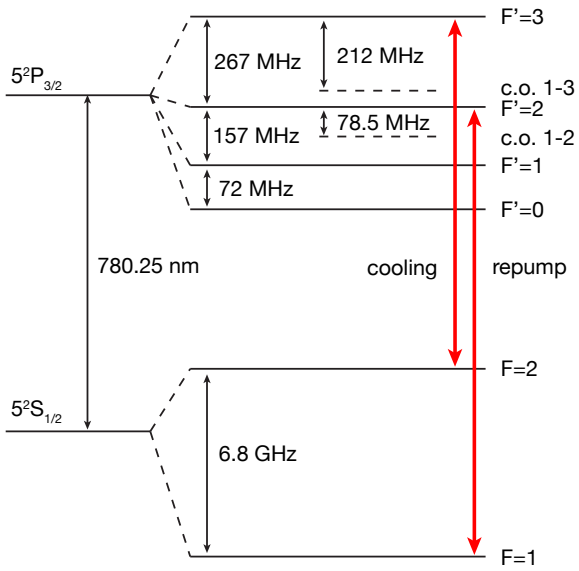

Figure 3.4: Level scheme of ^{87}Rb showing the hyperfine states of the $5^2S_{1/2}$ state and the $5^2P_{3/2}$ state [94]. The transitions that we use for cooling and for repumping are indicated. Also the cross overs to which we lock our lasers are shown.

zontal lattice beam (the retro-reflection is blocked), where the length corresponds to one fourth oscillation period of the trapping frequency in the lattice beam (typically 500 μs). In this time an initial transversal displacement between the atom position and the lattice beam will transform to a velocity which is subsequently probed by an image after time-of-flight. If the alignment is good, the atom cloud will expand symmetrically after this pulse. If the lattice beam is transversally displaced with respect to the atoms, one can deduce the direction of the displacement from the asymmetric expansion of the atom cloud. This is a very sensitive single-shot method which is insensitive to atom number fluctuations.

3.5 Laser setup

The level scheme of ^{87}Rb is sketched in Fig. 3.4 together with the wavelength of the cooling and repumping transition. It also shows the cross overs to which we lock some of our lasers (see below).

Low-power lasers

Our low power laser system is sketched in Fig. 3.5. All lasers are grating-stabilized diode lasers (Toptica DL-PRO). The laser system supplies the 2D-MOT, the 3D-MOT, the optical molasses at the position of the lattice and the addressing beam. We also

have absorption imaging beams superimposed with the MOT beams and the lattice beams. The following letters refer to the subfigures in Fig. 3.5.

(a) The master laser provides the image beam [via a double-pass acousto-optical modulator (AOM)] and the push beam of the 2D MOT [73]. It is stabilized to the 1-3 cross over using a Pound-Drewer-Hall lock.

(b) The repump laser for the two MOTs and for the absorption imaging is locked to the 1-2 cross over and shifted into resonance with the $F = 1$ to $F' = 1$ transition using an AOM. As the beams are not needed simultaneously, we extract the image repumper from the zeroth order of the first AOM.

(c)-(d) The cooling light for the two MOTs and the molasses is obtained from two tapered amplifiers which are both offset locked to the master. A half-wave plate can be placed into the beam path to switch the power between the 3D-MOT and the molasses at the lattices at the subsequent polarizing beam splitter cube (PBS).

(e) The addressing laser is not frequency stabilized and monitored with a wave meter. We can send a molasses beam through the same beam path (see Sec. 6.5).

(f) For the offset lock, the cooling light and the master laser are combined on a 50:50 splitter after spatial filtering via an optical fiber. The beam signal is recorded via a fast photo diode (Hamamatsu MSM Photodetector).

(g) The image beam is distributed over the different imaging ports. Repumping is done in the vertical direction at the position of the MOT and in longitudinal direction at the position of the lattice. We use one fast shutter to switch the imaging on and off (Uniblitz Eletronic). More shutters in front of each fiber coupling serve to select the desired imaging direction.

(h) The molasses light is distributed over the x,y, and z direction and can also be sent to the addressing port. The AOMs are controlled by phase-locked waveform generators such that we can give controlled relative detunings to the molasses beams (see Sec. 4.5).

High-power lasers

For the horizontal optical lattice laser beams we used two fiber amplifiers (Nufern, 40W) seeded with the same single-frequency solid-state laser (Innolight Mephisto product line 1064nm, 500mW), whereas the vertical lattice beam was derived from an independent solid-state laser (Innolight Mephisto MOPA product line 18W). For the optical dipole trap, we use a broad-band fiber laser (IPG photonics Ytterbium fiber laser 50 W, 1064 nm, emission bandwidth 5 nm, operated at 7 W). All high power lasers are send through polarization maintaining photonic crystal fibers (ams Technologies) between the AOM and the experiment. This avoids thermal drifts of the beam position from the AOMs. In order to avoid thermal destruction of the fibers, we use a duty cycle limiter on the AOM that ensures that the optical power reaches the fiber for not more than 1 s every 20 s.

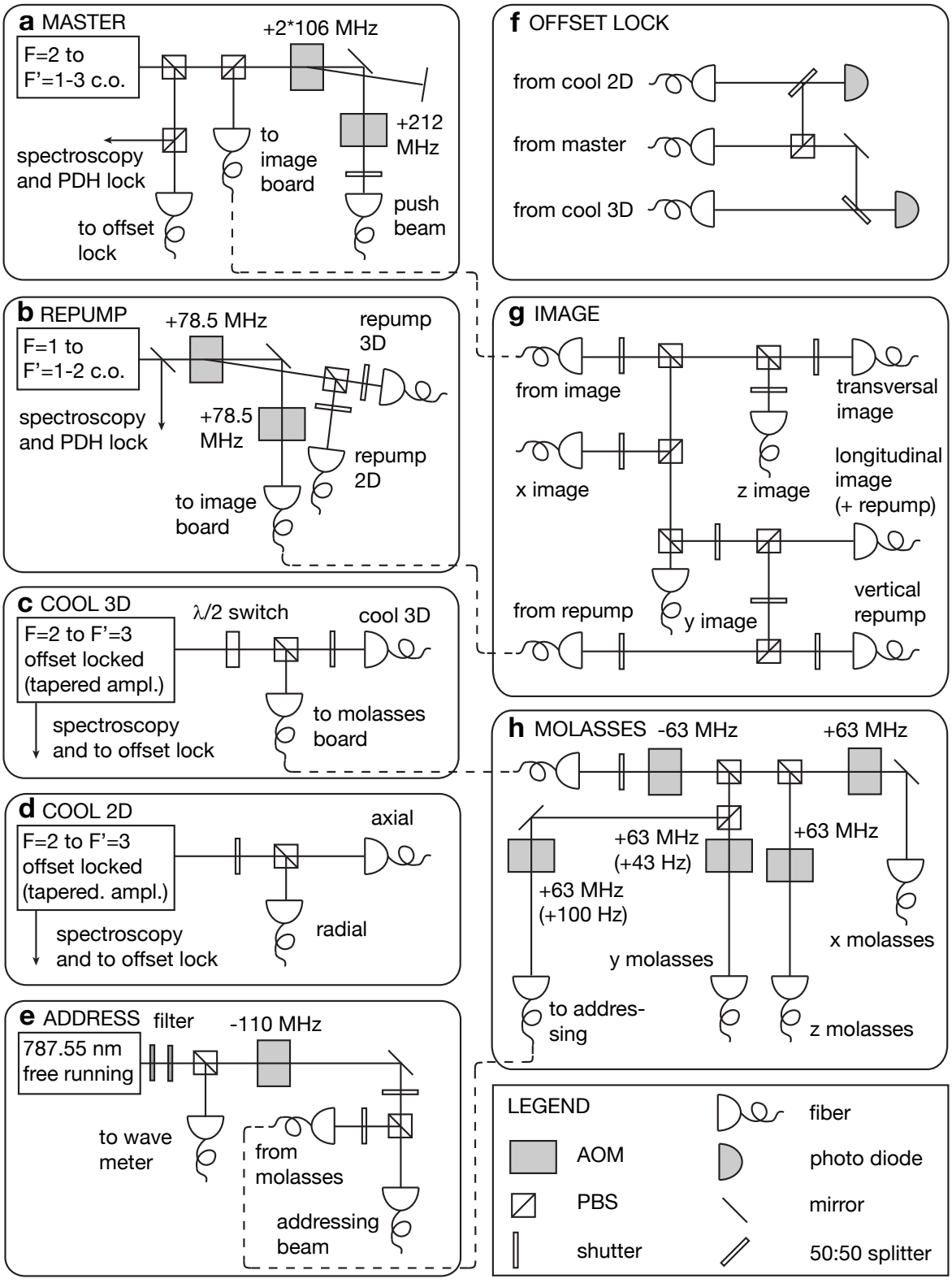

Figure 3.5: Schematic of the laser setup. For details see main text.

4 Single-atom resolved fluorescence imaging

This chapter describes how we image the quantum gases in the optical lattice with single-site resolution and single-atom sensitivity. We combine fluorescence imaging with a high numerical aperture objective (Sec. 4.2). One drawback of fluorescence imaging are the light-assisted collision, which lead to the rapid pair-wise loss of atoms, such that we detect the parity of the original atom distribution per lattice site (Sec. 4.3). Because we only have to distinguish between one or zero atom per lattice site, we can reconstruct the atom distribution even with a resolution above the Rayleigh criterion. We developed a deconvolution algorithm, which tries different atom configurations and reconstructs the distribution with very high fidelity (Sec. 4.4). The fidelity is limited by the loss of atoms during the imaging time due to background collisions and thermal hopping events in the molasses. Optimization of the molasses parameters can largely suppress this thermal hopping (Sec. 4.5). We discuss possible extensions of the imaging technique (Sec. 4.6) and conclude in Sec. 4.7.

4.1 State of the art

Fluorescence imaging is the method of choice for reaching single atom sensitivity, because it yields a large signal-to-noise ratio and atoms can be simultaneously cooled by an optical molasses. The method was demonstrated for imaging single atoms in optical dipole traps [35], and in optical lattices [38, 95].

However, it remained a challenge to apply it to systems in the strongly correlated regime. Strong correlations require sufficiently large tunneling rates between the lattice sites, which can compete with the technical heating rates to allow an adiabatic ramp up of the lattices. As the tunneling rate is exponentially suppressed with the lattice spacing, the latter has to be on the order of 0.5 μm, which is challenging to optically resolve. In the case of rubidium, Mott insulators were so far created with lattice spacings of $\sim$ 426 nm [2, 96], 532 nm [97], 680 nm [46], and with a rectangular lattice with spacings 765 nm and 426 nm [98]. Larger spacings might be possible for lighter elements, especially lithium [99].

The first experiments with fluorescence imaging worked either in a 3D lattice of 5 μm spacing [38], where tunneling is completely suppressed, or with sparse filling in a 1D lattice with short spacing [42, 95]. In this 1D lattice, nearest neighbor detection at a spacing of 433 nm was reached despite the diffraction limited resolution of 1.8 μm by using an algorithm, which makes use of the discreteness of the spacing and of the dilute filling [42].

An alternative approach demonstrated in the group of Herwig Ott is to apply scanning electron microscopy to ultracold gases, which allows a resolution down to 150 nm, well resolving a lattice of 600 nm spacing [43]. As the electron beam is scanned across the sample, the atoms are ionized by electron impact ionization, extracted with an electrostatic field and subsequently detected by an ion detector. The method, however, does not reach full single-atom sensitivity, because impact ionization constitutes only about 40% of the scattering events, and averaging over many images is required so far.

Absorption imaging has been used for *in situ* imaging of two-dimensional systems with a resolution of 3-4 μm [91] and 1.2 μm [39]. The former experiment achieved detection of the shell structure of a Mott insulator and the latter resolved lattice sites with 2 μm spacing, with a weak tunnel coupling. However, absorption imaging has not reached single-atom sensitivity so far.

Only recently was the technique of single-atom sensitive fluorescence imaging combined with single-site resolution in a short-period lattice in the group of Markus Greiner [45].The atoms were placed in a surface trap a few micrometer below a hemispheric lens, and the solid immersion effect lead to an effective numerical aperture of NA $= 0.8$ for an objective with NA $= 0.55$ outside the vacuum chamber. Thus the lattice spacing of 680 nm could be well resolved at a resolution of 600 nm (FWHM). The horizontal lattices were generated by projecting a holographic mask through the imaging system. This allowed to change the lattice wavelength for the imaging and obtain the required lattice depth with a convenient laser power. However, the proximity to the surface seems to cause problems in the homogeneity of the potentials [46]. Finally, single-atom-resolved images of Mott insulators were obtained in the group of Markus Greiner [46] and in our group [47]. This will be described in Ch. 5.

4.2 High-resolution imaging system

Imaging resolution

Due to its finite aperture, an imaging system can only reproduce a limited range of spatial frequencies of the object. Because the system is linear, the imaging system can be completely characterized by the response to a point source, the so called point spread function (PSF). It has the form of an Airy pattern, the width of which is determined by the wavelength and the aperture of the imaging system NA $= n \sin\alpha$. Here, α is the half opening angle and n is the refractive index between the object and the imaging system. The intensity distribution of the airy pattern is given by (see e.g. Ref. [100])

$$I(\rho) \propto \left(\frac{2J_1(\rho)}{\rho} \right)^2, \tag{4.1}$$

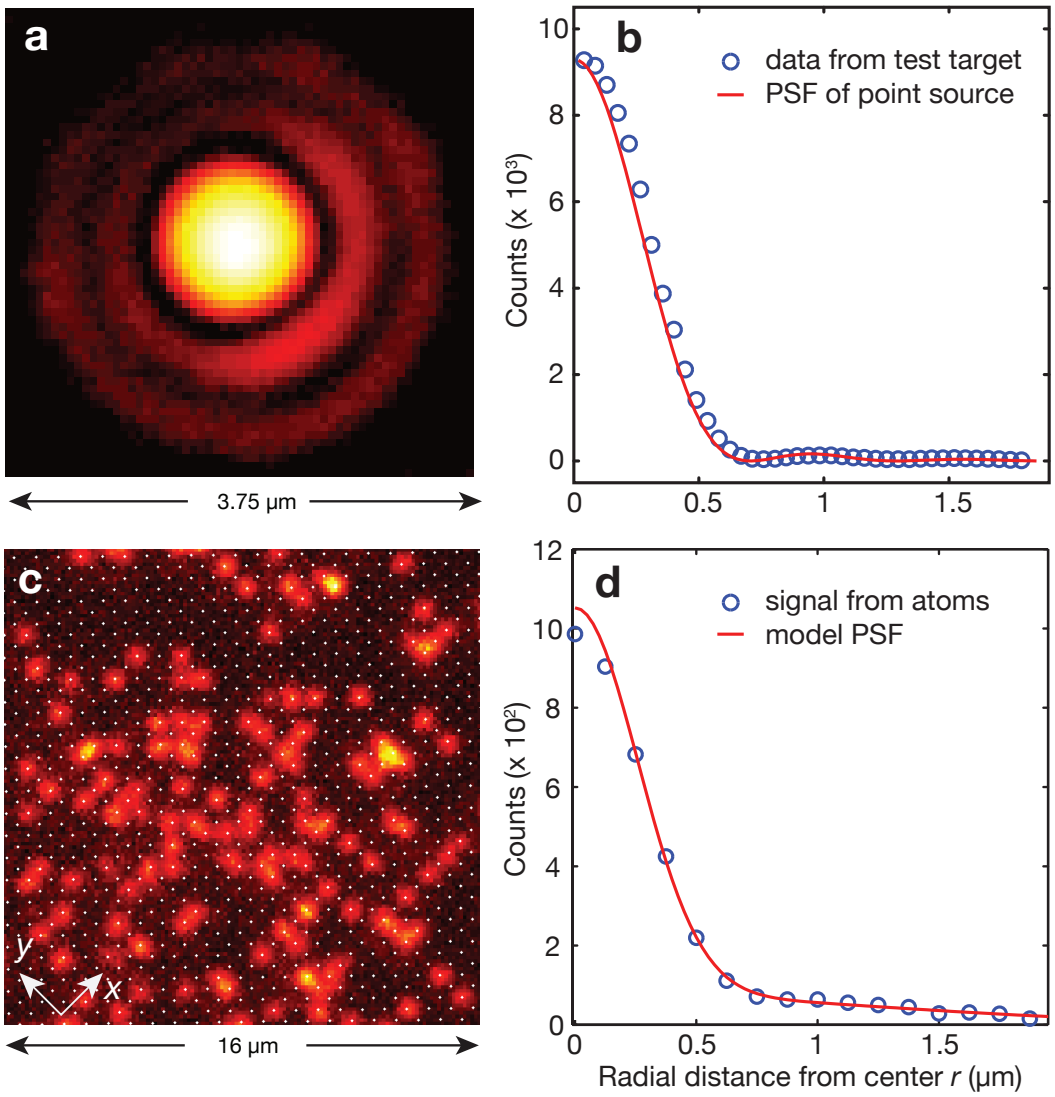

Figure 4.1: Point-spread function of the imaging system. (a) image of a single hole in the test target. Two of the rings of the Airy pattern can be distinguished. In the test setup, we used a camera with a pixel size of 8 μm, which corresponds to 62 nm in the object plane. (b) azimuthal average of the data in (a) together with an Airy pattern as given by Eq. (4.1) with a resolution of $r_0 = 700$ nm as expected from the numerical aperture NA $= 0.68$ of the imaging system (red line). The experimental data points (blue circles) lie somewhat outside the theoretical curve due to the finite size of the hole (≈ 100 nm). (c) Fluorescence image of a dilute cloud of atoms. The white dots mark the lattice sites. The individual atoms are well distinguishable. (d) Azimuthal average of our experimentally obtained point spread function of a single atom. The data was obtained by averaging over 68 signals of single atoms. The red line is a fit with the double Gaussian of Eq. (4.2).

where $J_1(\rho)$ is the Bessel function of first order and $\rho = r \cdot 3.795/r_0$ is the radial distance r scaled by the resolution r_0 and a numerical factor. The Rayleigh resolution is defined as the first zero of $I(\rho)$ and is linked to the numerical aperture via $r_0 = 1.22 \cdot \lambda/(2\mathrm{NA})$. Fig. 4.1(b) shows the PSF of a point source for our numerical aperture of NA $= 0.68$ and an imaging wavelength of $\lambda = 780\,\mathrm{nm}$ (red line), which yields $r_0 = 700\,\mathrm{nm}$.

The Rayleigh criterion states that point sources can be discriminated, if the maximum of one PSF coincides with the first zero of the other PSF, i.e. if their distance is r_0. By this definition, we do not have single-site resolution for our lattice spacing of $a_{\mathrm{lat}} = 532\,\mathrm{nm}$. However, the actual resolution can be well below this diffraction limit, if additional information is given [42, 101], such as the discrete nature of atoms and the lattice structure.

As the atoms sit on their lattice sites, it is not necessary to determine their position, but only to determine the occupation of each lattice site. Furthermore, there can be only zero or one atom per lattice site due to the light-induced collisions (Sec. 4.3). Therefore it is sufficient to have an imaging resolution that is able to differentiate zero or one atom per lattice site. It would be much harder to discriminate between more atom numbers. The requirement for the optical resolution in this context is to resolve a missing atom within a full shell and for this we should compare the resolution to twice the lattice spacing. This argument holds only for a large signal to noise, where the PSF of each atom is well formed on the camera chip. We describe in Sec. 4.4 how we determine the position of the lattice sites and reconstruct the atom distribution on the lattice.

The above considerations assume incoherent light, and in fact, imaging with coherent light can reduce the resolution [102]. Here, fluorescence imaging has an advantage over absorption imaging. Both methods rely on the scattering of photons by the atoms, but in absorption imaging, the usually coherent incident beam with the resulting shadow is imaged, while in fluorescence imaging only the scattered photons are imaged, and they can lose their coherence via inelastic scattering. In Ch. 8 we show that the coherent power fraction scattered into the objective is just a few percent.

We use the 5S-5P transition at $\lambda = 780\,\mathrm{nm}$ for imaging. Using the 5S-6P transition at the wavelength of $\lambda = 420\,\mathrm{nm}$ instead would allow a much better resolution of 370 nm. However, it is not clear if the sub-Doppler molasses (Sec. 4.5) will work on this transition.

Experimental setup

Our microscope objective was custom made (Leica Microsystems) and is located outside the vacuum chamber with a working distance of 13 mm. It is optimized for the wavelength range of 420 nm to 780 nm and has a numerical aperture of NA $= 0.68$ for $\lambda = 780\,\mathrm{nm}$ and NA $= 0.70$ for $\lambda = 420\,\mathrm{nm}$. It is diffraction limited with a Strehl of 97%. The camera (iXon$^{\mathrm{EM}}$+ 897 (back-illuminated), ANDOR Technology) has a

quantum efficiency of 80% and is cooled to $-70^{\circ}C$ in order to reduce dark counts. The beam path is sketch in Fig. 4.2. The objective covers 13% of the solid angle and the total transmission of the imaging system including the mirrors and filters is 63%. Including the quantum efficiency of the camera, we thus detect 7% of the scattered photons at the camera.

The imaging system consists of the objective with effective focal length of 5.19 mm and an achromatic lens with focal length 675 mm, yielding a magnification of 130. Thus the camera pixel size of 16 μm corresponds to 123 nm in the object plane, which is a reasonable value, since it does not limit the resolution and at the same time avoids distribution of the signal on too many pixels. Interference filters serve for the suppression of the light from the vertical lattice. An uncoated glass window in the beam path allows to send beams through the objective in reverse direction, e.g. a molasses beam (Sec. 4.5) or the addressing beam (Ch. 6).

The objective was tested separately from the main experimental setup using a test target with small holes, which was illuminated from the back [103]. The holes were spaced irregularly in order to avoid the Talbot effect with the spatially coherent light [104, 105]. The measured PSF from the test setup agreed with the specified imaging resolution, taking into account the finite size of the holes [see Fig. 4.1(a),(b)]. The objective is placed on a positioner (PIFOC P-726, Physik Instrumente GmbH & Co. KG, Karlsruhe), which allows to move it along the optical axis over a range of 100 μm with a precision of 10 nm.

The placement of the objective outside the vacuum chamber poses stringent requirements on the flatness of the vacuum window. Over a region of 15 mm the deformations must be smaller than $\lambda_t/4$ ($\lambda_t = 655$ nm is the test wavelength). This excludes spherical deformations, which can be compensated by refocussing the objective. We measured the deformations with a Fizeau interferometer (PTI 250 ZygoLOT, 50 mm aperture) and found 0.15 λ_t, which degraded to 0.22 λ_t after baking of the vacuum chamber.

Point spread function of a single atom

An essential step for developing a reconstruction algorithm is the precise knowledge of the point spread function of a single atom. It can be determined from fluorescence images of a dilute atomic cloud [see Fig. 4.1(c)]. We summed the fluorescence signal of many individual atoms that were isolated from their neighbors by more that 12 pixels. The summed image is almost radially symmetric and we computed an azimuthal average [see Fig. 4.1(d)]. We found that our PSF can be well approximated by a double Gaussian:

$$PSF(x,y) = C\left[(1-a)\exp\left(-0.5(x^2+y^2)/\sigma_1^2\right) + a\exp\left(-0.5(x^2+y^2)/\sigma_2^2\right)\right] \quad (4.2)$$

with widths σ_1, σ_2 and a parameter a describing the relative amplitudes. The maximum fluorescence level C varies from day to day and is in the range of 800-1200 counts.

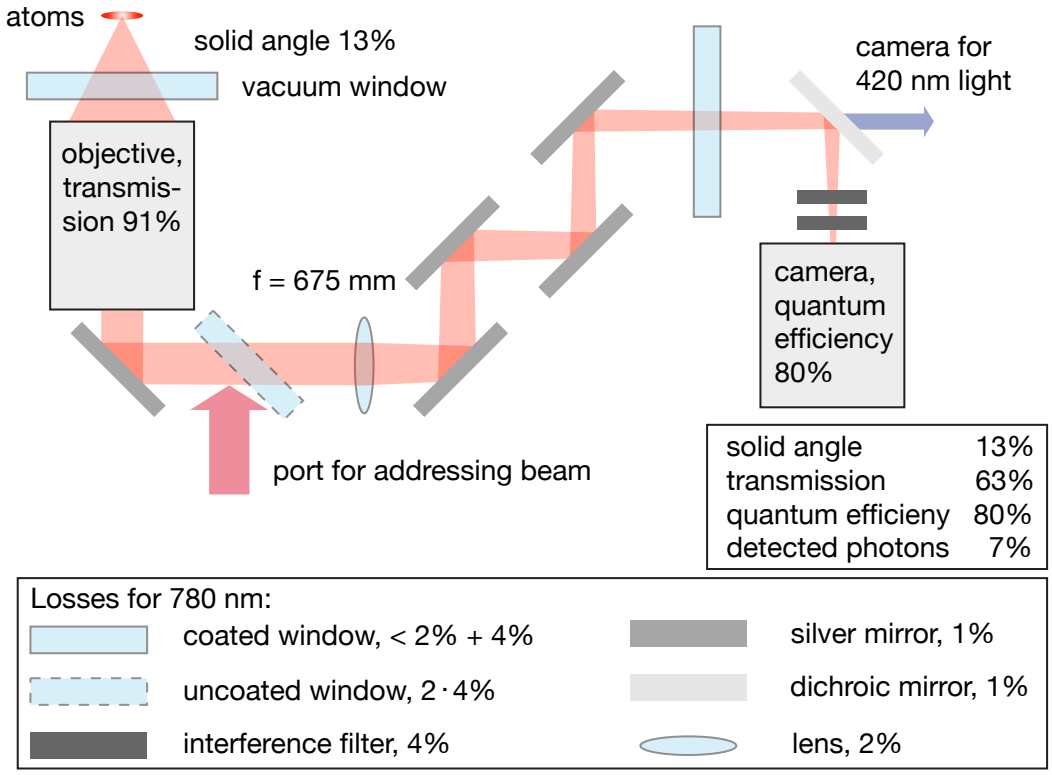

Figure 4.2: Imaging beam path and transmission. The imaging system consists of the objective and an achromatic lens. The glass plate behind the objective allows to insert additional beams. It causes no astigmatism, because the wavefronts are almost plane behind the objective. The vacuum window is only coated on the top side, with a high reflectivity of the lattice wavelength $\lambda_{\mathrm{lat}} = 1064\,\mathrm{nm}$, but a high transmission of the imaging wavelength $\lambda = 780\,\mathrm{nm}$ and also of $\lambda = 420\,\mathrm{nm}$. A copy of this window as well as two interference filters are placed in the beam path to further suppress the vertical lattice beam which is reflected at the vacuum window. The use of in total five silver mirrors is dictated by the geometry of our setup. The legend lists the losses for the imaging wavelength at the different optical components, which sum up to an overall transmission of 63%. For the uncoated window we use the average reflectivity of the s and p polarization. The fraction of detected photons is given by the solid angle of the objective of 13% (NA=0.68), the transmission of 63% and the quantum efficiency of the camera of 80% and amounts to 7%.

Parameter	Value	Unit
σ_1	2.06(5)	pixel
σ_2	9.6(1.2)	pixel
a	0.075(2)	-
C	1050(7)	counts

Table 4.1: Parameters of the fit of the model function Eq. (4.2) to the atomic PSF.

We expect our PSF to be a convolution of an Airy disk with a Gaussian, taking into account the width of the atomic wave packet in the potential wells and the pixel size in the object plane of 125 nm. Due to this convolution, the first minimum of the airy pattern is not visible in our averaged signal.

Tab. 4.1 lists the parameters of a fit of the model function Eq. (4.2) to the atomic PSF [Fig. 4.1(d)]. The width $\sigma_1 = 2.06(5)\text{pixel} = 258(6)\,\text{nm}$ corresponds to a Rayleigh resolution of $r_0 = 740(20)\,\text{nm}$ and is only slightly above the diffraction limited size for ideal point sources.

4.3 Light-assisted collisions

During the imaging, atom pairs on a lattice site are immediately lost due to inelastic light-assisted collisions [35, 46, 47, 106]. The loss is on the time scale of 100 μs for our parameters which is short compared to the total illumination time of 900 ms, such that we do not observe a signal from the atoms before they are expelled. We therefore only detect the particle number modulo two on each lattice site. This essentially amounts to recording the parity of the atom number. Fig. 4.3(a)-(c) illustrates this effect, which has important consequences for the detection of the number statistics (see Sec. 5.3).

We observed that the expelled atoms can be recaptured by the molasses and lead to a large background in the atom distribution, especially along the lattice axes, where lattice is deep enough to hold the atoms [Fig. 4.3(d)]. To avoid this, we apply a 50 ms push out pulse from below, which removes the atoms in the doubly occupied sites, before switching on the molasses. The laser is on the $F = 2$ to $F' = 3$ transition, which is 6.8 GHz red detuned for the atoms in $F = 1$, but excites into the molecular potentials causing light-assisted collisions. Fig. 4.3(e) illustrates that the background is efficiently removed by the push out pulse.

Parity projection constitutes a loss of information and is in many cases not desirable. One way around this is to work at an average filling much smaller than one. One might also let the atoms expand in the third direction after freezing the distribution of the 2D system, in order to make it so dilute that doubly occupied sites become negligible (see Ch. 7). Using blue detuned light, the energy gained by the atoms in the light-assisted collision can be limited, leading to the loss of only one of the two atoms

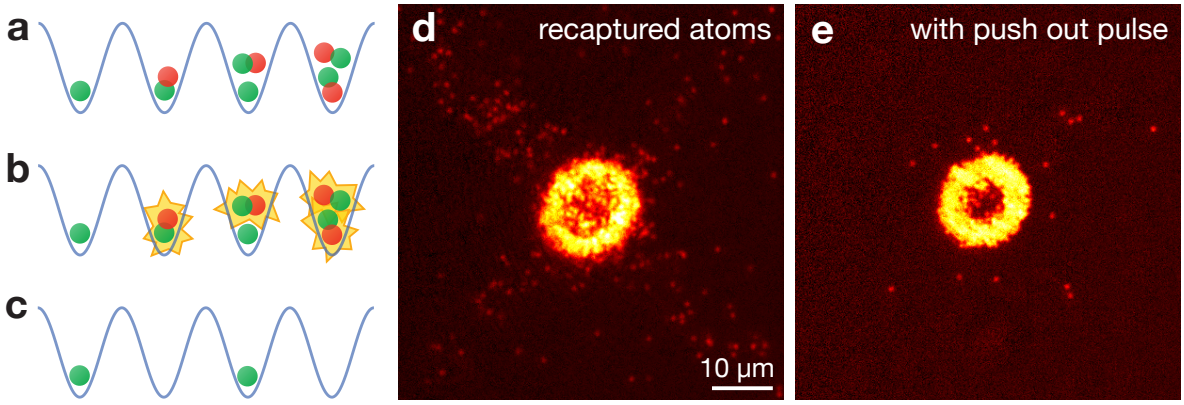

Figure 4.3: Light-assisted collisions and push out. (a) Initial density distribution with different atom numbers per lattice site. (b) Light-assisted collisions due to the optical molasses lead to rapid pair-wise loss of the atoms. (c) The measured density distribution is the initial density distribution modulo two. (d) fluorescence image of an n=2 Mott insulator without push out. The atoms in the doubly occupied sites are expelled from their wells by the light-assisted collisions, but they are recaptured by the molasses. This leads to a strong background of atoms, especially along the lattice axes. (e) fluorescence image of a n=2 Mott insulator with a push out before the imaging, which removes the atoms in doubly occupied sites

in most cases [107]. Combining this idea with grey molasses cooling [108, 109] might be a route to avoid the losses. In *in situ* absorption imaging, the light-assisted collisions can be avoided by switching off the lattice just before imaging, thus decreasing the density [91]. Another possibility is to use an accordion lattice [110], that can be expanded until the sites are resolvable and then add a separate pinning lattice that mutually isolates the atoms [111].

4.4 Image evaluation and deconvolution

This section describes how we evaluate our fluorescence images and reconstruct the atom number distribution using a deconvolution algorithm.

Determination of the lattice angles and spacing

To characterize our imaging system and to determine the lattice structure, we used a fluorescence image of a dilute thermal could [Fig. 4.1(c)]. The lattice axes are oriented at approximately $\pm 45^\circ$ with respect to the image coordinates. A precise determination of these angles and of the lattice spacing is needed so that the deconvolution algorithm works with high fidelity. We first determined the center positions of isolated atoms from this image by a simple fitting algorithm. The histogram of the mutual

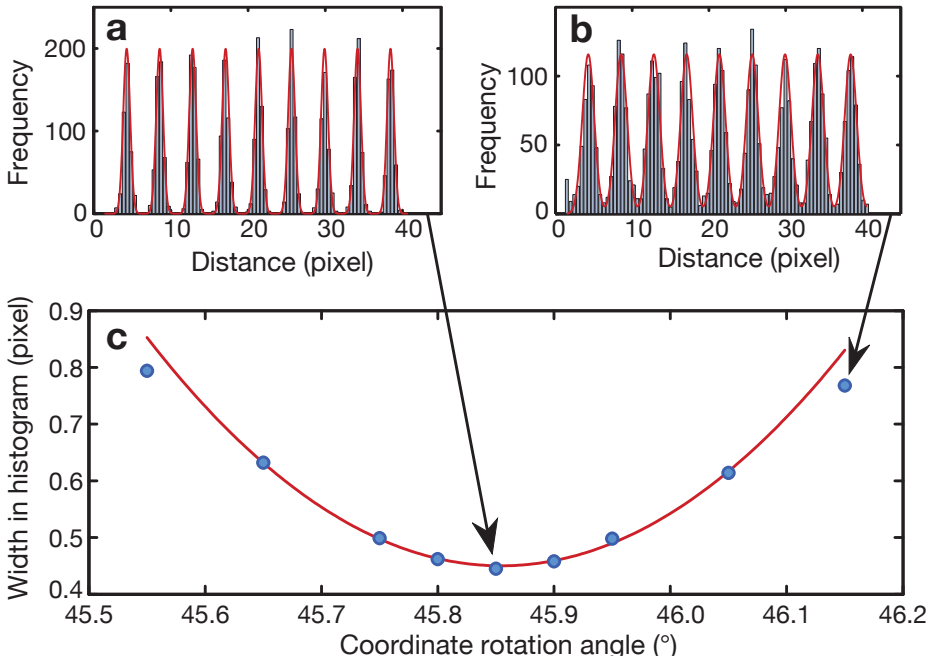

Figure 4.4: Determination of the lattice angles. (a), (b) Histogram of the distances between the center positions of individual atoms for different angles θ of the coordinate system. The red line is a fit to a sum of equidistant Gaussians. The atom positions are taken from Gaussian fits to isolated atoms in a dilute cloud as in Fig. 4.1(c). (c) The width of the fitted Gaussians shows a clear minimum versus θ. The red line is a parabolic fit and yields a minimum at a rotation angle of $\theta = 45.85(5)^\circ$.

distances between these center positions along the axes of a coordinate system rotated by an angle θ clearly shows the periodicity of the lattice [see Fig. 4.4(a),(b)]. The visibility of the pattern depends very sensitively on θ, because the periodicity is only visible if we project the distances along the right direction.

For a quantitative analysis, we fit a sum of equidistant Gaussians to the histogram. The width of the Gaussians for different values of θ [Fig. 4.4(c)] shows a clear minimum at $\theta = 45.85(5)^\circ$. We obtained a similar graph for the other lattice axis and found an angle of $-45.55(5)^\circ$. The distance of the Gaussians is $4.269(4)$ pixel which corresponds to the lattice period of 532 nm. Thus, our magnification factor is 128.4(5) and one pixel of the CCD camera corresponds to 125 nm in the object plane. The angles and the lattice spacing determined by this method are used as fixed parameters for our deconvolution algorithm. We also found that the phases of the two lattice axes slightly drift from shot to shot. They are determined for each image by fitting the center positions of single atoms in the outer part of the images.

Reconstruction of the atom number distribution

We developed a deconvolution algorithm to reconstruct the atom number distribution from a fluorescence image [Fig. 4.5(a)]. The algorithm tries different model-configurations for each lattice site and its nearest neighbors in order to minimize the difference of the original image with the reconstructed one [Fig. 4.5(b)]. This reconstructed image is obtained by convoluting the atom number distribution with the atomic PSF [Fig. 4.1(d)]. The algorithm allows for a variance of the fluorescence level of each atom of $\pm 20\%$ of the mean photon count. These varying fluorescence levels partially arise from the inhomogeneous intensity of the molasses light.

We additionally found an increased fluorescence level of about 5%-10% in the center of very dense $n = 1$ shells of a Mott insulator, compared to the isolated atoms in the outer part of the images. This effect might arise from rescattering, which effectively blocks a significant part of the solid angle, redirecting the photons out of the plane. The cross section for rescattering a photon in a stimulated Rayleigh transition is of the order of the resonant cross section [112] which is of the same size as the distance between the atoms.

We have evaluated the fidelity of the reconstruction algorithm by creating simulated images of a known atom distribution using the PSF of our imaging system, the poissonian and superpoissonian noise contributions of the light hitting the EMCCD camera (including the amplification process), and the site-to-site fluorescence fluctuations of $\pm 20\%$. Running the reconstruction algorithm over several hundred of such randomly generated images of Mott insulators at finite temperatures, we find a reconstruction fidelity of $\sim 99.5\%$. In our experiment, the main limitations of the fidelity are atom losses during the detection process due to collisions with background gas atoms (Sec. 4.5). The imaging time of 900 ms is thus a compromise between the acquired signal and the described atom losses.

A more sophisticated algorithm is presently under development and will be described in the thesis of Peter Schauß.

Etaloning of the camera

We correct for an etaloning effect of the CCD camera, which causes a spatially dependent signal strength (see Fig. 4.6). We determined the effect by summing over 90 images with two slices of a large thermal cloud [Fig. 4.6(a) and (b)]. To eliminate the shape of the cloud, we fitted the data with an 8th order polynomial and divided the data by this fit, obtaining the etalon data containing the fringes [Fig. 4.6(c)]. The outer regions with little signal were set to one. All pictures are divided by this etalon data to correct for the effect.

We correct for stray light by subtracting a second picture without the atoms but with the same molasses parameters.

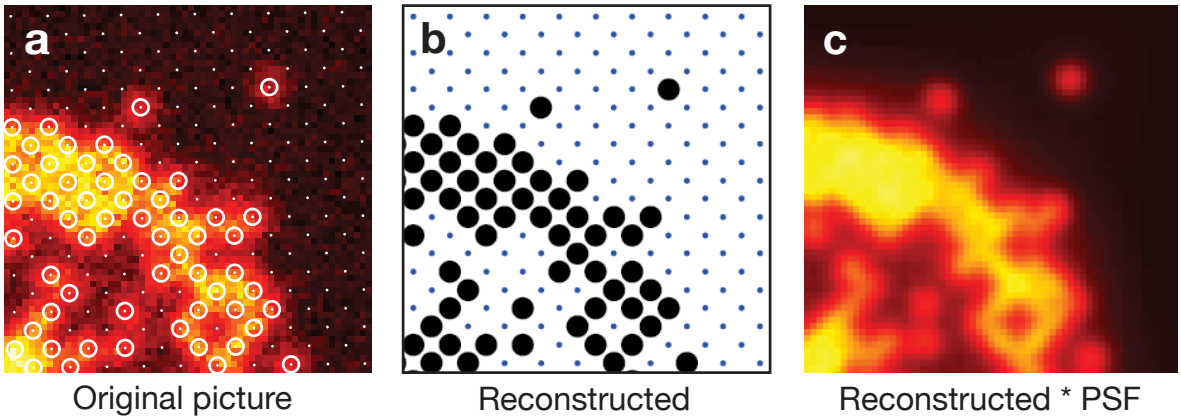

Figure 4.5: Illustration of the deconvolution algorithm. (a) Original picture. The white dots mark the lattice sites as determined from the position of isolated atoms and the lattice angles and spacing. The white circles indicate, where the algorithm found an atom. (b) Reconstructed atom distribution on the lattice. (c) Convolution of the reconstructed image with the PSF of the imaging system. This data is subtracted from the original picture, and the reconstruction is changed to minimize the residuum. The algorithm also allows for spatially varying signal levels.

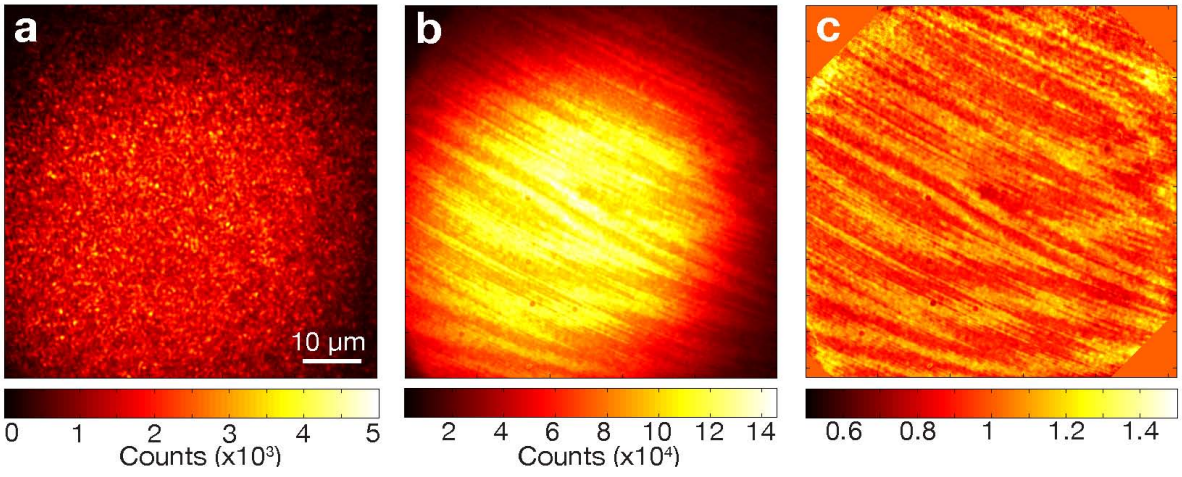

Figure 4.6: Etalonning of the camera chip. (a) Picture of a thermal cloud (two slices). (b) Sum over 90 such pictures. Fringes originating from interference in the camera chip are clearly visible. (c) The picture in (b) divided by a polynomial fit of 8th order. In order to correct for the etalon effect, we divide each picture by this data.

4.5 Optical molasses

For imaging the atoms, we freeze the distribution by ramping the lattices to a depth of $\sim 300\,\mu$K per axis and illuminate them with an optical molasses, which simultaneously laser cools the atoms. If the parameters are chosen well, the atoms stay in their lattice site during the imaging time of about 900 ms. With a total scattering rate of ~ 150 kHz, we detect about 7000 photons per atom which allows to reconstruct the atom distribution with high fidelity (see Sec. 4.4).

We use five molasses beams oriented along the lattice axes in a $\sigma^+ - \sigma^-$ configuration (see Fig. 4.7). Two horizontal beams are overlapped with the corresponding lattice beams via a dichroic mirror and are retro-reflected after a separation from the lattice beams via another dichroic mirror. The beam radii at the position of the atoms are $w_x = 940\,\mu$m and $w_y = 790\,\mu$m. We use a lens before the retro-reflecting mirror, which allows to have a smaller radius of the reflected beam and therefore to compensate for unavoidable power losses. We aligned the radiation pressure from the incoming and retro-reflected beam using a 1D free-space molasses.

A fifth molasses beam is shone in from below, in reverse direction through the imaging system. It has a focus before the objective, such that it is not focused at the focal plane of the imaging system, but has its focus further up and has a radius of $w_z = 4.2(6)\,\mu$m in the focal plane. In order to further expand the beam, we scan it across the cloud with a frequency of 100 Hz (see Fig. 4.7), leading to an effective beam radius of about $w_z^{\text{eff}} = 30\,\mu$m. The significant stray light from this beam, originating from reflections inside the objective, needs to be taken into account as described in Sec. 4.4. The scanning of the position of the z molasses beam helps to wash out fringes in this stray light and interferences between the stray light and the signal. The z molasses beam is not balanced by a counter-propagating beam; the polarization gradients from the interference with the horizontal beams are sufficient for cooling in the z direction.

Thermal hopping

When the atomic distribution is frozen by very deep optical lattices, the quantum mechanical tunneling rates of the low bands become extremely small. However, the fluorescing atoms can undergo thermal hopping, i.e. overcome the barrier between the lattice sites by their thermal energy. This process can be modeled by the Arrhenius law [38], which is often used to describe chemical reaction rates or diffusion of adsorbates [113, 114]. To a good approximation, the activation energy for a hopping event is given by the lattice depth V_0, because the tunneling rate is suppressed for all but the very last bound states. The hopping rate Γ_h can then be written as $\Gamma_\text{h} = \Gamma_a P(E > V_0)$, where Γ_a is the attempt rate, and $P(E > V_0)$ is the probability to find an energy E larger than the trap depth V_0 in the thermal distribution. The laser field acts as a thermal bath for the atoms and the attempt rate Γ_a, with which the atom probes the tail

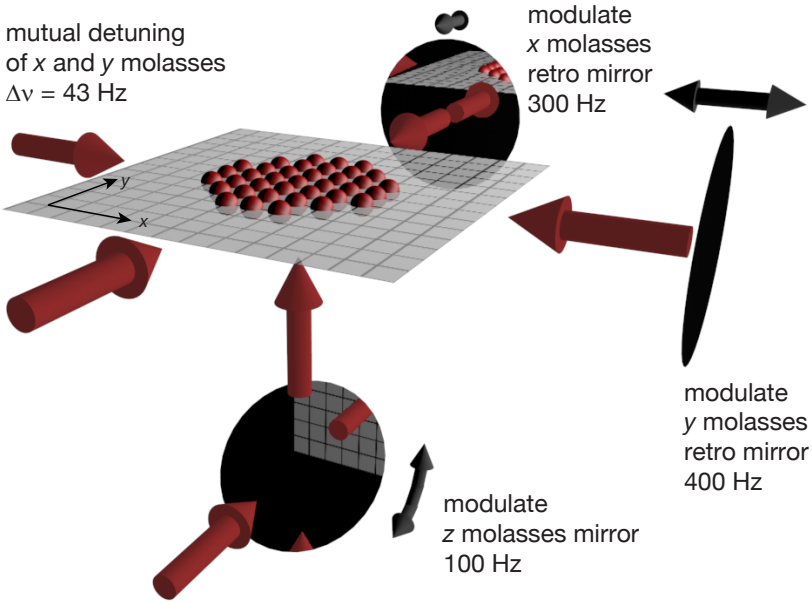

Figure 4.7: Configuration of the molasses beams and the applied modulations.

of its thermal distribution, is related to the laser cooling time. The hopping rate can be evaluated to

$$\Gamma_h \approx \Gamma_a \left(\int_{V_0}^{\infty} \exp(-E/k_B T) \mathrm{dE} \right) / (k_B T) = \Gamma_a \sqrt{\pi} \mathrm{erfc}(\sqrt{V_0/k_B T}), \qquad (4.3)$$

where $\mathrm{erfc}(x) = 2/\pi \int_x^{\infty} \exp(-t^2) \mathrm{d}t$ is the complementary error function.

We measure the site-hopping rate by taking two consecutive images of the same cloud for the first 200 ms and the last 200 ms of our 900 ms illumination period. We compare the reconstructed atom distribution of the two images and extract the number of lost atoms and of hopped atoms [see Fig. 4.8(a),(b)]. Atoms that appear at a previously empty site in the second image count as a hopping event. Subtracting this number from the number of atoms that have disappeared from their sites in the second image yields the atom loss. We cannot assign which atom moved to which site and therefore do not consider the traveled distance, but can only count the number of events. For thermal hopping, we do not expect that the atoms move site by site as for quantum mechanical tunneling. They rather move an arbitrary distance before they are recooled to a different lattice site. Normalizing by the total number of atoms and the time between the two images, we find the hopping rate and the loss rate, and record these for different lattice depths [see Fig. 4.8(c)]. A fit to Eq. (4.3) yields a temperature of $T = 26(4)\,\mu$K and $T = 18(2)\,\mu$K and an attempt rate of $\Gamma_a = 19(9)$ Hz and $\Gamma_a = 21(9)$ Hz for the x and the z lattice, respectively.

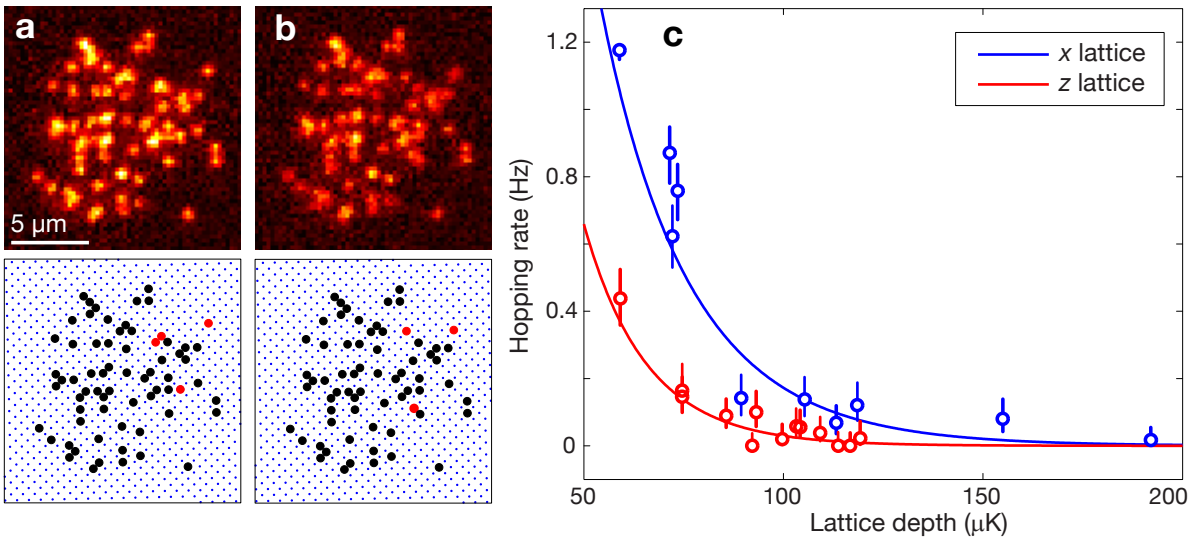

Figure 4.8: Thermal hopping and Arrhenius process. (a), (b) Top row: two consecutive images of the same dilute cloud, containing 69 atoms, taken during the first 200 ms and the last 200 ms of the 900 ms illumination period. Bottom row: reconstructed atom distribution. In the second picture, 4 atoms have disappeared and 3 atoms appeared (marked red in the respective images), suggesting a hopping rate of $\Gamma_\mathrm{h} = 6(8)$ Hz and a loss rate of $\Gamma_\mathrm{l} = 2(5)$ Hz. (c) Hopping rate Γ_h versus the lattice depth of the x and the z lattice. For each curve, the other two lattices are fixed at their maximum depth. The data is fitted to an Arrhenius process as defined in Eq. (4.3) yielding temperatures of $T = 26(4)\,\mu$K and $T = 18(2)\,\mu$K, respectively. The displayed error bars show the 1σ statistical uncertainty, given by the Clopper-Pearson confidence limits.

Optimization of the molasses parameters

For the optimization of the molasses parameters, we monitor the hopping rate, which is a measure for the molasses temperature. Fig. 4.9(a),(b) shows the hopping rate Γ_h and the loss rate Γ_l for different molasses intensities and detunings. The intensity is given as the saturation parameter s_tot of all five molasses beams calculated from a calibration of the optical power and the beam size. The detuning $\Delta = \Delta_\mathrm{free} + \Delta_\mathrm{lat}$ is composed of the free space detuning Δ_free and the additional detuning from the optical lattice $\Delta_\mathrm{lat} = -40$ MHz (as measured by the shift of the resonance of *in situ* absorption imaging). We find a parameter region, in which both the hopping rate and the loss rate are small. They increase for smaller detunings and larger intensities, but also begin to increase for too large detunings. We attribute the loss rate to collisions with background atoms. For very bad molasses parameters, the loss rate also comprises atoms that are thermally activated to completely leave the lattice and the distinction between hopping rate and loss rate is difficult. For optimal molasses parameters, the loss rate has a background value of about 1% over 900 ms, which corresponds to a

trap lifetime of $\sim 75\,\mathrm{s}$, in agreement with independent lifetime measurements in the magnetic trap.

Fig. 4.9(c) shows the hopping rate plotted versus the ratio $s_{\mathrm{tot}}/|\Delta|$ of the saturation parameter and the molasses detuning. We find that in this plot the curves for different detunings coincide. This suggests that the hopping is limited by the $T \propto s_{\mathrm{tot}}/|\Delta|$ relation of polarization gradient cooling [115–117]. We also observe how this relation begins to break down at very small values of $s_{\mathrm{tot}}/|\Delta|$. The solid line shows a fit to an Arrhenius process [Eq. (4.3)], which assumes a linear dependence as $k_B T/V_0 = C \cdot s_{\mathrm{tot}}/|\Delta|$, yielding a prefactor $C = 0.33(5)$ and an attempt rate of $\Gamma_{\mathrm{a}} = 24(1)\,\mathrm{Hz}$.

We choose a free space detuning of $\Delta_{\mathrm{free}} = -40\,\mathrm{MHz}$ and a saturation parameter of $s_{\mathrm{tot}} \sim 7$ as optimal parameters, which yield a scattering rate of $\Gamma_{\mathrm{sc}} \sim 150\,\mathrm{kHz}$ and a hopping rate of $\Gamma_{\mathrm{h}} \sim 0.01\,\mathrm{Hz}$. Within the usual imaging time of 900 ms, we collect about 7000 photons per atoms for these parameters.

For these measurements, we used dilute clouds of 30-70 atoms, which allowed to reconstruct the distribution with high fidelity even for molasses parameters that yield a small signal. We checked, however, that at the optimal parameters the hopping rate is the same for dense clouds with unit occupation. In fact, we do not expect to see the density dependent heating via rescattering, because in our 2D system the scattered photons can escape in the direction perpendicular to the lattice. The neighboring atoms block only a few percent of the solid angle (the scattering cross section for stimulated Rayleigh scattering of the emitted photons is on the order of the resonant cross section [112]). If rescattering was a problem, we would expect the temperature to depend on the scattering rate, because heating can be suppressed by scattering slower than the trap frequency [112]. In Fig. 4.9(d) we plot the hopping rate versus the total scattering rate. Low hopping rates are only achieved for scattering rates around $\Gamma_{\mathrm{sc}} \approx 150\,\mathrm{kHz}$, only slightly smaller than our trap frequencies of $\sim 200\,\mathrm{kHz}$. Therefore, the plot suggests that the scattering rate does not set the temperature limitation.

We checked the calibration of our molasses power which we use to calculate the saturation parameter s_{tot} by comparing the resulting scattering rate

$$\Gamma_{\mathrm{sc}} = \frac{\Gamma}{2} \frac{s_{\mathrm{tot}}}{1 + s_{\mathrm{tot}} + (2\Delta/\Gamma)^2} \tag{4.4}$$

to the number of detected photons per atom. From the peak counts per atom $C_{\mathrm{peak}} \approx 1000$, we calculated the total counts per atom as $C_{\mathrm{tot}} = C_{\mathrm{peak}} \frac{\pi}{2} (\frac{2\sigma}{B})^2$, where $\sigma = 2.1$ pixel is the $1/\sqrt{e}$ radius of the PSF and B is the pixel binning of the camera ($B = 2$ in this section). The number of photons needed to obtain the above A/D counts is given by the camera sensitivity $S_{\mathrm{cam}} = 300/58.4$, including the EM-CCD gain of 300 (camera settings are shift speed=3.3, PreAmp=1, read out rate=0.1 MHz). Dividing the number of detected photons by the illumination time T and the fraction F of detected photons (Sec. 4.2), we obtained the total scattering rate $\tilde{\Gamma}_{\mathrm{sc}} = C_{\mathrm{tot}}/S_{\mathrm{cam}}/T/F$

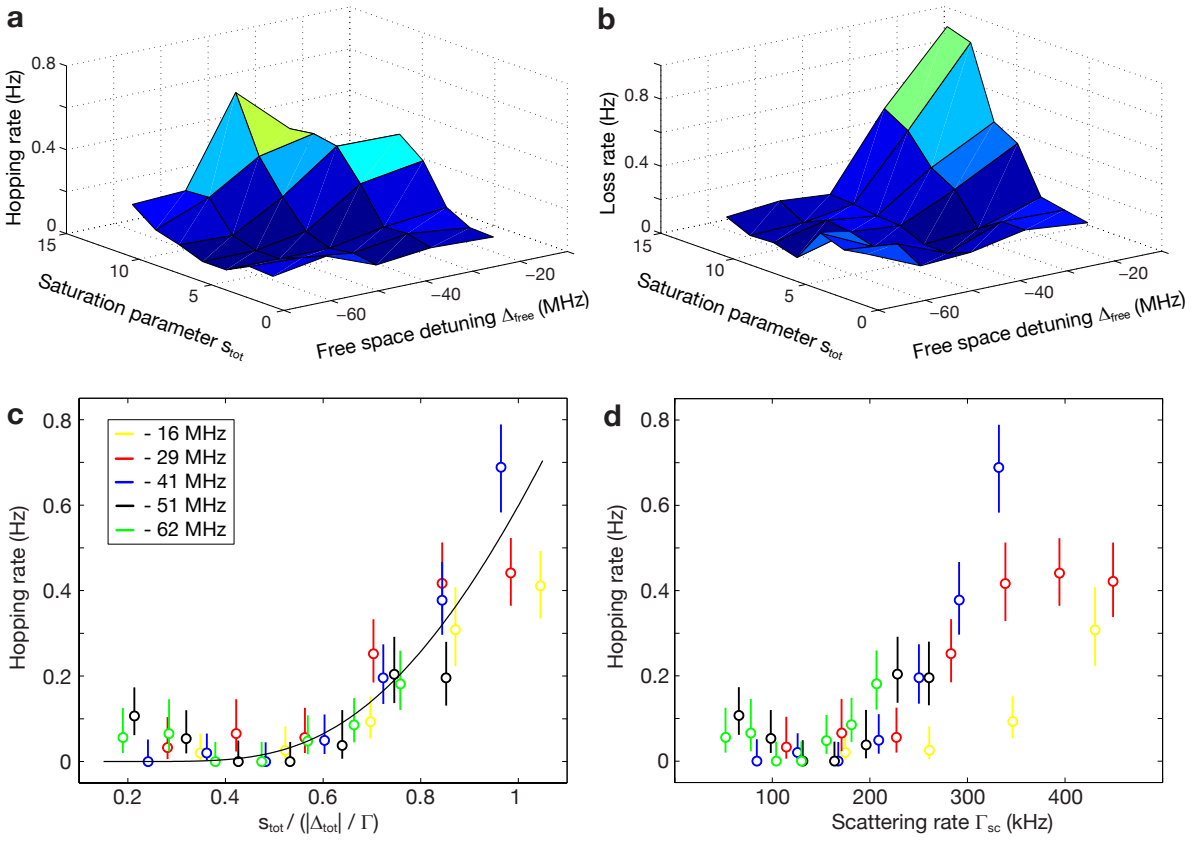

Figure 4.9: Optimization of the molasses parameters. (a) Hopping rate and (b) loss rate as a function of the saturation parameter s_{tot} and the free space detuning Δ_{free} of the molasses. (c) Hopping rate as a function of $s_{\mathrm{tot}}/|\Delta|$. The curves for different detunings coincide, suggesting the typical temperature dependence of polarization gradient cooling. The legend states the free space detuning $\Delta_{\mathrm{free}}/(2\pi)$. (d) The same data plotted versus the total scattering rate Γ_{sc}.

and found reasonable agreement with the calculation from the saturation parameter and detuning.

For the measurements of this section, the beam balance was carefully aligned (also using the intensity of the peaks in the far-field diffraction patterns of Ch. 8). However, this is not mandatory. At the optimal molasses parameters, the hopping can be very small, even when the retro-reflections of both horizontal molasses beams are blocked. The relevant condition is that there are polarization gradients in all directions. The light pressure imbalance can be absorbed by the tight confinement in the lattice sites.

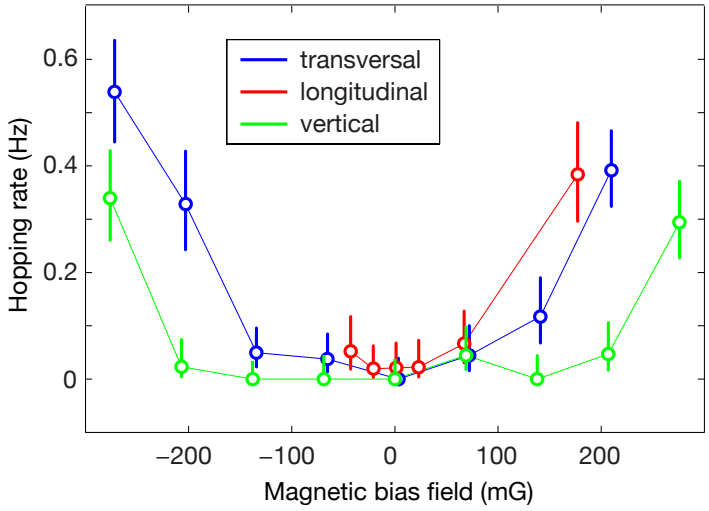

Figure 4.10: Hopping rate as a function of applied bias fields in different directions.

Sensitivity to magnetic bias fields

It is well known that an optical molasses is sensitive to a magnetic bias field. A transverse field leads to a Larmor precession, which changes the population of the magnetic sublevels, thus competing with the optical pumping process that leads to the cooling in a polarization gradient. Also the Zeeman-shifts must be smaller than the AC-stark shifts between different m_F states. It was found that the molasses temperature increases considerably, when the Larmor frequency is not a factor of ten below the scattering rate [118].

In Fig. 4.10 we applied a magnetic bias fields in different directions and monitored the resulting hopping rate for the optimal molasses parameters. We found that a bias field of up to a few 10 mG is tolerable if all other molasses parameters are optimized.

One should be aware that the optical lattices can create an effective magnetic field via a differential light shift if their polarization has a circular component. At the very large powers required for the imaging this can be relevant even for a wavelength of $\lambda_{\mathrm{lat}} = 1064\,\mathrm{nm}$. We measured the effective magnetic field using microwave spectroscopy in the deep lattices and found values as large as 100 mG, which we could reduce to 3 mG by placing additional polarizing cubes close to the atoms.

Washing out of interferences between the molasses beams

In a one-dimensional molasses, both the σ^+-σ^- as well as the lin-$\perp$-lin configuration show a periodic modulation only in the local polarization, but not in the intensity. This is, because the two counter-propagating beams have orthogonal polarizations

and can therefore not interfere. With additional beams as in a three-dimensional molasses, however, there will be an intensity pattern, which causes inhomogeneous illumination of the atoms. Therefore it is common to modulate certain parameters of the molasses in order to wash out these interferences [45, 47]. The modulation has to be slow compared to the scattering rate ($\simeq$ 150 kHz) in order to not compromise the polarization gradient cooling mechanism, but fast compared to the imaging time (900 ms). The modulations that we apply are indicated in Fig. 4.7: the retro-reflecting mirrors of the x and y molasses beams are modulated with a frequency of 300 and 400 Hz, respectively, and the z molasses is scanned across the cloud with a frequency of 100 Hz. Additionally, the y molasses is detuned with respect to the x and z molasses by 43 Hz.

The scanning of the z molasses is mainly for washing out interferences with the stray light that originates from this beam. It seems that its scanning has little influence on the wavefront at the position of the atoms and it is therefore kept on in the following. When omitting other molasses modulations, the interferences of the molasses beams can be clearly seen in the image of a Mott insulator [see first row of Fig. 4.11(a)-(c)]. In Fig. 4.11(a), the modulation of the retro-reflecting mirror of the x molasses was omitted and interference fringes perpendicular to the non-modulated molasses are clearly visible. The second and third row show integrated profiles along the axis as indicated by the dashed white lines in the first row. The period of the fringes is 7% larger than the molasses wavelength of 780 nm, which is probably due to a small angle between the two counter-propagating molasses beams. In Fig. 4.11(b), the modulation of both retro-reflecting mirrors was omitted and in In Fig. 4.11(c), also the relative detuning of the molasses beams was omitted, such that all five beams interfere.

The spread of the atomic wave function is large enough to map out the intensity pattern. A Moiré pattern between the molasses' interference and the lattice spacing is only seen in the reconstructed images [Fig. 4.11(d)]. When the minimum of the molasses intensity coincides with a lattice cite, the atom is likely to get lost and we see indeed a reduced atom number with a period of about 3 lattice sites.

We investigated how fast we can wash out of the interference pattern without compromising the molasses by changing the detuning of the y molasses with respect to the other two molasses. We found that the hopping rate is not changed for a detuning of up to 10 kHz, while it then grows rapidly. At a total scattering rate of 150 kHz, or a single beam scattering rate of about 30 kHz, this shows that the cooling is already efficient, if just a few photons are scattered in a given polarization gradient configuration. We also detuned the z molasses instead of the y molasses and found the same behavior, but the interference between the x and y molasses was still visible as a horizontal modulation.

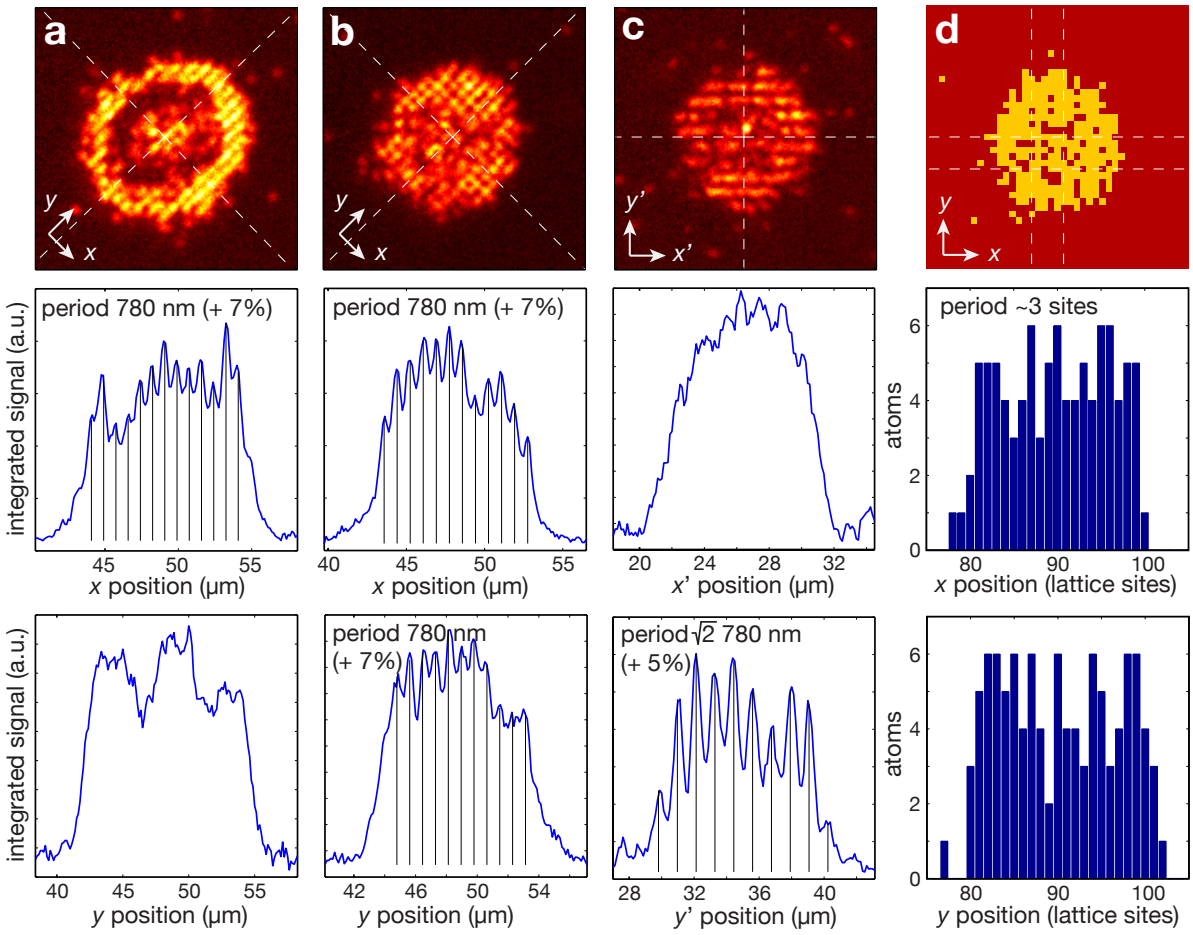

Figure 4.11: Interference pattern of the molasses beams, illustrating the need to wash them out by modulating the molasses. (a) Omitting the modulation of the x molasses, one clearly sees the interference with the retroreflected beam. (b) Omitting the modulation of the x and the y molasses, one sees the interference along both directions. (c) Omitting the detuning between the x and the y molasses, one sees the stripes arising from their interference with a period which is larger by a factor of $\sqrt{2}$. (d) Reconstruction of (b). Atoms are more likely to be missing with a period of three sites, where the minimum of the interference pattern coincides with a lattice site. The top row shows the fluorescence images. The middle and bottom row show density profiles integrated along the respective coordinates [in the restricted range indicated by the dashed lines in the case of (d)].

4.6 Possible spin-dependent imaging and single-qubit read-out

In the present scheme, spin dependent imaging relies on removing one spin component before detection (see Ch. 6). For experiments with spin mixtures [29, 119] it would be desirable to image both spin states in the same experimental run. This can however not be done using a molasses, because it mixes all magnetic sub-states. One possibility is to apply absorption imaging on one of the components, while shelving the other spin component. If the scattering is done on a closed transition $F = 2$ to $F' = 3$ with circular polarized light, one can heat the atom out of the trap before it is depumped to the $F = 1$ manifold. Subsequently one can use the molasses to image the shelved atoms.

For a future one-way quantum computation scheme [51, 52], it is mandatory to read out qubits during the computation process without affecting the other atoms. This could be done by using two states in the $F = 1$ manifold as qubit and transfer the selected atom to $|F = 2, m_F = -2\rangle$ for detection. There it can resonantly scatter a few hundred photons on the closed transition $F = 2$ to $F' = 3$ from a single σ^- polarized beam, such that the atom is heated out of the trap before it is depumped to the $F = 1$ manifold. One would first transfer from one of the qubit states in the $F = 1$ manifold and detect its population and then transfer the other state and also detect it. As all other atoms remain in the $F = 1$ manifold, they remain unaffected by the light on the $F = 2$ to $F' = 3$ transition. The selective transfer to $F = 2$ can be done by the combination of a differential light shift from an addressing beam and appropriate microwave and radio frequency pulses (see Ch. 6). As there is only one atom imaged at a time, the few hundred scattered photons might be sufficient to detect it, e.g. by imaging the full signal on a single avalanche photo diode. One open question is if one can ensure that the atom is heated out of the trap without hopping to different lattice sites and disturbing the atoms there.

4.7 Conclusion

In this chapter we have shown how we image quantum gases in an optical lattice with single-site resolution and single-atom sensitivity. We use an imaging system with a numerical aperture of NA $= 0.68$ located outside the vacuum chamber, yielding a diffraction limit of 700 nm, slightly above the lattice spacing of 532 nm. It was tested in a separate setup and characterized via a test target. We measure the point spread function of single atoms and compare it to that of the test setup.

Light-assisted collisions in the molasses lead to a rapid pair-wise loss of atoms, such that we only detect the parity of the atom number per lattice site. As we only have to discriminate between one or zero atom per site, we can reconstruct the atom distribution on the lattice despite the resolution above the lattice spacing. For this, we precisely determined the lattice angles and the lattice spacing from images of a dilute

cloud. A deconvolution algorithm digitizes the images with a fidelity of $\sim 99.5\%$.

During the fluorescence imaging, we apply an optical molasses, which simultaneously laser cools the atoms to a temperature $\sim 20\mu$K in a lattice with 300 μK depth per axis. We collect about 7000 photons per atoms in 900 ms yielding a large signal over a small background. By optimizing the molasses parameters, we can make thermal hopping and losses negligible.

5 Imaging Mott insulator shells

In this chapter we apply the single-atom resolved imaging technique presented in the previous chapter to Mott insulators in the atomic limit. We directly observe both the characteristic shell structure and the number squeezing in the Mott shells. A comparison of the radial density distribution with theory provides a precise *in situ* temperature and entropy measurement from single images.

5.1 State of the art

The superfluid-to-Mott-insulator transition has been studied extensively since its first realization [2]. When the interactions are increased relative to the kinetic energy, the atoms are localized to their sites, which leads to a number squeezing and the loss of phase coherence between the different sites. In an external confinement, the density distribution changes from the smooth Thomas-Fermi profile of a weakly-interacting BEC to a characteristic shell structure, in which the number distribution is pinned to integer values. Also the excitation spectrum changes.

In a BEC, arbitrarily small excitations exist, which correspond to phase offset between sites, while in a Mott insulator an energy gap opens, and the smallest possible excitation is one particle in excess which has an energy cost of one interaction energy U. All these properties have been verified experimentally and were used to detected the Mott insulated state.

The first observation of the Mott insulator was via the the loss of phase coherence, which is a direct consequence of the localization of the atoms [2, 120]. The measurement is done by switching off the trap and observing the matter wave interference after time-of-flight, which shows prominent peaks at a momentum of the reciprocal lattice vector. The phase coherence is deduced from the visibility of the interference pattern and the reappearance of this visibility when going back to a shallow lattice shows that one can reversibly cross the phase transition.

Another feature of the Mott insulator, which was already probed in the first experiments, is the energy gap in the excitation spectrum. It corresponds to a particle-hole pair as lowest lying excitation, which for $U/J \gg 1$ has an energy of U. Excitation spectra have been recorded by driving the system either by applying a magnetic gradient [2] or by amplitude modulation of the lattice [11, 121]. The heating is measured by ramping back to the superfluid state and by detecting the increased dephasing in the broadening of the central momentum peak after time-of-flight. In the Mott insulator, the spectra show distinct peaks at energies of U and also $2U$, where the

latter comes from excitations at the boundaries between two shells. It has been subsequently argued that the appearance of the peaks in the excitation spectra alone is not a prove of a Mott insulating state and that an analysis of the strength of the peaks at different multiples of U would be required.

A method, which tackles the shell structure, is to record the global atom number statistics, i.e. the occupation numbers averaged over the entire system for different total atom numbers, and to compare it to theory. For a superfluid one expects to find all occupations numbers for any filling. For the Mott insulator, however, one expects an enhancement of certain occupation numbers, depending on what shells exist at the given total atom number. E.g. the fraction of sites with double occupancy is zero for a perfect Mott insulator with only an $n = 1$ shell. For larger total atom numbers, which lead to the formation of an $n = 2$ shell, this fraction increases steadily, until it decreases again with the formation of the $n = 3$ shell. Different methods have been used to assess the global atom number statistics, ranging from spin changing collisions [122] to interaction blockade [123] and multi-body interactions [65].

While these methods only probe the global atom number statistics, other experiments achieved to image the shell structure. They used a state transfer selective to the filling factor and recording the spatial distribution of lattice sites with different occupations. The filling-selective state transfer was realized by clock shifts [124] (with better data quality in [125]) and by spin-changing collisions [68]. The latter involves tomographic imaging of single 2D slices of a 3D Mott insulator to avoid the integration in one direction.

The shell structure is also revealed in a direct measurement of the density profile obtained from absorption imaging of a 2D Mott insulator with a resolution of $3-4\,\mu$m [91], showing a clear plateau at a density corresponding to unity filling as well as reduced density fluctuations. Finally, Mott insulator shells were imaged with single-site resolution and single-atom sensitivity in the group of Markus Greiner [46] and in our group [47]. Single-site resolved *in situ* images are of special interest, because they can directly probe the squeezing of the number statistics, which is the complementary quantity to the measurement of the phase coherence in the first experiments.

Next to the Bosonic case, the Mott insulator has also been realized for Fermions [10, 11]. In this case, the incompressibility of the insulating state, which can be deduced from the response to an increased external confinement, is a better measure than in the Bosonic case, because the Pauli principle forbids the formation of shells with larger fillings.

5.2 Shell structure of Mott insulators

Our experiments start with a BEC in a single antinode of the vertical z lattice with a depth of $V_z = 26(2)\,E_r$ (The preparation of the BEC is described in Ch. 3). For the Mott insulators, the lattice depths along the x and y directions were then increased

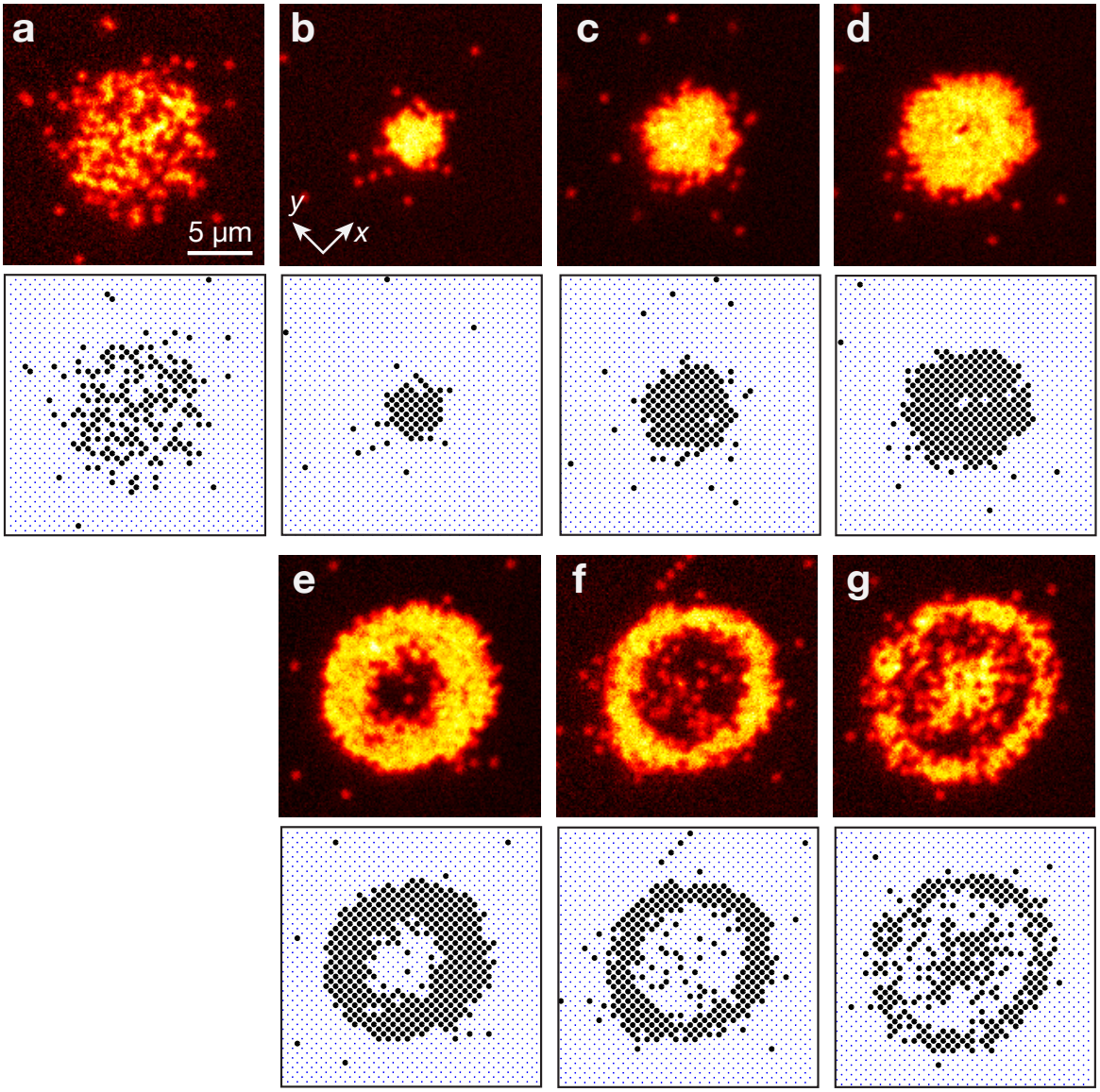

Figure 5.1: High resolution fluorescence images of a BEC and Mott insulators. Top row: Experimentally obtained images of a BEC (a) and Mott insulators for increasing particle numbers (b)-(g) in the zero-tunneling limit. Bottom row: Reconstructed atom number distribution. Each circle indicates a single atom, the points mark the lattice sites. BEC and Mott insulators were prepared with the same in-plane harmonic confinement.

in s-shaped ramps within 75 ms up to $V_{x,y} = 23(2)\,E_r$. A band structure calculation (see e.g. [60]) yields an interaction energy $U = h \cdot 960\,\mathrm{Hz}$ and a tunnel coupling $J = h \cdot 3\,\mathrm{Hz}$ for this lattice depth, such that $U/J \sim 300$ and we are deeply in the atomic limit of the Mott insulator. The Gaussian beam profile of our lattice beams ($1/e^2$ waist radius of 75 μm) caused an additional harmonic confinement with trapping frequencies $\omega_x/(2\pi) = 72(4)\,\mathrm{Hz}$ and $\omega_y/(2\pi) = 83(4)\,\mathrm{Hz}$ at the lattice depths of $V_{x,y} = 23(2)\,E_r$ and $V_z = 26(2)\,E_r$. For comparison, we also imaged BECs without the horizontal lattices, but with similar external confinement dominated by the vertical lattice. To freeze out the atom distribution without crossing the phase transition, we rapidly ramped up the horizontal lattices within 0.1 ms.

Fig. 5.1 shows the resulting atom distributions of a BEC and Mott insulators in the zero-tunneling limit for different atom numbers. We directly observe dramatic differences in the density profiles and the on-site number fluctuations. For a BEC we find that the recorded atomic density exhibits large atom number fluctuations from site to site. In contrast, for a Mott insulator we obtain plateaus of constant integer density, with almost vanishing fluctuations. The images in Fig. 5.1 show how for increasing particle numbers successive Mott insulator shells are formed, which appear as alternating rings of one and zero atoms per site due to our parity measurement (see Sec. 4.3).

In both the raw images and the reconstructed ones, individual defects are directly visible as holes or additional atoms. Because the higher atom numbers are obtained by less evaporation, the larger Mott insulators are hotter than the small ones, which shows in the less sharp transition between the shells. We find that our atom clouds are very symmetric in comparison to those in Ref. [46], which sets an upper bound on the disorder in the optical potentials. A small ellipticity of the clouds is caused by the different harmonic trapping frequencies ω_x and ω_y.

5.3 Number statistics after parity projection

The on-site number fluctuations are an important indicator for the physical state. For a BEC, they are Poissonian, while for a Mott insulator, the number statistics is squeezed, with unity probability for a certain integer filling depending on the shell.

The statistics can be probed via averaging the occupation of each site over many shots [46] or via averaging over different sites in a single image [47]. The latter has the advantage that it is insensitive to shot-to-shot fluctuations of the total atom number or even cloud position, but it is only good, if the potentials are well characterized. Here we take azimuthal averages and observe the number statistics in the mean value and the variance of this average.

The light-assisted collisions in the molasses lead to pair-wise loss of the atoms, such that one only detects the parity of the original atom number per site (see Sec. 4.3). This projection has some consequences on the detected statistics. Let us first consider some

general properties that hold independent of the original atom number distribution. Because one can only find zero or one atom on a site, squaring the single-shot occupation number $n_{\mathrm{det}}(r)$ at a site at radius r has no effect and hence $n^2_{\mathrm{det}}(r) = n_{\mathrm{det}}(r)$ and also $\overline{n^2_{\mathrm{det}}}(r) = \bar{n}_{\mathrm{det}}(r)$. The detected variance is therefore

$$\sigma^2_{\mathrm{det}}(r) \equiv \overline{n^2_{\mathrm{det}}}(r) - \bar{n}^2_{\mathrm{det}}(r) = \bar{n}_{\mathrm{det}}(r) - \bar{n}^2_{\mathrm{det}}(r) = \bar{n}_{\mathrm{det}}(r)\left[1 - \bar{n}_{\mathrm{det}}(r)\right], \tag{5.1}$$

which is simply a function of the mean density. I.e. independent of the on-site atom number distribution, the variance contains not more information than the detected mean density and in turn, the mean density must contain information about the variance, i.e. the atom number distribution. One can say that the parity projection mixes the mean density and the variance of the original distribution. In the same way that $0 < \bar{n}_{\mathrm{det}}(r) < 1$, it holds $0 < \sigma^2_{\mathrm{det}}(r) < 0.25$ and the maximal variance $\sigma^2_{\mathrm{det}}(r) = 0.25$ is found together with the density $\bar{n}_{\mathrm{det}}(r) = 0.5$.

Let us now consider what the parity projection will do to the atom number distribution of a BEC and a Mott insulator. A Mott insulator shell with perfect number squeezing is projected onto a mean value of one or zero depending on the filling of the shell and the variance vanishes. A BEC has a Poissonian on-site number distribution with an original mean value $\bar{n}$. The probability $P_{\mathrm{Poisson}}(n, \bar{n})$ to find n atoms is given by

$$P_{\mathrm{Poisson}}(n, \bar{n}) = \bar{n}^n e^{-\bar{n}}/n!, \tag{5.2}$$

where the mean value is reproduced as

$$\bar{n} = \sum_{n=0}^{\infty} n \cdot P_{\mathrm{Poisson}}(n, \bar{n}). \tag{5.3}$$

When the detected atom number is parity projected we have instead a detected mean value of

$$\bar{n}_{\mathrm{det}} = \sum_{n=0}^{\infty} \mathrm{mod}_2(n) \cdot P_{\mathrm{Poisson}}(n, \bar{n}) = 0.5\left[1 - \exp\left(-2\bar{n}\right)\right]. \tag{5.4}$$

We find that the detected mean density $\bar{n}_{\mathrm{det}} < 0.5$ and that it approaches this value for large original mean values $\bar{n}$, when the probability to find an even or an odd number are equal. This value of $\bar{n}_{\mathrm{det}} \sim 0.5$ is already found for $\bar{n} \gtrsim 1.5$ and, indeed, we detect a mean density of $\bar{n}_{\mathrm{det}} = 0.5$ in the center of our BECs. This reasoning shows that a detected mean density $\bar{n}_{\mathrm{det}} > 0.5$ already is a proof of number squeezing.

5.4 Radial density profiles

The symmetry of our clouds allowed us to average the data azimuthally, taking into account the ellipticity, and to obtain radial profiles for the average detected density $\bar{n}_{\mathrm{det}}(r)$ and its variance $\sigma^2_{\mathrm{det}}(r)$ [see Fig. 5.2(d),(e)]. For this, we first determined the

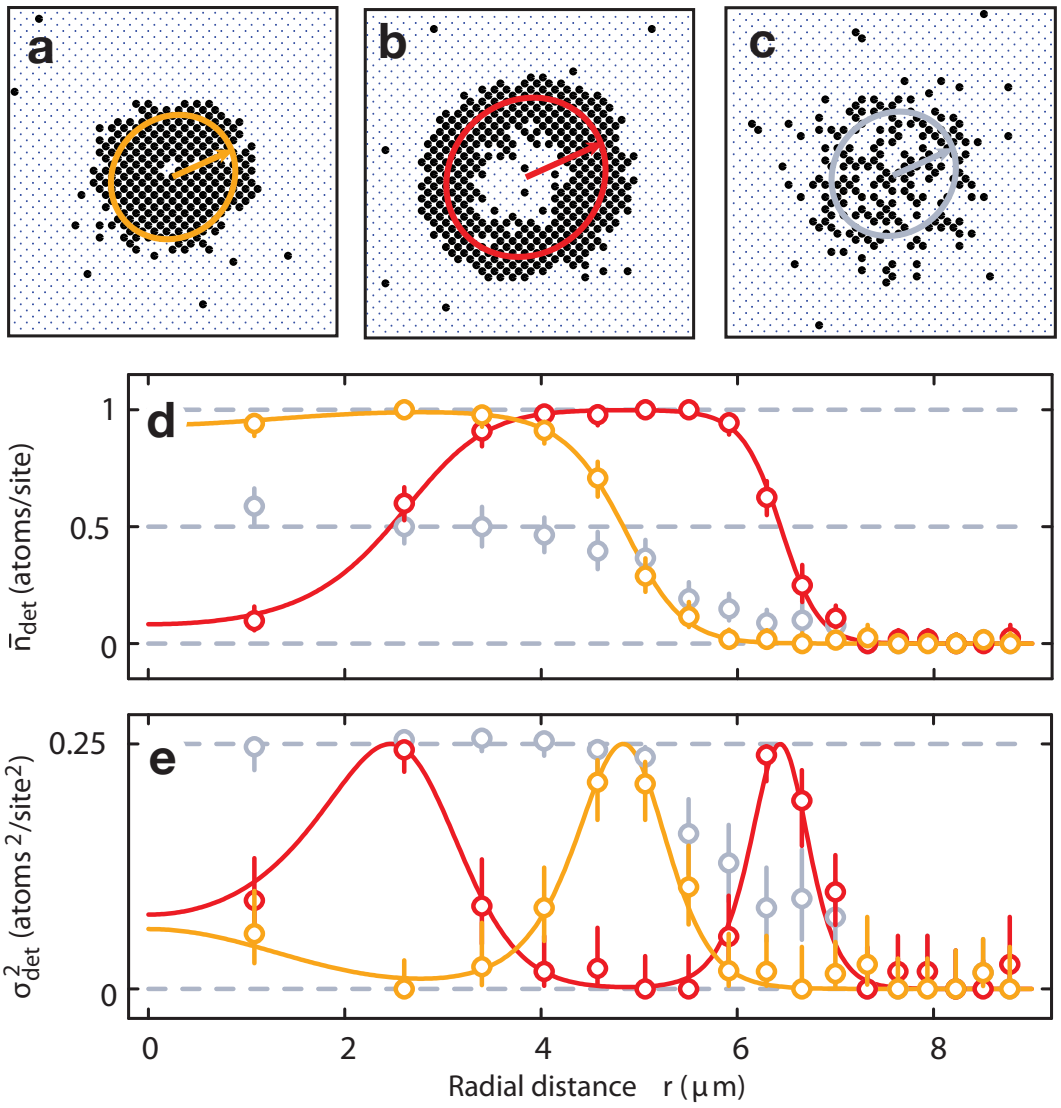

Figure 5.2: Radial profiles of the mean atom density and its variance. (a)-(c) Reconstruction of the $n = 1$ and $n = 2$ Mott insulator images of Fig. 5.1(d),(e) and of the BEC in Fig. 5.1(a) for reference. The circles indicate the (elliptical) azimuthal average at a given radius. (d),(e) Radial profiles of the mean density $\bar{n}_{\mathrm{det}}(r)$ and the variance $\sigma^2_{\mathrm{det}}(r)$ of the data in (a)-(c). The displayed statistical errors are Clopper-Pearson 68% confidence intervals for the binomially distributed number of excitations. For the Mott insulators the density and variance profiles were fitted simultaneously with the model functions of Eqs. (5.7) and (5.1).

center of the cloud as the center of mass of the reconstructed distribution. Then we binned the lattice sites according to their distance from the center, thereby correcting for the ellipticity of 10%. The bin sizes were chosen larger near the center to produce sufficient statistics.

We analyze the radial profiles with a simple model for the atomic limit, i.e. vanishing tunnel coupling. This is a good approximation for our experiments with $U/J \simeq 300$. Coherent particle-hole fluctuations are suppressed as $(J/U)^2$ and they are negligible here. So the deviations from the integer filling are all induced by thermal fluctuations, which are described by a simple thermodynamic calculation. The atom number distribution at a lattice site at radius r is given by

$$P_r(n) = e^{\beta[\mu_{\mathrm{loc}}(r)n - E_n]}/Z(r), \tag{5.5}$$

where $Z(r) = \sum_n e^{\beta[\mu_{\mathrm{loc}}(r)n - E_n]}$ is the grand canonical partition function, $\beta = 1/(k_B T)$, $\mu_{\mathrm{loc}}(r)$ is the local chemical potential and $E_n = Un(n-1)/2$ is the interaction energy. Using a local density approximation (LDA), we define μ_{loc} in terms of the global chemical potential μ and the external harmonic trapping confinement as

$$\mu_{\mathrm{loc}}(r) = \mu - \frac{1}{2}m(\omega_x^2 x^2 + \omega_y^2 y^2). \tag{5.6}$$

Taking the light-induced losses into account, we calculate the expected detected density at different radii as

$$\bar{n}_{\mathrm{det}}(r) = \frac{1}{Z(r)} \sum_n \mathrm{mod}_2(n) e^{\beta[\mu_{\mathrm{loc}}(r)n - E_n]} \tag{5.7}$$

For the Mott insulators in Fig. 5.2, the density and variance profiles were fitted simultaneously with the model functions of Eqs. (5.7) and (5.1) with T/U, μ/U and a radius $r_0 = \sqrt{2U/(m\omega_x\omega_y)}$ quantifying the strength of the external confinement as free parameters [red and orange data and lines in Fig. 5.2(d),(e)]. r_0 was not fixed, because it is not clear at which lattice depth and which according external confinement the distribution is frozen during the ramp into the atomic limit. The fits yielded temperatures $T = 0.090(5)\,U/k_B$ and $T = 0.074(5)\,U/k_B$, chemical potentials $\mu = 0.73(3)\,U$ and $\mu = 1.17(1)\,U$, and radii $r_0 = 5.7(1)\,\mu$m and $r_0 = 5.95(4)\,\mu$m for the $n = 1$ Mott insulator (orange) and the $n = 2$ Mott insulator (red), respectively. From the fitted values of T, μ and r_0, we determined the original atom numbers of the system before parity projection to $N = 270(20)$ and $N = 529(8)$.

For both the density profiles and the atom number variances we find excellent agreement between the experimental data and the theoretical model for all radial distances. This supports the assumption that our system is in global thermal equilibrium, in contrast e.g. to Ref. [126]. The extracted temperatures of $T = 0.090(5)\,U/k_B$

and $T = 0.074(5)\,U/k_B$ for the $n = 1$ and $n = 2$ data are well below U/k_B and accordingly the shell structure is only slightly washed out by thermal excitations. Our temperature estimates are conservative since all defects are attributed to thermal excitations in our model. However, defects might also arise due to "collateral damage" caused by atoms undergoing light-assisted collisions.

For reference, we show the corresponding data obtained by freezing out the atom distribution of a BEC [Fig. 5.2(c) and grey data in Fig. 5.2(d),(e)]. We observe the expected density of $\bar{n}_{\mathrm{det}} = 0.5$ in the center of the cloud together with a maximum variance of $\sigma^2_{\mathrm{det}} = 0.25$. We note that the thermal shells surrounding a Mott insulator core also exhibit this maximum variance and can be as narrow as 1-2 lattice sites. As both the superfluid and the thermal state are expected to show a mean density of 0.5 after parity projection, it is not possible to discriminate between them in these pictures. Furthermore a fit to a BEC with finite condensate fraction is not feasible. A prominent feature of the bimodal density distribution of a partially condensed cloud is the kink between the superfluid core and the thermal wing [71]. However, this feature is totally lost in the parity projection.

In Fig. 5.3(b),(c) we plot both Mott insulator data sets from Fig. 5.2 versus the local chemical potential. In a single image, we mapped out an entire line in the phase diagram as illustrated in Fig. 5.3(a). The slightly different temperatures of the two Mott insulators are clearly visible in the different widths of the variance curves.

Entropy per particle

Our measurements also confirm that the entropy is concentrated around the Mott insulating regions, whereas in the center of a Mott insulator, for local chemical potentials of $\mu_{\mathrm{loc}} = (n + 1/2)\,U$ with an integer n, number fluctuations are completely suppressed and the entropy density is essentially zero. We use the fitted temperature and chemical potential to calculate the original atom number distribution $P_r(n)$ without parity projection. As can be seen in Fig. 5.3(b), the deviation from the perfect integer filling due to thermal excitations is smallest in the center of the $n = 1$ Mott shell at a local chemical potential of $\mu_{\mathrm{loc}} = 0.5\,U$. Therefore we insert the radius corresponding to $\mu_{\mathrm{loc}} = 0.5\,U$ into $P_r(1)$ to extract the maximum of the theoretical probability for unity occupation. For the lowest observed temperature of $T = 0.074(5)\,U/k_B$ we calculate a 99.7(1)% probability for unity occupation in the center of the $n = 1$ Mott-insulating plateau.

We can furthermore calculate the local entropy per lattice site as

$$S_{\mathrm{loc}}(r) = -k_B \sum_n P_r(n) \ln[P_r(n)]. \tag{5.8}$$

Summing the density and entropy density over the lattice sites, we calculate the total number of particles $N = 529(8)$ and the total entropy $S = k_B \cdot 180(12)$ given the fitted values of T and μ from the $n = 2$ data of Fig. 5.2. We find a mean entropy per particle

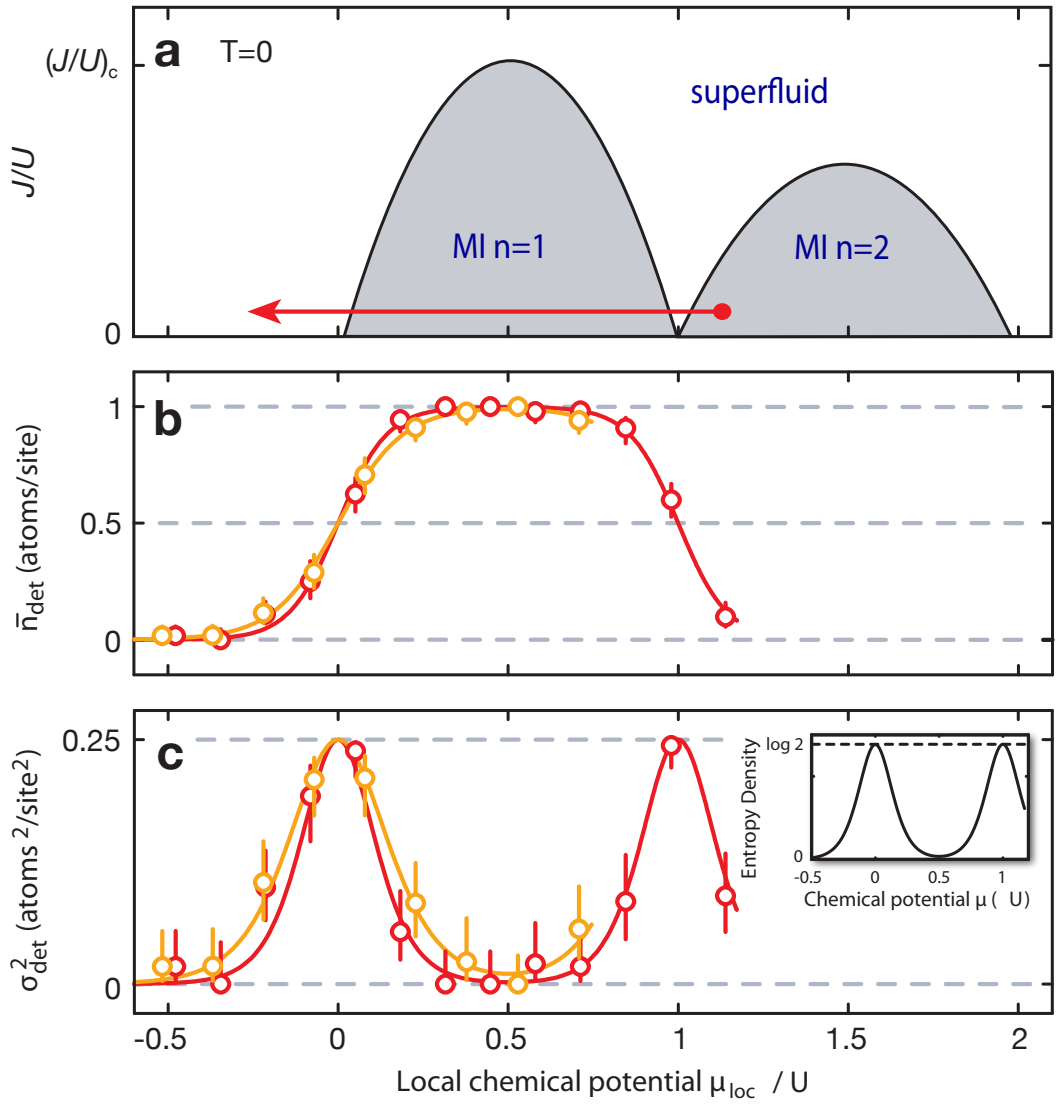

Figure 5.3: Atom density and variance versus local chemical potential. (a) Schematics of the Bose-Hubbard phase diagram ($T = 0$) showing the transition between the characteristic Mott insulating lobes and the superfluid region. The red line starting at the maximum chemical potential μ shows the part of the phase diagram existing simultaneously at different radii in the trap due to the external harmonic confinement. (b),(c) The data from Fig. 5.2 plotted versus the local chemical potential using the local-density approximation [Eq. (5.6)]. The inset to (c) is the entropy density calculated for the displayed $n = 2$ Mott insulator.

$S/N = k_B \cdot 0.34(2)$. This is around the critical entropy for quantum magnetism, which is estimated to be between $(S/N)_c = k_B \cdot 0.34$ [127] and $(S/N)_c \sim k_B \cdot 0.5$ [128].

5.5 *In situ* thermometry

Thermometry in optical lattices is notoriously difficult [8]. Usually the temperature is determined by measuring the temperature before loading into the lattice and again after loading back into a harmonic trap and comparing the entropies calculated from the temperatures and the trap geometry [129, 130]. Our method constitutes a single-image *in situ* thermometer for the atomic limit, from which the entropy can be straightforwardly calculated [Eq. (5.8)]. It relies on the simple analytic expression of the density profile for the atomic limit. In the strongly correlated regime, there are no simple analytic expression and a direct temperature measurement is difficult. However, the entropy of the system can be estimated from measurements of the temperature in the atomic limit.

Range of the thermometer

A Mott insulator at zero temperature has shells with perfectly sharp edges at positions where the local chemical potential μ_{loc} is an integer multiple of U. Temperature washes out these edges and the width of the transition from one integer filling to the next is used to determine the temperature. However, there are also other effects which wash out the edges and therefore set the lowest detectable temperature. The most fundamental effect is the graininess of the lattice. The square lattice and the circular shell structure are incommensurate and therefore a perfectly sharp edge can only be approximated by occupations on the lattice. We apply a fit to simulated data of an $n = 2$ Mott insulator at $T = 0$ and find a temperature of $T_{\mathrm{min}} = 0.02\,U/k_B$. This is the lower bound given by the graininess of the lattice. It could be reduced via a smaller external confinement, i.e. a larger system, in which the graininess of the lattice is less important. For all practical purposes, however, this should not be a limitation.

The single-shot temperature measurement also relies on well-characterized potentials, which allow to convert the position to a local chemical potential. We measured the trap frequencies of the external confinement via excitation of the dipole mode and the low damping rates indicate a good quality of the harmonic confinement. We don't expect to probe the inharmonic part of the potential, because the radius of a $n = 2$ Mott insulator is about 7 μm, while the $1/e^2$ waist radius of the lattice beams is 75 μm. We find a small ellipticity ϵ of our clouds, given by the two trapping frequencies $\omega_x/(2\pi) = 72(4)$ Hz and $\omega_y/(2\pi) = 83(4)$ Hz as $\epsilon = 1 - \omega_x/\omega_y = 13(1)\%$. In the azimuthal averages, we correct for this ellipticity. We estimate the effect of badly

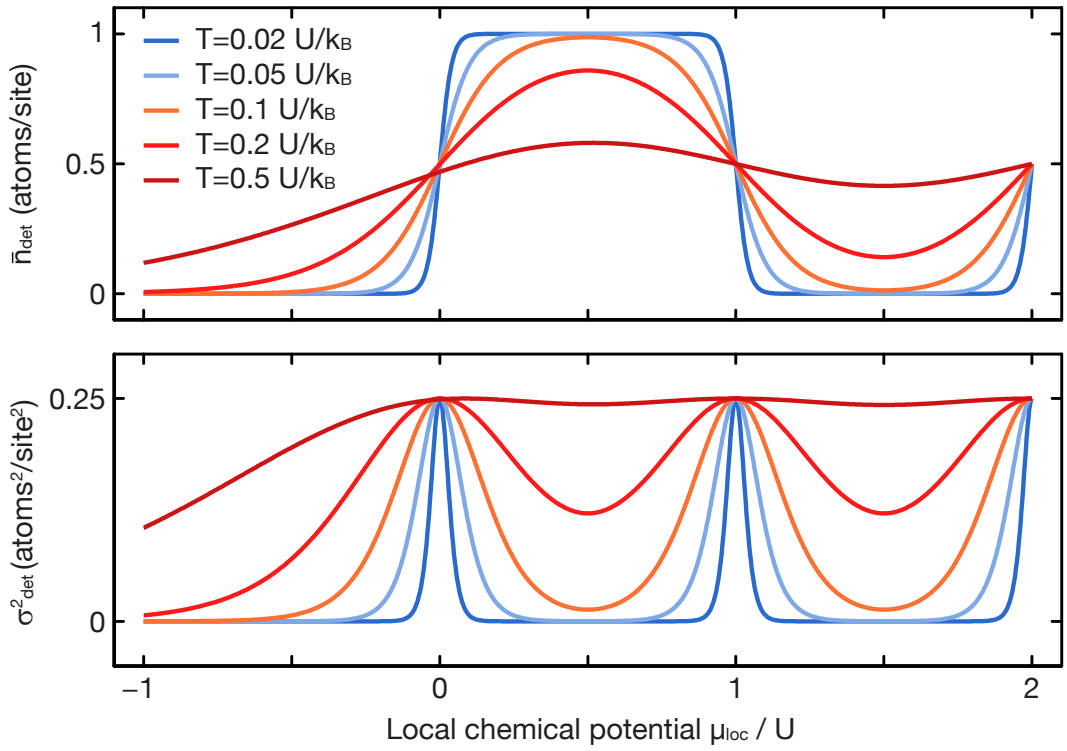

Figure 5.4: Calculated mean density and variance as a function of local chemical potential according to Eq. (5.7) for different temperatures (compare Ref. [131]).

compensated ellipticity, by fitting to simulated data at $T = 0$ as above, but adding an ellipticity in the azimuthal averaging. We find that an ellipticity of $\epsilon = 5\%$ hardly changes the lowest detectable temperature $T_{\mathrm{min}} = 0.02\,U/k_B$, while an ellipticity of $\epsilon = 10\%$ increases it to $T_{\mathrm{min}} = 0.04\,U/k_B$. We conclude that we are not limited by our uncertainty of the ellipticity.

The highest detectable temperature T_{max} is given by the melting of the Mott insulator at $T \lesssim U/k_B$. Fig. 5.4 shows the atom number distribution as a function of local chemical potential according to Eq. (5.7) for different temperatures. The shells are just about visible at $T_{\mathrm{max}} = 0.5\,U/k_B$, and the temperature measurement should work to this point. Without the parity projection, the shells in the density are already washed out at a temperature $T \simeq 0.2\,U/k_B$ [131].

In conclusion, our method is a good thermometer in the range of $T_{\mathrm{min}} = 0.02\,U/k_B$ to $T_{\mathrm{max}} = 0.5\,U/k_B$, which is more than an order of magnitude and covers just the relevant range.

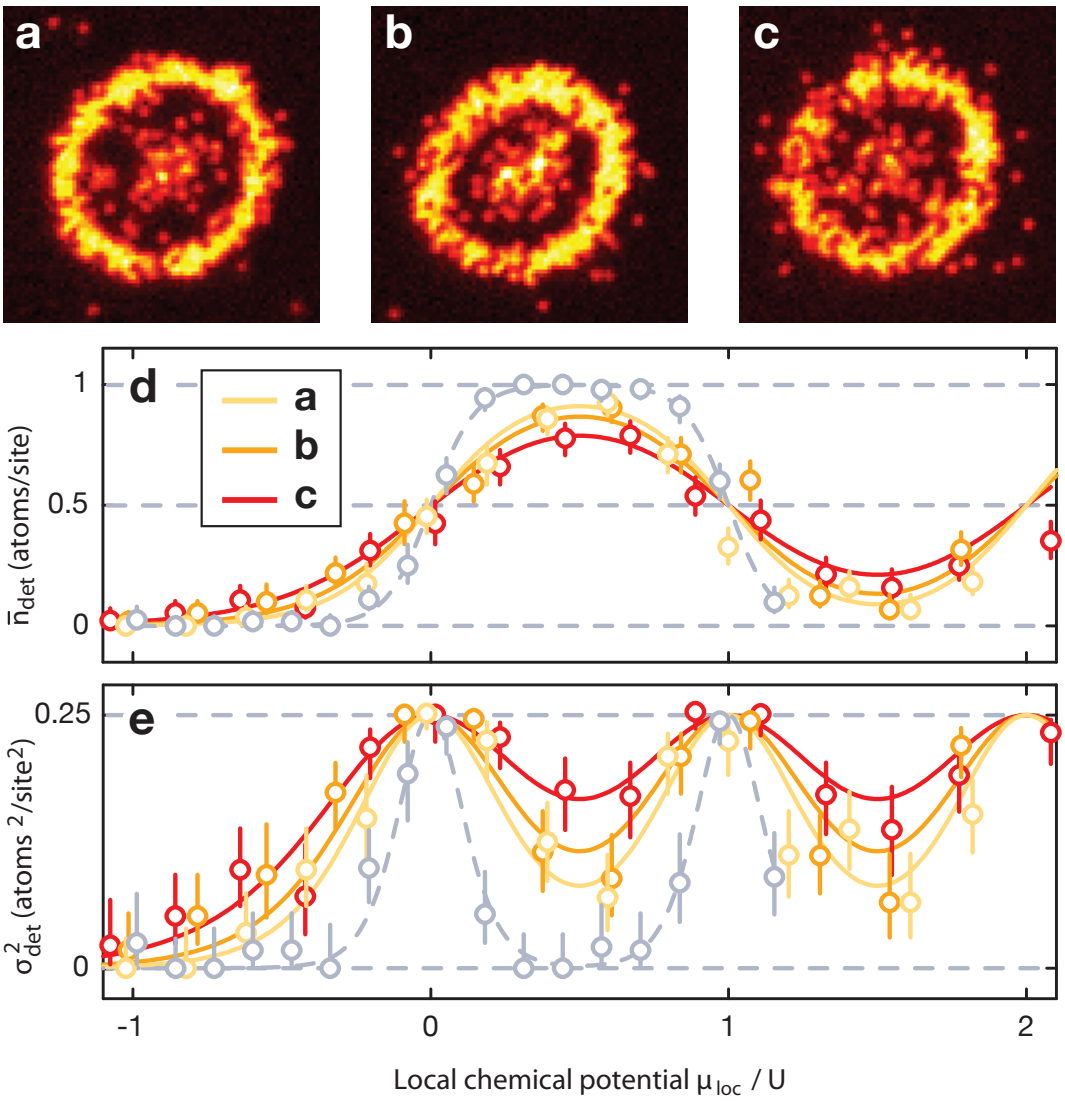

Figure 5.5: Melting of a Mott insulator. (a)-(c) Mott insulators with three different temperatures T, and constant total chemical potential μ in the zero-tunneling limit. For higher temperatures, an increased number of uncorrelated particles or holes appear. In the data shown the pixel were binned 2x2. (d),(e) Profiles of the mean density and its variance as a function of chemical potential, determined as described in the caption of Fig. 5.2 and Fig. 5.3. Yellow, orange and red points correspond to the data sets from (a),(b), and (c), respectively. Light blue points correspond to the low-temperature $n = 2$ Mott insulator of Fig. 5.2(b) with $T = 0.074(5)\,U/k_B$ and $\mu = 1.17(1)\,U$. The parameters extracted from the simultaneous fits to the radial density and variance profiles are $T = 0.17(1)\,U/k_B$, $\mu = 2.08(4)\,U/k_B$, for (a), $T = 0.20(2)\,U/k_B$, $\mu = 2.10(5)\,U/k_B$, for (b) and $T = 0.25(2)\,U/k_B$, $\mu = 2.06(7)U/k_B$, for (c).

Melting of a Mott insulator

We observe how a Mott insulator melts as the temperature (or entropy) of the quantum gas is increased (see Fig. 5.5). At constant total chemical potential but increasing temperatures, one observes that the Mott domains gradually vanish. Although there is no sharp transition to a normal fluid state in this case, Mott plateaus and number squeezing degrade rapidly, once $T \gtrsim 0.2\,U/k_B$ [see Fig. 5.5(d),(e)].

Our method yields the temperature in units of the interaction energy U. This is the relevant energy scale in the atomic limit and only this ratio will enter into the calculation of the thermodynamic properties, e.g. the entropy. If we want to use the atomic limit as a thermometer, we want to extrapolate to other lattice depths with different interaction energies U. For this, we should compare the entropy, because this is the quantity, which is conserved in an adiabatic change of the potential. The temperature in contrast will change with the lattice depth.

We can calculate an absolute temperature using the interaction energy $U = h \cdot 960\,\mathrm{Hz}$ at the end point $V_{x,y} = 23(2)\,E_r$ of the ramp of the lattice depth. Our lowest measured temperature then corresponds to $T = 0.074(5)\,U/k_B = 3.6(3)\,\mathrm{nK}$. However, when ramping deeply into the atomic limit, the tunneling rate and therefore the equilibration rate get exponentially suppressed. At the final lattice depth, the tunnel coupling is only $J = h \cdot 3\,\mathrm{Hz}$. Hence the thermal excitations will be frozen out at a finite depth with some finite tunneling and the final atom distribution will correspond to this depth and interaction energy. Therefore this absolute temperature is only an upper estimate.

5.6 Conclusion

In this chapter, we have shown single-atom resolved images of Mott insulators in the atomic limit. When increasing the atom number, we see how successive shells are formed. Due to the parity projection they show as alternating rings of density one and zero. The symmetry of our external confinement allows us to obtain a radial density and variance profile from an azimuthal average over the data of a single image. We determine the temperature in a single image by fitting the profiles with a simple grand-canonical model. We find temperatures as low as $T = 0.074(5)\,U/k_B$. This corresponds to a 99.7(1)% probability for unity occupation in the center of the $n = 1$ Mott-insulating plateau.

Our pictures show that the entropy is concentrated in the transition regions between the Mott insulator shells and that it is essentially zero in the center of the shells. For our parameters, we calculate a mean entropy per particle of $S/N = k_B \cdot 0.34(2)$, which is around the critical entropy for quantum magnetism. We also show how a Mott insulator melts as the temperature of the quantum gas is increased. Our method constitutes an *in situ* thermometer in the range $0.02 \lesssim k_B T/U \lesssim 0.5$.

We studied the simple case of the atomic limit to set a benchmark and confirm the reliability of our technique. A natural extension would be to probe the strongly correlated state along the quantum phase transition. The same experimental sequence can be used by simply freezing out the distribution at a different lattice depth. This is ongoing work as I write.

6 Single-spin addressing

In this chapter we describe how we manipulate the spin of individual atoms in a Mott insulator with sub-diffraction-limited resolution using a tightly focussed laser beam together with a microwave field. We review the state of the art in Sec. 6.1 and describe our scheme in Sec. 6.2. We show in Sec. 6.3 that we can experimentally prepare arbitrary spin patterns and we discuss the fidelity of the addressing scheme in Sec. 6.4. Some technical details are given in Sec. 6.5 and 6.6 and possible improvements are discussed in Sec. 6.7.

6.1 State of the art

The quest to address single sites of an optical lattice has a long history, which was mainly inspired by the potential applications in quantum information processing. Because typical lattice spacings are on the order of half the lattice wavelength, they cannot be fully optically resolved by a focused laser beam of a similar wavelength. Therefore many proposals have been put forward to overcome this diffraction limit.

One idea is to synthesize a localized optical field with zeros on all other sites of a one-dimensional lattice either using a spatial light modulator [132] or by interference of many tilted laser beams [133]. Another idea is to use a position-dependent atomic population transfer in multi-level systems [134], e.g. exploiting the nonlinear response to the intensity of a control beam in electromagnetically induced transparency [135], in the spirit of stimulated emission depletion microscopy (STED) [136]. A third idea is to use an auxiliary marker atom in a different internal state, which is moved independently from the qubit atoms and initiates the selective spin flips [137, 138].

Experimentally, single-site addressing was demonstrated both spatially, i.e. by focused beams [36, 37, 44], and spectrally, i.e. by selective microwave pulses [41, 93, 139]. Spatial addressing was performed optically in a one-dimensional lattice of 5.3 μm spacing [36] and a two-dimensional microtrap array of 125 μm spacing [37]. In both cases, the lattice sites contained several hundred thermal atoms and tunneling was completely suppressed at these lattice spacings. Two-dimensional addressing of a BEC in a lattice of 600 nm spacing was recently achieved using an electron beam that can be focused to a much smaller spot than light with optical wavelengths [44]. However, spin manipulation was not possible so far, but only depopulation of selected lattice sites.

Spectral addressing was demonstrated with a magnetic field gradient in a sparsely filled one-dimensional lattice of 433 and 532 nm spacing [41, 93] and with an effective

magnetic field at one site of a double well optical lattice [139]. In both cases, selected atoms where shifted into resonance with a microwave field and could be coherently manipulated.

Here we follow a hybrid approach [140, 141], which combines the advantages of spatial and spectral addressing. The differential light shift from a tightly focussed laser beam makes the atoms spectrally addressable via microwave radiation. This method allows to overcome the diffraction limit (Sec. 6.4) and also allows to reach full two-dimensional addressability (Sec. 6.3). The diffraction limit is overcome, because the intensity of the laser beam does not need to vanish at the next atom, but only needs to change as much as to allow to spectrally resolve the change in the differential light shift. Two-dimensional addressing is in principle also possible with magnetic field gradients in two directions [142], but in practice this substantially limits the region of interest.

For the first time, we combine two-dimensional single-atom spin control in strongly correlated systems with high fidelity single-atom detection.

6.2 Addressing scheme

In order to address the atoms in the lattice, we used an off-resonant laser beam focused by the high-resolution imaging system onto individual lattice sites (Fig. 6.1). The laser beam causes a differential light shift of the two relevant hyperfine levels $|0\rangle \equiv |F = 1, m_F = -1\rangle$ and $|1\rangle \equiv |F = 2, m_F = -2\rangle$ and tunes the addressed atom into resonance with an external microwave field at $\sim$6.8 GHz [140, 141]. The σ^--polarized addressing beam had a wavelength of 787.55 nm, between the D_1 and D_2 lines, in order to obtain a large differential light shift between the two hyperfine levels. For perfect σ^--polarization, this 'magic' wavelength generates a light shift only for state $|1\rangle$, and leaves state $|0\rangle$ unaffected (see Fig. 6.2). The beam had a diameter of $\sim$ 600 nm full-width at half-maximum (FWHM) and could be moved in the object plane over the entire field of view by changing its angle of incidence into the microscope objective with a two-axis piezo mirror. We were able to position the beam with an accuracy better than 0.1 a_{lat} using an independent calibration measurement of its position together with a feedback that tracks the slowly varying lattice phases (see Sec. 6.5).

If the addressing laser beam is perfectly centered onto one lattice site [see Fig. 6.1(b)], the differential light shift is $\Delta_{\mathrm{LS}}/(2\pi) \simeq -70$ kHz, whereas a neighboring atom only experiences 10% of the maximum intensity. The resulting difference in light shifts can be well resolved spectrally by our microwave pulses. In order to flip the spin, we performed Landau-Zener sweeps yielding a near flat-top frequency spectrum with a maximum population transfer efficiency of $\sim$ 95%. The microwave sweeps are HS1-

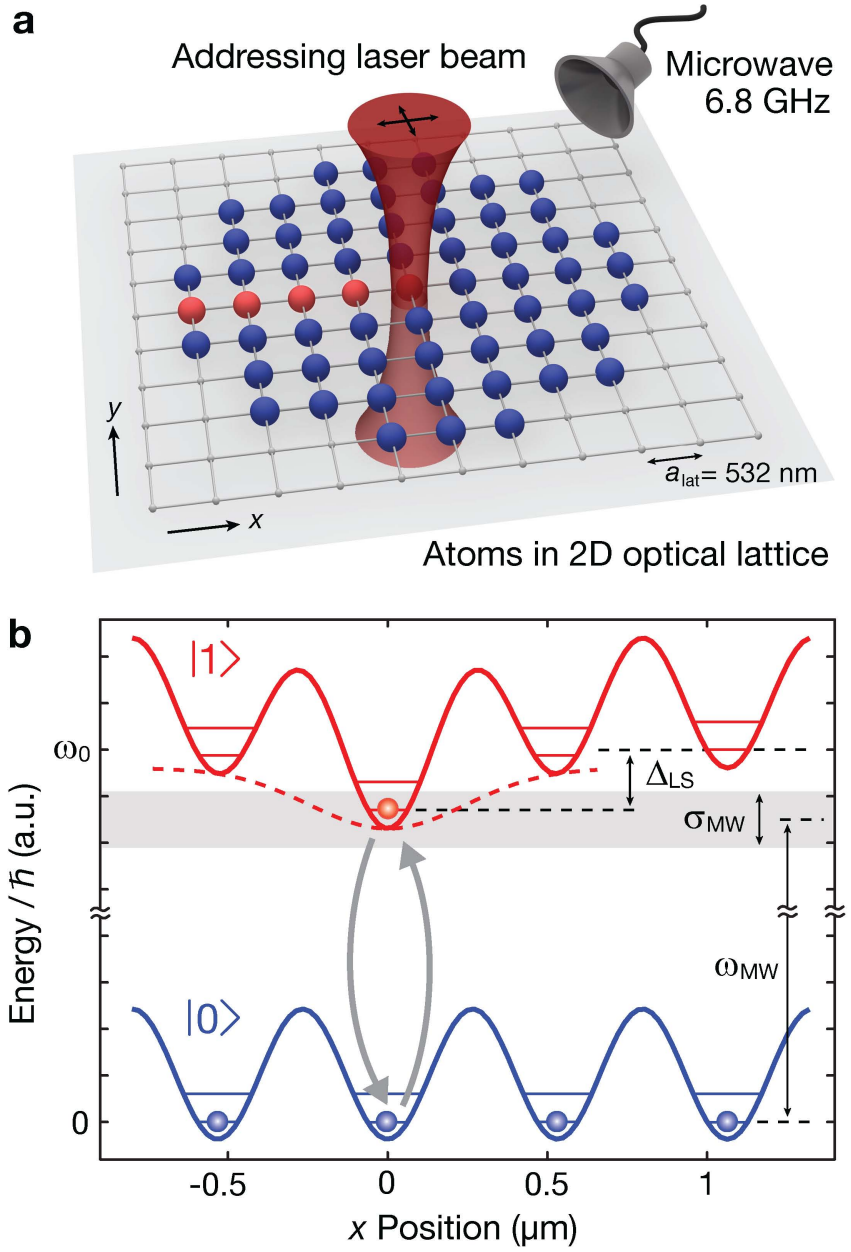

Figure 6.1: Addressing scheme. (a) Atoms in a Mott insulator with unity filling arranged on a square lattice with period $a_{\mathrm{lat}} = 532\,\mathrm{nm}$ were addressed using an off-resonant laser beam. The beam was focussed onto individual lattice sites by a high-aperture microscope objective (not shown) and could be moved in the xy plane with an accuracy of better than $0.1\,a_{\mathrm{lat}}$. (b) Energy diagram of atoms in the lattice for the two hyperfine states $|0\rangle$ and $|1\rangle$. The σ^--polarized addressing beam locally induces a light shift Δ_{LS} of state $|1\rangle$, bringing it into resonance with a microwave field. A Landau-Zener sweep (central frequency ω_{MW}, sweep width σ_{MW}) transfers the addressed atoms from $|0\rangle$ to $|1\rangle$.

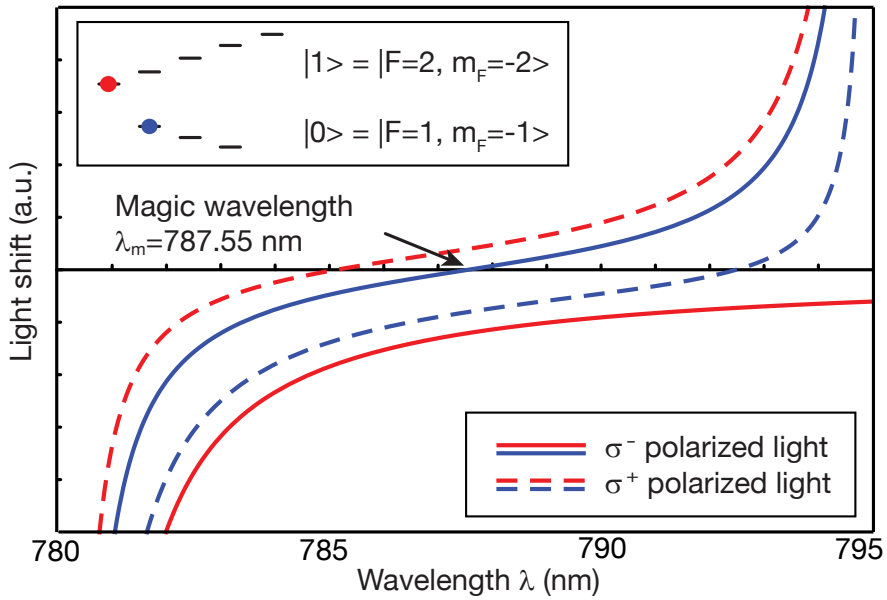

Figure 6.2: Differential light shift. The figure shows the light shift on state $|0\rangle$ (blue) and on state $|1\rangle$ (red) as a function of wavelength for σ^- (solid lines) and σ^+ (dashed lines) polarization. At the magic wavelength of $\lambda_m = 787.55\,\text{nm}$, state $|0\rangle$ experiences no light shift in the case of perfect σ^- polarization due to a cancelation of the light shifts arising from the coupling to the D1 (795 nm) and D2 (780 nm) line. The light shift on the $|1\rangle$ state for σ^- polarization does not diverge at the D1 line, because there is no state with $m_F = -3$ in the $5S_{1/2}$ manifold to couple to.

pulses [143] with time-dependent Rabi frequency $\Omega(t)$ and detuning $\delta(t)$ given by

$$\Omega(t) = \Omega_0 \,\text{sech}\left[\beta\left(\frac{2t}{T_p} - 1\right)\right] \tag{6.1}$$

$$\delta(t) = \frac{\sigma_{\text{MW}}}{2} \tanh\left[\beta\left(\frac{2t}{T_p} - 1\right)\right], \tag{6.2}$$

where $\Omega_0/(2\pi) = 3\,\text{kHz}$ is the maximum Rabi-frequency, $\beta = 5$ is a truncation factor, $T_p = 20\,\text{ms}$ is the pulse duration, and $\sigma_{\text{MW}}/(2\pi) = 60\,\text{kHz}$ is the sweep width. The detuning $\delta(t)$ is measured relative to the center of the sweep at $\omega_{\text{MW}} = \omega_0 - \Delta_{\text{MW}}$ [see Fig. 6.1(b)]. Here, ω_0 is the bare resonance between the two hyperfine states, including the shift of -570 kHz due to the magnetic bias field along the z direction and $\Delta_{\text{MW}}/(2\pi) = -75\,\text{kHz}$ denotes the offset of the sweep center.

6.3 Writing arbitrary spin patterns

As a first experiment, we sequentially flipped the spin of the atoms at selected lattice sites in our Mott insulator with unity filling and spin state $|0\rangle$ (see Fig. 6.3(a) and Ch. 5). The lattice depths were first changed to $V_x = 56\,E_r$, $V_y = 90\,E_r$ and $V_z = 70\,E_r$ in order to completely suppress tunneling even when the addressing beam locally perturbs the lattice potential. For each lattice site, we then switched on the addressing laser beam with an s-shaped ramp within 2.5 ms, which is adiabatic with respect to the on-site oscillation frequency of ~ 30 kHz. Subsequently, a microwave pulse with the parameters described above produced spin-flips from $|0\rangle$ to $|1\rangle$. The addressing laser was switched off again within 2.5 ms, before its position was changed in 5 ms to address the next lattice site.

For the image of Fig. 6.3(a), this procedure was repeated 16 times in order to flip the spins along a line. Finally, a 5 ms 'push-out' laser pulse, resonant with the $F = 2$ to $F' = 3$ transition, removed all addressed atoms in state $|1\rangle$. In order to reveal only the spin-flipped atoms, the spin states of all atoms were flipped by a global microwave sweep before the push-out laser pulse was applied [Fig. 6.3(c),(d)]. However, due to the finite transfer efficiency of the global sweep, some atoms remaining in state $|0\rangle$ were clearly visible in addition to the addressed ones. To avoid this problem when detecting the addressed atoms, we initially transferred the whole sample to state $|1\rangle$ by a microwave sweep and then shone in a repumping laser that completely depopulated state $|0\rangle$. Then, we used our addressing scheme to transfer selected atoms back to $|0\rangle$ and subsequently pushed out the atoms in $|1\rangle$, yielding typical images as shown in Fig. 6.3(b),(e),(f).

By the deterministic creation of arbitrary two-dimensional spin patterns of individual atoms, we realize a scalable single-atom source [35, 107, 144].

6.4 Spin-flip fidelity

We quantified the success rate of our addressing scheme by producing a series of spin-flips along the y lattice axis in a Mott insulator with unity filling (see Fig. 6.4). The experimental procedure was the same as described above for the realization of Fig. 6.3(a), in which the addressed sites were detected as empty sites. From the reconstructed atom number distribution [Fig. 6.4(a)], we determined the probability $p_0(\delta x)$ of finding an empty site as a function of the pointing offset δx between the addressing beam and the center of the lattice site [see Fig. 6.4(b)]. We also investigated the effect of the addressing procedure on next neighboring atoms, which ideally should remain unaffected. For this purpose, we monitored the probability of finding a hole at the sites next to the addressed ones [dark blue regions in Fig. 6.4(a),(b) and dark blue data points in Fig. 6.4(c)]. In order to distinguish accidentally flipped neighboring atoms from holes that originate from thermal excitations of the initial Mott insulator

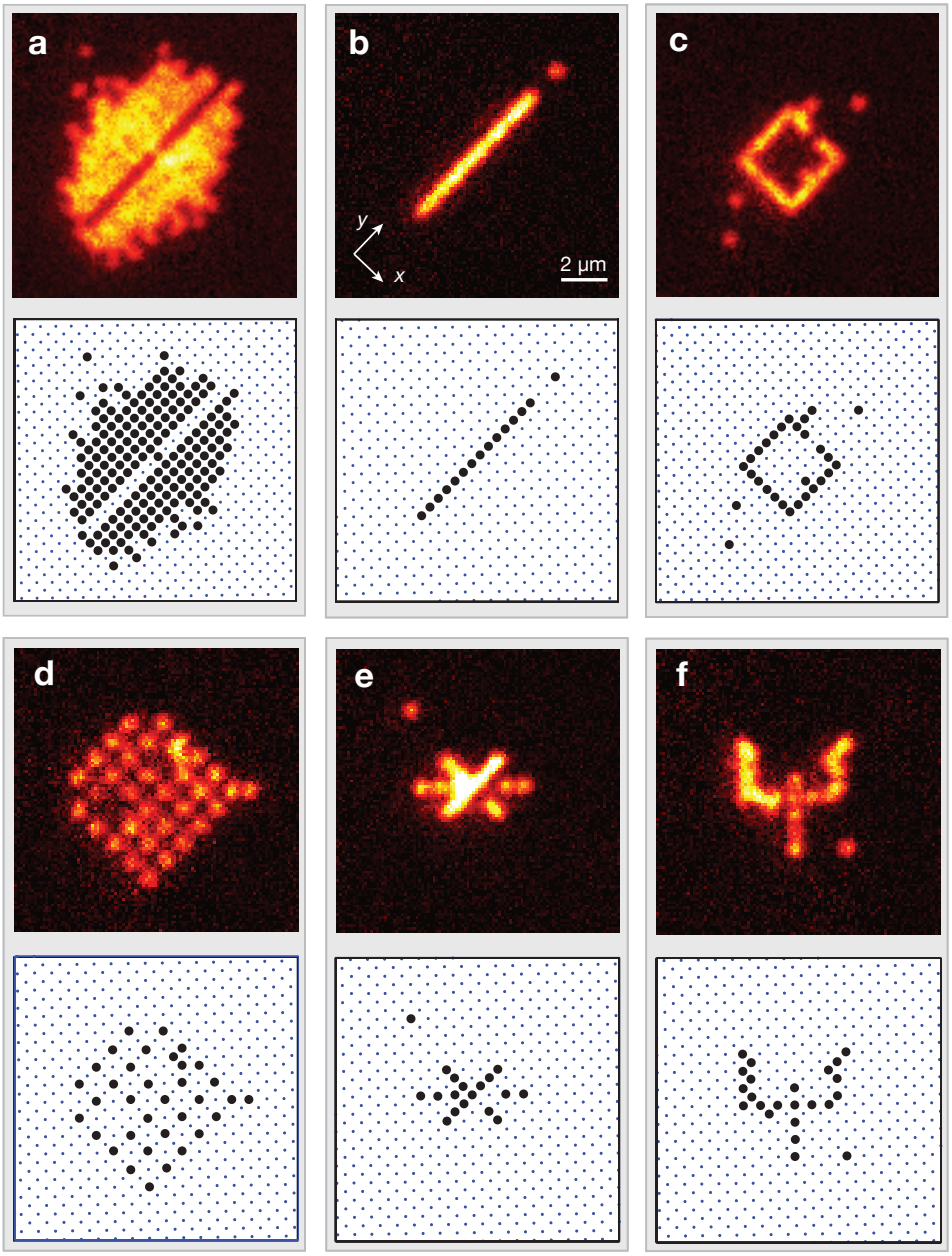

Figure 6.3: Single-site addressing. (a) Experimentally obtained fluorescence image of a Mott insulator with unity filling in which the spin of selected atoms was flipped from $|0\rangle$ to $|1\rangle$ using our single-site addressing scheme. Atoms in state $|1\rangle$ were removed by a resonant laser pulse before detection. The lower part shows the reconstructed atom number distribution on the lattice. Each circle indicates a single atom, the points mark the lattice sites. (b)-(f), Same as (a), but a global microwave sweep exchanged the population in $|0\rangle$ and $|1\rangle$, such that only the addressed atoms were observed. The line in (b) shows 14 atoms on neighboring sites, the images (c)-(f) contain 29, 35, 18 and 23 atoms, respectively. The single isolated atoms in (b),(e),(f) were placed intentionally to allow for the correct determination of the lattice phase for the feedback on the addressing beam position.

(Ch. 5), we also monitored the probability of finding a hole at the second next neighbors (light blue regions and data points in Fig. 6.4). As both yielded the same hole probability of 6(2)%, we attribute all holes to thermal excitations and conclude that the probability of addressing a neighboring atom is indiscernibly small.

We fitted the hole probability $p_0(\delta x)$ of the addressed site with a flat-top model function, given by

$$p_0(\delta x) = \frac{A}{2}\left[\mathrm{erf}\left(\frac{\delta x + \sigma_a/2}{\sigma_s}\right) + \mathrm{erf}\left(-\frac{\delta x - \sigma_a/2}{\sigma_s}\right)\right] + B. \tag{6.3}$$

Here, $\mathrm{erf}(x) = 2/\sqrt{\pi}\int_0^x e^{-\tau^2} d\tau$ is the error function, σ_a denotes the full-width at half-maximum of the flat-top profile and σ_s the edge sharpness. The offset B is kept fixed at the thermal contribution of 6%. We chose this model function since our HS1-pulses produce a flat-top population transfer profile, the edges of which are dominated by randomly fluctuating quantities (beam pointing and magnetic fields) following Gaussian statistics. The addressing fidelity is defined as $F = A/(1-B)$ taking into account that the maximum hole probability $p_0^{\max} = A + B$ also includes holes from thermal defects. These yield a hole with probability B at unsuccessfully addressed sites which occur with probability $1 - F$, such that $p_0^{\max} = F + (1-F)B$. From the fit, we derived a spin-flip fidelity of 95(2)%, a full-width at half-maximum of $\sigma_a = 330(10)$ nm and an edge sharpness of $\sigma_s = 50(10)$ nm [Fig. 6.4(c)]. These values correspond to 60% and 10% of the addressing beam diameter, demonstrating that our method reaches sub-diffraction-limited resolution, well below the lattice spacing.

The observed maximum spin-flip fidelity is currently limited by the population transfer efficiency of our microwave sweep. The edge sharpness σ_s originates from the beam pointing error of $\lesssim 0.1\, a_{\mathrm{lat}}$ and from variations in the magnetic bias field. The latter causes frequency fluctuations of ~ 5 kHz, which translate into an effective pointing error of $0.05\, a_{\mathrm{lat}}$ at the maximum slope of the addressing beam profile. The resolution σ_a could in principle be further reduced by a narrower microwave sweep, at the cost of a larger sensitivity to the magnetic field fluctuations. A larger addressing beam power would reduce this sensitivity, but we observed that this deformed the lattice potential, due to the imperfect σ^--polarization, allowing neighboring atoms to tunnel to the addressed sites.

6.5 Positioning of the addressing beam

Calibration of the addressing beam position

To move the addressing laser beam in the object plane, we changed the angle of the beam entering from the reverse direction into the microscope objective using a two-axis piezo mirror (S-334 Physik Instrumente GmbH & Co. KG, Karlsruhe). The device has an angular resolution of 5 μrad, corresponding to a theoretical resolution in the

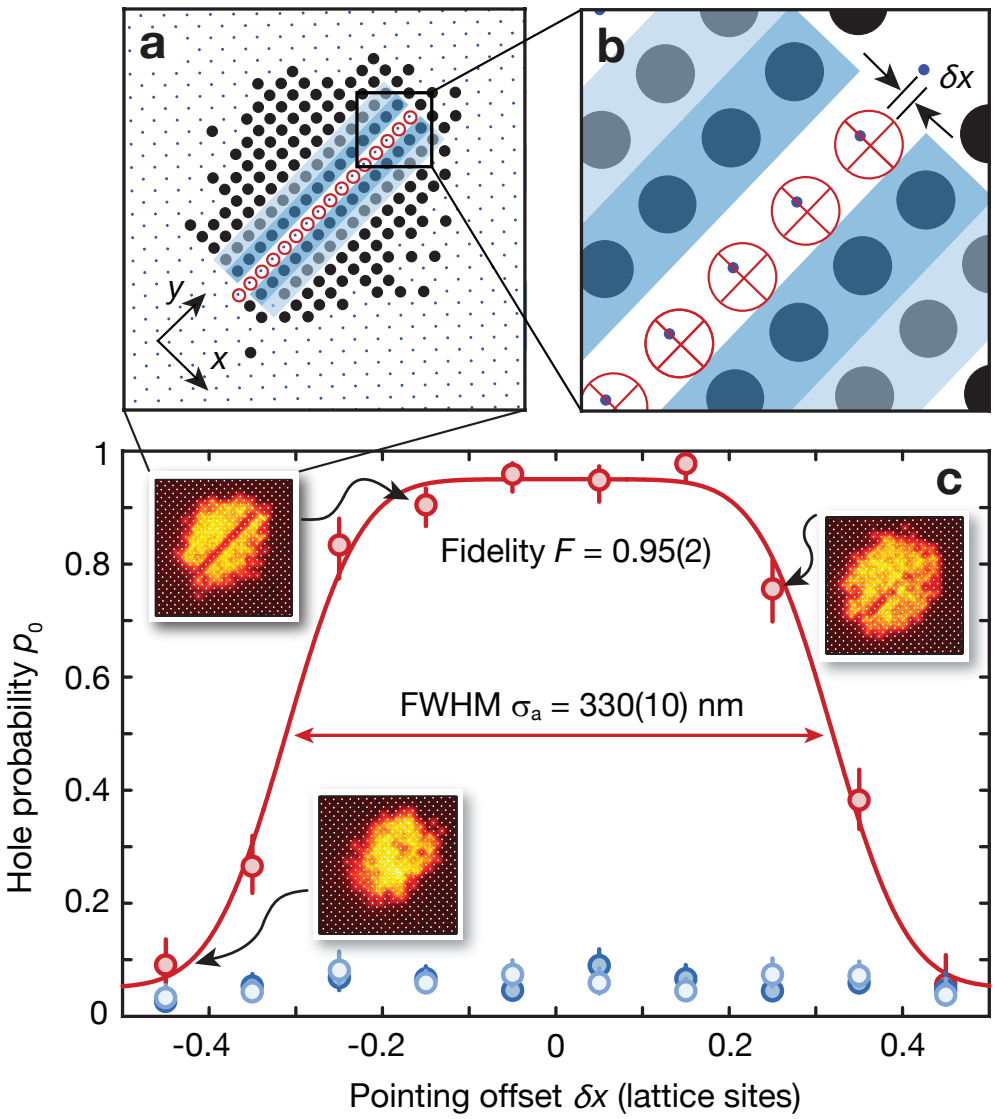

Figure 6.4: Addressing fidelity. The spin-flip probability was measured by sequentially addressing a series of 16 neighboring sites along the y lattice axis [red circles in (a)] in a Mott insulator with unity filling. The red data points in (c) show the resulting hole probability $p_0(\delta x)$ as a function of the pointing offset δx, as defined in (b). Each point was obtained by averaging over 4-7 pictures (total 50-100 addressed lattice sites), taking only those sites into account which lie well within a Mott shell with unity filling. The displayed error bars show the 1σ statistical uncertainty, given by the Clopper-Pearson confidence limits. The data was fitted by a flat-top model function [Eq. (6.3)] and yields a full-width at half-maximum $\sigma_a = 330(10)$ nm, an edge sharpness of $\sigma_s = 50(10)$ nm, and a peak fidelity of 95(2)%. The offset was fixed at the 6(2)% probability of thermally activated holes as deduced from the next neighboring and second next neighboring sites [blue shaded regions in (a),(b) and blue points in (c)].

object plane of 10 nm$\simeq 0.02\,a_{\mathrm{lat}}$. In order to position the addressing laser beam onto the atoms with high precision, we measured calibration functions that translate the two control voltages of the piezo mirror into image coordinates. This calibration was performed by replacing the far detuned addressing laser beam by a near resonant molasses beam that follows the identical beam path. Using in addition the x and y molasses beams, we took a fluorescence image of a large thermal atom cloud in the vertical lattice alone and observed a strongly enhanced signal at the position of the focused beam [see Fig. 6.5(c)]. We determined the position of this fluorescence maximum with an uncertainty of 0.2 pixels in our images, corresponding to $0.05\,a_{\mathrm{lat}} = 25$ nm in the object plane [see Fig. 6.5(d)]. The long term drifts of the addressing beam position are on the order of $0.1\,a_{\mathrm{lat}}$ per hour, which we took into account by regular recalibration of the beam position.

Lattice phase feedback

In order to compensate slow phase drifts of the optical lattice, we applied a feedback on the position of the addressing beam. We determined the two lattice phases (offsets of the position of the lattice sites) along the x and y direction after each realization of the experiment by fitting the position of isolated atoms (see Fig. 6.5(a), the isolated atom is marked by a circle). Averaging over the positions of typically 1-5 isolated atoms per image allowed us to determine the lattice phase to better than $0.05\,a_{\mathrm{lat}}$. For the determination of the phase, we used the lattice constant a_{lat} and the lattice angles determined from a fluorescence image with many isolated atoms (Sec. 4.4). We find that the phases slowly drift over many lattice sites [see Fig. 6.5(b)], showing an oscillation with an amplitude of $3\,a_{\mathrm{lat}}$ and a period of about 80 min. The same period is found in the drift of the temperature above the experimental table. The amplitude of 3°C should make a difference in wavelength of $\Delta\lambda_{\mathrm{lat}}/\lambda_{\mathrm{lat}} = 3 \cdot 10^{-6}$ due to the change in the refractive index of the air. The beam path in air from the vacuum chamber to the retro-reflecting mirror is about $L = 2 \cdot 100\,\mathrm{mm} = 2 \cdot 10^5\,\lambda_{\mathrm{lat}}$, so the change in length is $\Delta L = (\Delta\lambda_{\mathrm{lat}}/\lambda_{\mathrm{lat}}) \cdot L = 3 \cdot 10^{-6} \cdot 2 \cdot 10^5 \lambda_{\mathrm{lat}} = 0.6\,\lambda_{\mathrm{lat}} = 1.2\,a_{\mathrm{lat}}$. The fact that the phases in x and y direction drift along further supports this interpretation and a better temperature stabilization is certainly necessary. Since our phase drifts were slower than $0.04\,a_{\mathrm{lat}}$ between two successive realizations of the experiment ($\simeq$25 s cycle time), we used the lattice phase from the previous image to correct the addressing beam position. The feedback was done by adding appropriate offsets to the piezo control voltages.

Table 6.1 summarizes the positioning errors. We estimate that we can position the addressing beam with respect to the lattice with a total error of $\sim 0.1 a_{\mathrm{lat}} = 50$ nm, consistent with the edge sharpness $\sigma_s = 50(10)$ nm in our fidelity curve (see Fig.6.4).

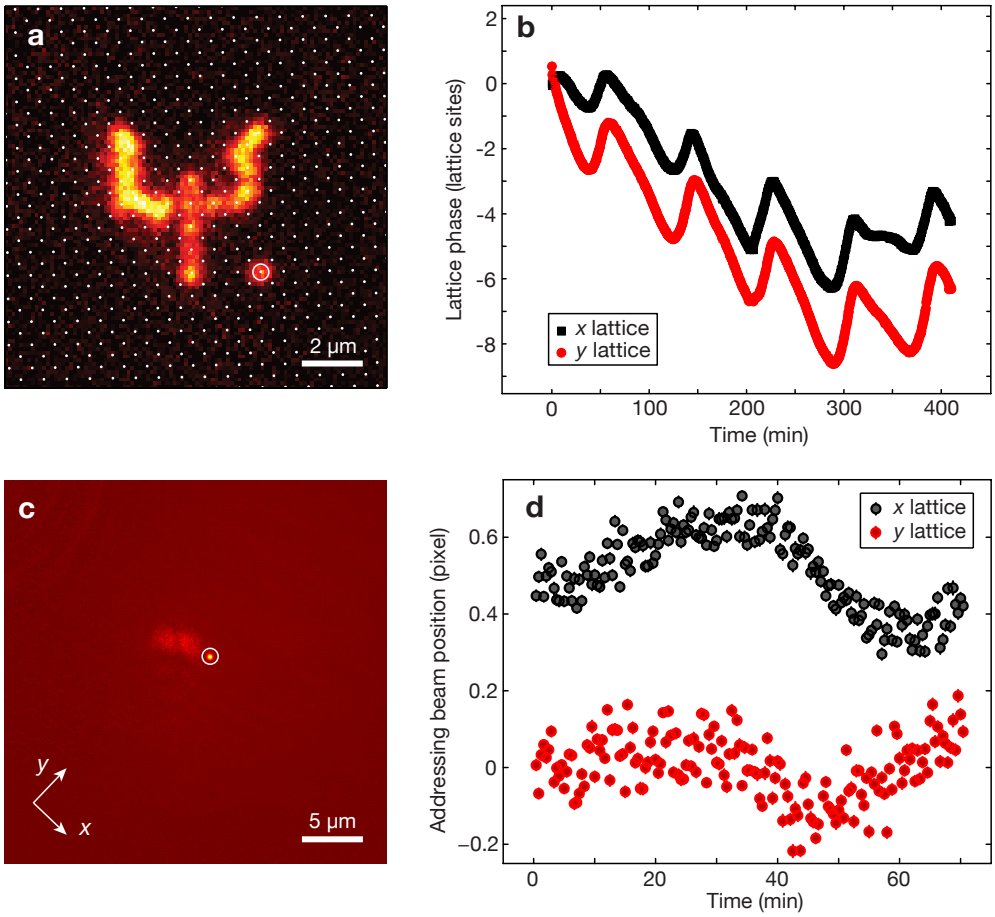

Figure 6.5: Positioning of the addressing beam. (a) The lattice phase is determined from the position of isolated atoms, which are placed intentionally. The phase is evaluated online and fed forward to the addressing beam. (b) The lattice phases drift over several sites over the day. The maximal drift between two successive sequences is however only $0.4\,a_{\mathrm{lat}}$. (c) The position of the addressing beam is determined from the increased fluorescence at its position, when it is replaced by an additional molasses beam. The increase in signal is so large that the fluorescence from the rest of the cloud is not visible on this scale. The feature to the left is stray light from this beam. (d) The drifts of the addressing beam position are smaller than $0.5\,a_{\mathrm{lat}}$.

6.6 Calibration of the light shift

Microwave spectra in the addressing beam

We calibrated the differential light shift of the addressing beam via microwave spectra of atoms loaded into the beam. This makes the measurement independent of the positioning errors of the addressing beam.

Error source	Error
Resolution of mirror	0.02 a_{lat}
Determination of lattice phase	$< 0.05\ a_{\mathrm{lat}}$
Drifts of lattice phase (per cycle)	$< 0.04\ a_{\mathrm{lat}}$
Determination of addressing beam position	0.05 a_{lat}
Overall	$\sim 0.1 a_{\mathrm{lat}}$

Table 6.1: Error budget for the positioning of the addressing beam with respect to the lattice sites.

For perfect σ^- polarization, the beam at the magic wavelength should only trap atoms in state $|F = 2, m_F = -2\rangle$, while atoms in $|F = 1, m_F = -1\rangle$ should see no light shift. Therefore, even when we load it from a cloud prepared in $|F = 1, m_F = -1\rangle$, we mostly load $|F = 2, m_F = -2\rangle$ into the beam, because there are enough atoms in the wrong spin state. Indeed, an optical push out on the $F = 2$ to $F' = 3$ transition did remove the atoms from the addressing beam and therefore confirmed that the trapped atoms were in the $|F = 2, m_F = -2\rangle$ state. For the spectrum, we applied an HS1 microwave sweep of 30 ms duration, which transfered the atoms down to the $|F = 1, m_F = -1\rangle$ state, where they were lost from the trap. The resonance therefore shows as a dip in the atom number (see Fig. 6.6).

In order to count the remaining atoms, we loaded them into a 3D lattice of $V_x = V_y = 3.5\, E_r$ and $V_z = 57\, E_r$ depth. When we let them tunnel for 100 ms in this weak horizontal lattice, they spread over a diameter of $\sim 10\,\mu$m. We then ramped up the lattice to freeze the distribution and took a fluorescence image. At this dilute filling of the lattice, the probability for two atoms at the same lattice sites is very low and we can neglect losses due to the parity projection. The method is therefore a very reliable way to count small numbers of atoms.

Fig. 6.6(a) shows the resulting spectra for different addressing beam powers. We loaded around 50 atoms into the addressing beam and lost all of them for resonant transfer. The microwave frequency is given relative to the bare transition in the absence of magnetic fields. The addressing beam shifts the transition to smaller frequencies. For larger addressing beam powers, the resonance does not fully drop to zero atoms, because some $|F = 1, m_F = -1\rangle$ atoms are trapped due to the imperfect polarization.

In order to measure the bare transition including the bias magnetic field, but not the light shift from the addressing beam, we took a spectrum inside the lattice. We loaded the atoms from the addressing beam in order to have only $|F = 2, m_F = -2\rangle$ atoms and then performed the microwave sweep to the $|F = 1, m_F = -1\rangle$ state inside the lattice. Atoms which were not transferred were then removed with an optical push out on the $F = 2$ to $F' = 3$ transition and the resonance shows as surviving

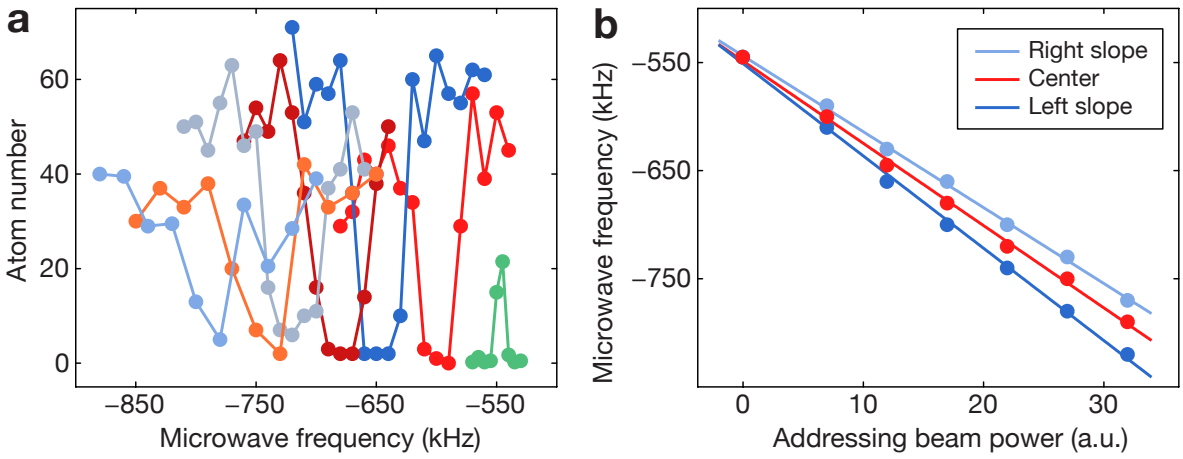

Figure 6.6: Microwave spectra in the addressing beam for the calibration of the differential light shift. (a) Remaining atom number versus the microwave sweep center for different beam depths and bare transition without addressing beam (green data points). (b) Frequencies of the center and the slopes of the resonances for different beam powers.

atoms [green data points in Fig. 6.6(a)]. The transition is shifted by $-550\,\mathrm{kHz}$ from the bare transition by the applied vertical magnetic field of 260 mG. By repeating this measurement we found that scatter in the magnetic bias field causes frequency fluctuations of $\sim 5\,\mathrm{kHz}$. Fig. 6.6(b) shows the center and the slopes of the resonances in Fig. 6.6(a) as a function of the addressing beam power.

Quality of the polarization

In order to obtain a differential light shift, as used in our addressing scheme, it is essential to have circular polarized light. This is challenging, because the addressing beam has to pass many optical elements, which can spoil the polarization. The beam is overlapped with the imaging path via an uncoated glass window (see Fig. 4.2) and the reflection coefficient for the s and the p polarization differ by one order of magnitude. Also the use of silver mirrors, which allow to alternatively work with an addressing beam at 420 nm, spoil the polarization. We therefore used a combination of a three wave plates ($\lambda/4, \lambda/2, \lambda/4$) in the beam path to pre-compensate the effect of these elements, finding the appropriate angles of the wave plates in a separate test setup.

In order to determine the quality of the polarization in the final setup, we need to compare the light shift on the atoms in different magnetic sublevels. We did this by measuring loading curves for the $|F = 2, m_F = -2\rangle$ and the $|F = 1, m_F = -1\rangle$ state (see Fig. 6.7, red and light blue data points, respectively). The curves show the number of trapped atoms versus the addressing beam power for a hold time in the

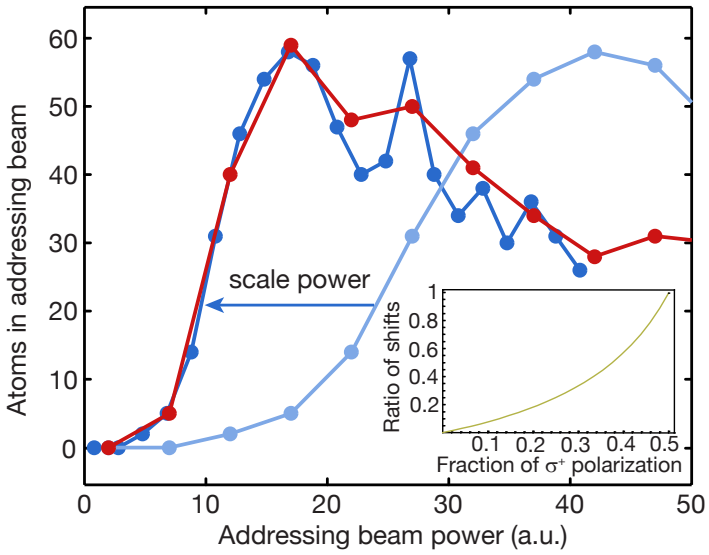

Figure 6.7: Loading curve in the addressing beam. Number of atoms in the addressing beam after 50 ms hold time for the state $|1\rangle$ (red points) and $|0\rangle$ (light blue points). When the addressing beam power for the $|0\rangle$ state is scaled by 40%, the curves coincide (dark blue points). Inset: ratio of the light shifts on state $|0\rangle$ and $|1\rangle$ as a function of the power fraction of the addressing beam in the σ^+ polarization.

addressing beam of 50 ms. We observe a fast initial increase and a slow decay for large depths. We assume that this results from an interplay of the number of bound states with a short lifetime at very high densities. The curve for the $|F = 1, m_F = -1\rangle$ state was recorded by removing the $|F = 2, m_F = -2\rangle$ atoms with an optical push out directly after loading into the addressing beam and again after loading into the 3D lattice.

We find that the curves overlap if we scale the power for the $|F = 1, m_F = -1\rangle$ atoms by 40% (dark blue data points in Fig. 6.7). We assume that the number of atoms only depends on the potential depth and conclude that the $|F = 1, m_F = -1\rangle$ state experiences 40% of the light shift on the $|F = 2, m_F = -2\rangle$ state for the same addressing beam power. A ratio of 40% in the light shifts corresponds to a fraction of 33% of the power in the σ^+ polarization (see inset to Fig. 6.7 and Fig. 6.2). For the differential light shift of $\hbar\Delta_{\mathrm{LS}} = 70\,\mathrm{kHz} = 35\,E_r$, which we used in the addressing experiments, the absolute light shifts are then $\hbar\Delta^1_{\mathrm{LS}} = 1.65 \cdot \hbar\Delta_{\mathrm{LS}} = -58\,E_r$ on state $|F = 2, m_F = -2\rangle$ and $\hbar\Delta^0_{\mathrm{LS}} = 0.65 \cdot \hbar\Delta_{\mathrm{LS}} = -23\,E_r$ on state $|F = 1, m_F = -1\rangle$. These shifts are comparable to the lattice depth itself at which we performed the addressing experiments. Indeed, we observed that a further increase of the addressing beam depth substantially deformed the potential and allowed neighboring atoms to tunnel to the addressed site.

6.7 Possible improvements

In our present scheme, we need 30 ms for each addressed lattice site, which is limited by both the small Rabi frequency of the microwave and the slow movement of the addressing beam. A straight-forward improvement would be to replace the microwave sweep by an optical two-photon Raman transition, which can reach a much faster transfer. We can still use the differential light shift from the addressing beam to shift selected atoms into resonance with the Raman transfer. The Raman laser beams can be large in this case. An alternative is to focus both Raman laser beams onto a single site. In this case, the point spread functions need to be squared for the two-photon process, which would reduce the effect on the neighboring atom to a few percent. When using the transition at 420 nm the effect on the neighbors would be completely negligible.

The velocity of the addressing beam is limited to 5 ms per lattice site by the response time of the piezo mirror. This can be significantly improved to about 2 μs [145], when using an acousto-optical deflector to control the position of the addressing beam [146–148]. This in principle also allows to operate several beams at the same time.

So far, we only performed spin flips driven by frequency sweeps. The scheme is, however, obviously extendable to coherent spin control and would then constitute a single qubit gate. For driving a Rabi oscillation, the technical requirements are somewhat more challenging than for spin flip. The current fluctuations in the background magnetic field and the pointing error cause a scatter in the resonance frequency of the addressed atom of about 5 kHz. In a frequency sweep, one can set the parameters to achieve a transfer despite these fluctuations. In a Rabi oscillation, however, this would directly reduce the fidelity of the manipulation and an even better control would be required to implement a single-qubit gate with a high fidelity.

6.8 Conclusion

In summary, we have demonstrated two-dimensional single-site and single-atom spin control in an optical lattice in the strongly correlated regime. We focus a laser beam onto single lattice sites and thereby locally shift the atomic frequency into resonance with a microwave driving a spin flip. Starting from a Mott insulator with unity filling, we create arbitrary two-dimensional spin patterns of individual atoms, thus realizing a scalable single-atom source. These structures can be used to study ensuing non-equilibrium quantum dynamics. We achieved a spin-flip fidelity of 95(2)% and a sub-diffraction-limited spatial resolution of 330(10) nm which leads to a negligible influence on the neighboring lattice sites. By correcting for slow drifts of the lattice position, we position the addressing beam with respect to the lattice with an error of 50 nm.

7 Tunneling dynamics in a lattice

The ability to prepare arbitrary atom distributions opens up new possibilities for exploring coherent quantum dynamics at the single-atom level. As an example, we studied the one-dimensional tunneling dynamics in a lattice (Sec. 7.2). This allowed us to determine how much our addressing scheme affects the vibrational state of the atoms (Sec. 7.3).

7.1 State of the art

Tunneling processes are among the most intriguing phenomena of quantum mechanics and their direct observation is interesting in itself. Tunneling dynamics on a one-dimensional lattice can be seen as a continuous-time version of a quantum walk in position space, the quantum analog of the random walk. Quantum walks have attracted great theoretical interest due to the potential application in quantum information science [149–152] and their ability to speed up search algorithms compared to their classical counterparts [153].

Experimental realization of the quantum walk have been reported in various physical systems like nuclear magnetic resonance samples [154, 155] or optical systems [156–158], also for photons in an array of evanescently coupled photonic waveguides [159, 160]. The discrete quantum walk of material quantum particles was observed both for trapped ions in phase space [161, 162] and for neutral atoms using a sequence of spin manipulations and spin-dependent transports in an optical lattice [163]. Without single-particle and single-site resolution, a quantum walk in the ground state has been observed for ultracold fermionic atoms by measuring their ballistic expansion in a weak lattice [164].

No measurement so far has observed the ground state tunneling dynamics of massive particles on a lattice with single-site resolution.

7.2 Ground state tunneling dynamics

We started by preparing a single line of up to 18 atoms along the y direction before we lowered the lattice depth along the x direction to $V_x = 5.0(5)\,E_r$ within 200 μs. At the same time, the other lattice depths were lowered to $V_y = 30\,E_r$ and $V_z = 23\,E_r$, which reduced the external confinement along the x direction, but still suppressed tunneling in the y and z directions. After a varying hold time t, allowing the atoms to tunnel along x, the atomic distribution was frozen by a rapid 100 μs ramp of the

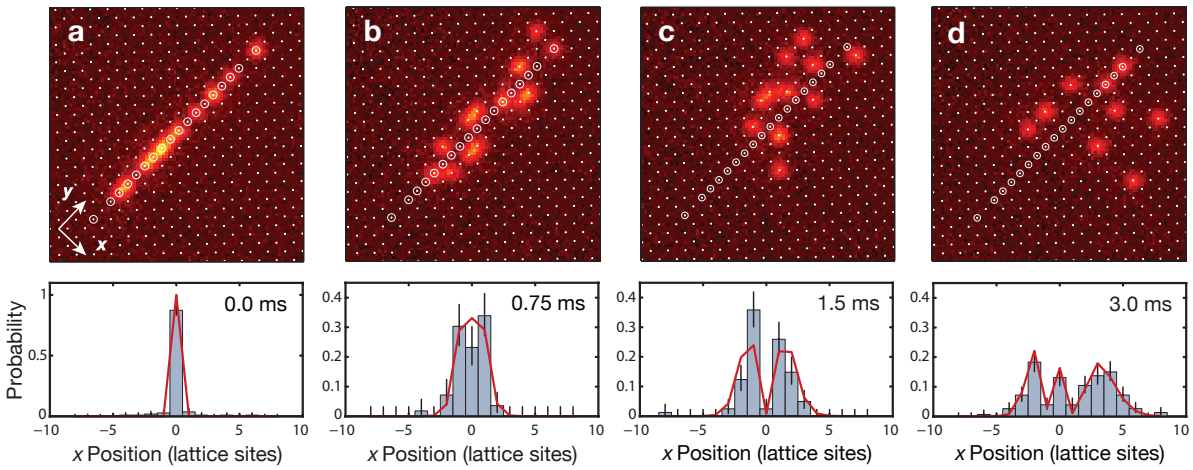

Figure 7.1: Ground state tunneling dynamics. (a) Atoms were prepared in a single line along the y direction before the lattice along the x axis was lowered, allowing the atoms to tunnel in this direction [(b)-(d)]. The top row shows snapshots of the atomic distribution after different hold times. White circles indicate the lattice sites at which the atoms were prepared (not all sites initially contained an atom). The bottom row shows the respective position distribution obtained from an average over $10-20$ of such pictures, the error bars give the 1σ statistical uncertainty. A single fit to all distributions recorded at different hold times (red curve) yields a tunneling coupling of $J^{(0)}/\hbar = 940(20)$ Hz, a trap frequency of $\omega_{\mathrm{trap}}/(2\pi) = 103(4)$ Hz and a trap offset of $x_{\mathrm{offs}} = -6.3(6)\, a_{\mathrm{lat}}$.

lattice depths along all axes to $70\, E_r$. By averaging the resulting atomic distribution along the y direction and repeating the experiment several times, we obtained the probability distribution of finding an atom at the different lattice sites along the x direction (Fig. 7.1, bottom row).

This probability distribution samples the single-atom wave function after a coherent tunneling evolution. We observed how the wave function expands in the lattice and how the interference of different paths leads to distinct maxima and minima in the distribution, leaving for example almost no atoms at the initial position after a single tunneling time $\hbar/J^{(0)}$ [Fig. 7.1(c)]. This behavior differs markedly from the evolution in free space, where a Gaussian wave packet disperses without changing its shape, always preserving a maximum probability in the center. For longer hold times, an asymmetry in the spatial distribution becomes apparent [Fig. 7.1(d)], which originates from an offset between the bottom of the external harmonic confinement and the initial position of the atoms.

We describe the observed tunneling dynamics by a simple Hamiltonian including the tunnel coupling between two neighboring sites and an external harmonic con-

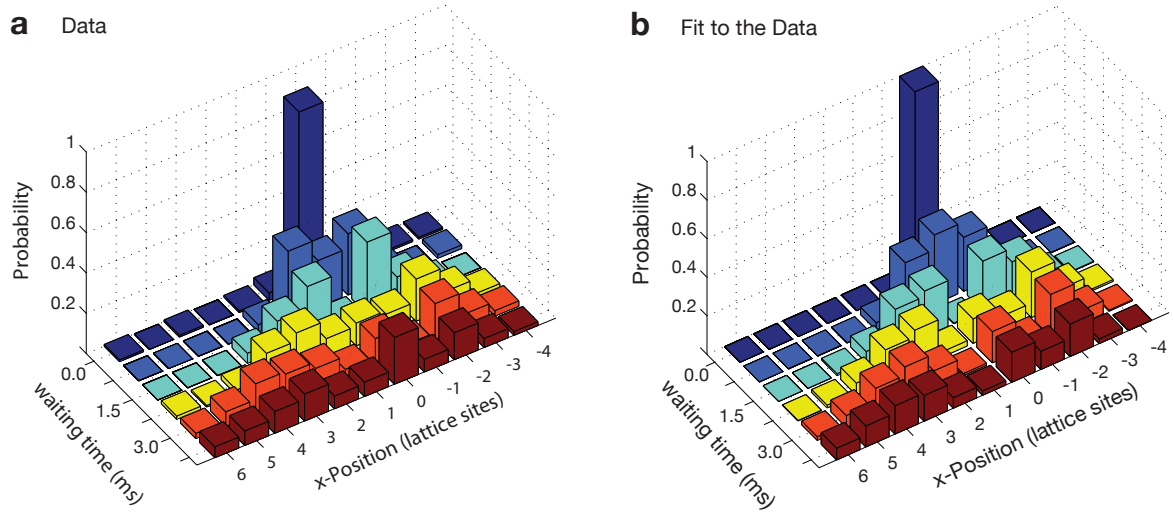

Figure 7.2: Ground state tunneling dynamics. Different representation of the data from Fig. 7.1. (a) Experimental position distribution. (b) Probability distribution as calculated for the fit parameters.

finement. The Hamiltonian on $k = 2n + 1$ lattice sites reads

$$\hat{H}^{(0)} = -J^{(0)} \sum_{i=-n}^{n} \left(\hat{a}_{i+1}^{\dagger} \hat{a}_i + \hat{a}_{i-1}^{\dagger} \hat{a}_i \right) + V_{\text{ext}} \sum_{i=-n}^{n} (i - x_{\text{offs}}/a_{\text{lat}})^2 \hat{a}_i^{\dagger} \hat{a}_i, \tag{7.1}$$

where $J^{(0)}$ is the tunnel coupling in the lowest band, and $\hat{a}_i^{\dagger}$ ($\hat{a}_i$) is the creation (annihilation) operator for a particle at site i. The strength of the external harmonic potential with trapping frequency ω_{trap} is given by $V_{\text{ext}} = \frac{1}{2} m \omega_{\text{trap}}^2 a_{\text{lat}}^2$, and x_{offs} describes a position offset with respect to the bottom of the harmonic potential. The single particle wave function and its coherent time evolution are given by

$$\Psi^{(0)}(t) = \sum_{i=-n}^{n} c_i^{(0)}(t) \hat{a}_i^{\dagger} |\tilde{0}\rangle = \exp\left(-i\hat{H}^{(0)} t/\hbar\right) \Psi^{(0)}(0), \tag{7.2}$$

with the initial condition $\Psi^{(0)}(0) = \hat{a}_0^{\dagger} |\tilde{0}\rangle$ and the vacuum state $|\tilde{0}\rangle$. The resulting probability of finding the particle at lattice site i after time t is $P_i^{(0)}(t) = |c_i^{(0)}(t)|^2$. For analyzing the data of Fig. 7.1, we calculated the time evolution for $k = 17$ lattice sites.

A single fit to all probability distributions recorded at different hold times (red line in Fig. 7.1) yields $J^{(0)}/\hbar = 940(20)\,\text{Hz}$, $\omega_{\text{trap}}/(2\pi) = 103(4)\,\text{Hz}$ and $x_{\text{offs}} = -6.3(6)\,a_{\text{lat}}$. This is in agreement with the trap frequency $\omega_{\text{trap}}/(2\pi) = 107(2)\,\text{Hz}$ obtained from an independent measurement via excitation of the dipole mode without the x lattice, whose contribution to the external confinement is negligible compared to the other two axes. From $J^{(0)}$, we calculated a lattice depth of $V_x = 4.6(1)\,E_r$,

which agrees with an independent calibration via parametric heating. Fig. 7.2 shows the same data as Fig. 7.1 in a different representation.

The expansion of the wave packet can also be understood by writing the initial localized wave function as a superposition of all Bloch waves of quasi-momentum $\hbar q$, with $-\pi/a_{\mathrm{lat}} \leq q \leq \pi/a_{\mathrm{lat}}$. To each quasi-momentum $\hbar q$, we can assign a velocity $v_q = \frac{1}{\hbar}\frac{\partial E}{\partial q}$, determined by the dispersion relation $E(q) = -2J^{(0)}\cos(qa_{\mathrm{lat}})$ of the lowest band. The edges of the wave packet propagate with the largest occurring velocity $v_{\mathrm{max}} = 2J^{(0)}a_{\mathrm{lat}}/\hbar = 1.88(4)\,a_{\mathrm{lat}}/\mathrm{ms}$, in agreement with our data.

We also observed how the dynamics is suppressed, when the tunneling from site to site is shifted out of resonance by the external confinement. In combination with the offset $x_{\mathrm{offs}} = -6.3(6)\,a_{\mathrm{lat}}$ between the bottom of the external confinement and the prepared initial atom position, the external confinement leads to a potential gradient at the atom position. As the external confinement is caused by the perpendicular lattice depths, we increased it by keeping the perpendicular lattice depths at $V_y = 56\,E_r$ and $V_z = 70\,E_r$. The trap frequency of the external confinement is then $\omega_{\mathrm{trap}}/(2\pi) = 250\,\mathrm{Hz}$ and the energy shift from the initial lattice site to the adjacent lattice sites is $\Delta E = m\omega_{\mathrm{trap}}^2 x_{\mathrm{offs}} a_{\mathrm{lat}} = h \cdot 900\,\mathrm{Hz}$. We found that in this case the atoms stay at the prepared position even after several hundred milliseconds.

7.3 Tunneling in the first excited band

In a second tunneling experiment, we observed the faster dynamics of atoms in the first excited band (see Fig. 7.3). For this, we deliberately excited the atoms by introducing a pointing offset δx of the addressing beam, which caused a shift of the potential wells during the switch-on. We repeated the same tunneling experiment as above with a hold time of $t = 1\,\mathrm{ms}$ for different pointing offsets δx. For a small pointing offset [$\delta x = 0.1\,a_{\mathrm{lat}}$ in Fig. 7.3(b)] we observed a narrow distribution, compared to a much broader one for a large offset [$\delta x = -0.4\,a_{\mathrm{lat}}$ in Fig. 7.3(a)]. We attribute this to different fractions f of atoms in the first band which is characterized by the higher tunneling rate $J^{(1)}$.

We fitted the distribution of Fig. 7.3(a) to a two-band model and found $J^{(1)}/\hbar = 6.22(6)\,\mathrm{kHz}$. This is in excellent agreement with the expected value of $J^{(1)}/\hbar = 6.14(6)\,\mathrm{kHz}$ from a band structure calculation in which we used $J^{(0)}$ as an input parameter to calculate the lattice depth.

When including tunneling in the first band, we assume an incoherent sum $P^{\mathrm{tot}}(t)$ of the distributions $P^{(0)}(t)$ of the zeroth band and $P^{(1)}(t)$ of the first band as

$$P^{\mathrm{tot}}(t) = (1-f)P^{(0)}(t) + fP^{(1)}(t). \tag{7.3}$$

The Hamiltonian $\hat{H}^{(1)}$ in the first band and the coherent dynamics are identical to the ones of the zeroth band (Eqs. 7.1 and 7.2), except for a different tunnel coupling

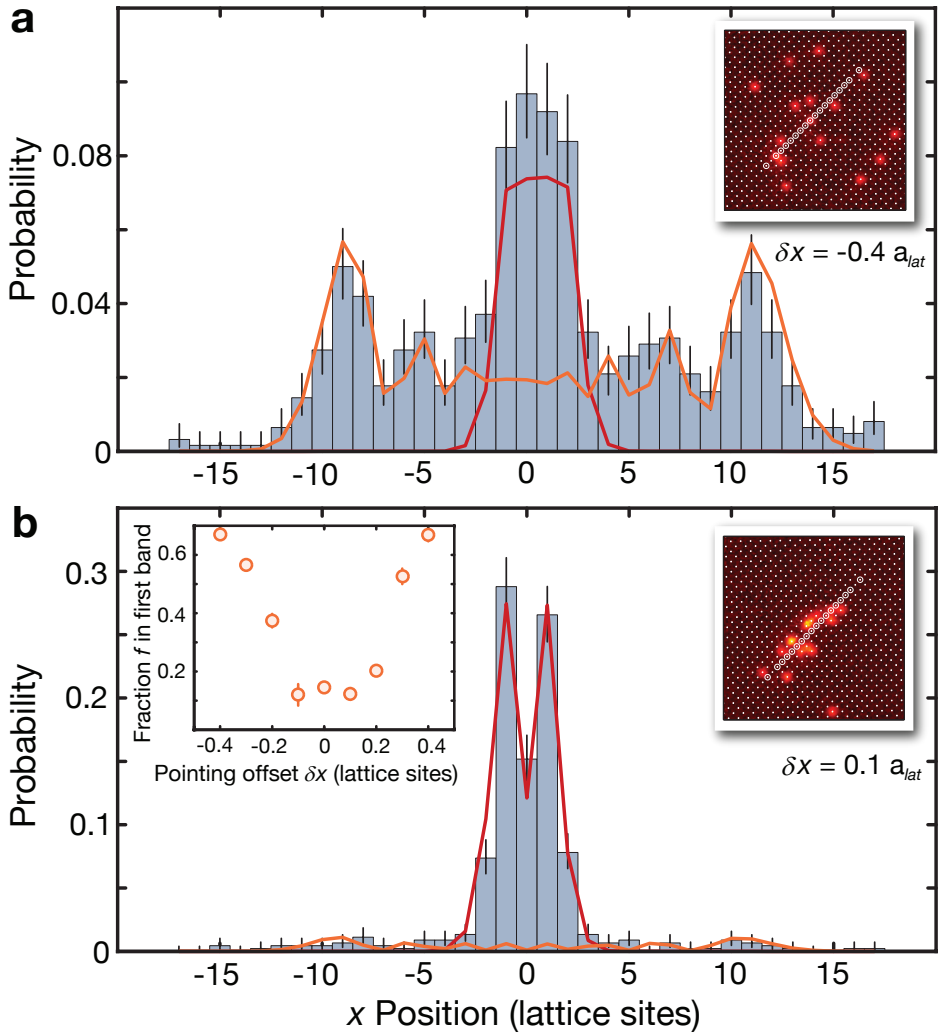

Figure 7.3: Tunneling dynamics of the first excited band. Some atoms were excited to the first band by a pointing offset δx of the addressing beam. (a) and (b) show the atomic position distribution after 1 ms tunneling time for $\delta x = -0.4\, a_{\mathrm{lat}}$ and $\delta x = 0.1\, a_{\mathrm{lat}}$, respectively. We fitted the data with a model that includes atoms in the zeroth band (red line) and a fraction f in the first band (orange line). The right insets to (a),(b) show corresponding original images. The left inset to (b) shows f versus δx with a broad minimum of $f = 13(2)\%$, indicating that most of the atoms are left in the ground state.

$J^{(1)}$. When fitting this model to our data, we kept ω_{trap}, x_{offs} and $J^{(0)}$ fixed at the values obtained from the data displayed in Fig. 7.1. We extracted $J^{(1)}$ from the data of Fig. 7.3(a) and used this value to fit the results for other pointing offsets.

For the data in Fig. 7.3, the parameters of our microwave sweep were such that also neighboring atoms were addressed. We took this into account by summing over two distinct probability distributions with a second starting position in the direction of the

pointing offset. Interaction effects between the two atoms in the 1D system are negligible for our parameters. From the lattice depths we calculate an interaction energy of $U_{\mathrm{int}} = h \cdot 610\,\mathrm{Hz}$ using a band structure calculation and the known atom-interaction parameters. This has to be compared to the kinetic energy of $4ZJ^{(0)}$ with the number of next neighbors $Z = 2$ in a one-dimensional system. For $U_{\mathrm{int}}/(8J^{(0)}) = 0.5$ and $U_{\mathrm{int}}/(8J^{(1)}) = 0.08$ we do not expect to observe interaction effects, e.g. repulsively bound pairs. The study of interaction effects is left for future investigations.

Our measurement of the fraction of excited atoms f as a function of the pointing offset δx [inset to Fig. 7.3(b)] shows that the atoms are strongly heated for large pointing offsets. By contrast, only a small fraction of the atoms is excited to the first band for small pointing offsets $|\delta x| \leq 0.1\, a_{\mathrm{lat}}$, yielding a ground state population of $1 - f = 87(2)\%$.

This value was not optimized yet. The heating is more than we would expect from spontaneous scattering of lattice photons even for the relatively long hold times of 800 ms. It might be due to a small amplitude shaking of the addressing beam position or intensity noise. Most probably it comes from a sideband transition of the microwave transfer, which is possible, because the differential light shift of the addressing beam leads to different trap frequencies for the two hyperfine states, which lifts the orthogonality of the vibrational levels.

7.4 Conclusion

We used our ability to prepare an arbitrary atom distribution for the study of coherent tunneling dynamics in a one-dimensional lattice. We started with a single line of atoms and lowered the perpendicular lattice depth for a varying hold time before we freezed and imaged the distribution. By averaging over the copies of the one-dimensional system and over several realizations we mapped out the wave function and its coherent evolution. We observe the distinct minima and maxima in the distribution originating from the interference of different paths.

We fitted the data to a simple model including the next neighbor tunnel coupling and an external confinement and found a tunneling rate in agreement with the expectation from a band structure calculation.

We excited atoms to higher bands by giving a pointing offset between the addressing laser and the lattice during the preparation of the starting position. We observed that the atoms tunnel much further in this case. We fitted to a model including the dynamics of the zeroth and the first band and extracted the tunneling rate of the first band as well as the fraction of atoms in the first band. We found that without pointing offset, our addressing scheme leaves $87(2)\%$ of the atoms in the vibrational ground state. The preparation of atoms in the ground state is important for the study of further non-equilibrium quantum dynamics.

Our measurements constitute the first observation of the ground state tunneling dynamics of massive particles on a lattice with single-site resolution.

8 Coherent light scattering from a 2D Mott insulator

In this chapter, we investigate coherent light scattering from an atomic Mott insulator in a two-dimensional square lattice structure [165]. We imaged the far-field diffraction pattern while simultaneously laser cooling the atoms with the probe beams and found distinct diffraction peaks.

The angular position of the diffraction peaks and the scaling of the peak parameters with the atom number are described by a simple analytic model (Sec. 8.2). A quantitative analysis of the diffraction pattern confirms the coherent nature of the scattering process (Sec. 8.3). From the power fraction in the peaks we deduce the coherence of the fluorescence light and discuss the mechanisms that reduce the coherence (Sec. 8.4).

We artificially prepared 1D antiferromagnetic order as a density wave and subsequently observed additional diffraction peaks, thus demonstrating the usability of light scattering for the detection of global spin correlations (Sec. 8.5).

8.1 State of the art

Recent interest in cold atoms research has focused on reaching sufficiently low temperatures and entropies to observe magnetically ordered quantum phases [3]. In this context, light scattering has been proposed as a new tool to detect these quantum correlations. Spin correlations could be mapped onto correlations of scattered light [166–169] or be detected via diffraction peaks from the additional scattering planes for spin-dependent probe light [170]. Light scattering would allow to measure the temperature of fermions in an optical lattice [171] or the density fluctuations across the superfluid-to-Mott-insulator transition [172–174]. Since the amount of scattered light is usually very small, several proposals involve a cavity for the detection [175, 176].

Without cavities, elastic Bragg scattering has been used to demonstrate the long range periodic order of thermal atoms in an optical lattice despite very low filling factors [177, 178]. It allowed the measurement of a change of the lattice constant from the backaction of the atoms [177, 179], their localization dynamics [180, 181] and temperature [179]. Bragg scattering was also studied in a far-detuned one-dimensional lattice [182].

8.2 Analytic 1D model

We begin by introducing a simple analytic 1D model to illustrate the underlying physics. Atoms on a 1D lattice (lattice spacing $a_{\mathrm{lat}} = \lambda_{\mathrm{lat}}/2$, where λ_{lat} is the lat-

tice wavelength) are driven by a light field (wavelength λ_{probe}) entering from the x direction [Fig. 8.1(a)] with wave vector $\mathbf{k}_i = k\,\mathbf{e}_x$, where $k = 2\pi/\lambda_{\text{probe}}$ and $\mathbf{e}_x$ is the unit vector along x. The scattered light is detected at a point $\mathbf{r}$, defined by the angle θ with the z-axis, such that $\mathbf{r} = r\,\mathbf{e}_r = r\sin\theta\,\mathbf{e}_x + r\cos\theta\,\mathbf{e}_z$. The position of the l-th atom is $\mathbf{x}_l = l\,a_{\text{lat}}\,\mathbf{e}_x$ and its distance r_l to the detection point is in far-field approximation $r_l = |\mathbf{r} - \mathbf{x}_l| \approx r - \mathbf{x}_l \cdot \mathbf{e}_r$. In our model, each atom emits a spherical wave, which at the detection point can be written as

$$F_l(r_l) = f\frac{e^{ikr_l}}{r_l}e^{i\delta_l} \approx f\frac{e^{ikr}}{r}e^{-i\mathbf{K}\cdot\mathbf{x}_l}. \tag{8.1}$$

Here, f denotes the coherently scattered field amplitude, $\delta_l = \mathbf{k}_i \cdot \mathbf{x}_l$ is the phase imprinted by the incoming light field, and $\mathbf{K} = \mathbf{k}_o - \mathbf{k}_i$ with the wave vector $\mathbf{k}_o = k\,\mathbf{e}_r$ in the observed direction. The differential cross section $\frac{d\sigma}{d\theta}(\mathbf{K}) \propto |\sum_l e^{-i\mathbf{K}\cdot\mathbf{x}_l}|^2$ is obtained by summing over the field amplitudes from all N_x atoms. As a result, we obtain the angular dependence of the scattered light field,

$$\frac{d\sigma}{d\theta}(\theta) \propto \frac{\sin^2\left[k\,a_{\text{lat}}(\sin\theta - 1)N_x/2\right]}{\sin^2\left[k\,a_{\text{lat}}(\sin\theta - 1)/2\right]}. \tag{8.2}$$

with distinct maxima when the field amplitudes of neighboring atoms interfere constructively, i.e. when $\mathbf{K}\cdot(\mathbf{x}_l - \mathbf{x}_{l+1}) = 2\pi\cdot n$, where n is an integer that denotes the diffraction order. The height of the diffraction peak is proportional to N_x^2 whereas the peak width scales as $1/N_x$. The angles θ_n, under which the diffraction maxima can be observed, are given by

$$\sin\theta_n = 1 + n\frac{\lambda}{a_{\text{lat}}}. \tag{8.3}$$

The trivial case $n = 0$ gives the forward scattered light ($\theta_0 = 90°$), independent of a_{lat} and λ. For our experimental parameters ($\lambda_{\text{probe}} = 780\,\text{nm}$, $a_{\text{lat}} = 532\,\text{nm}$), Eq. (8.3) can be additionally fulfilled only for $n = -1$, yielding the corresponding minus first diffraction order at $\theta_{-1} = -27.8°$ and $207.8°$. These two out of plane scattered waves ensure the momentum conservation in the z direction. Fig. 8.1(b) (blue curve) shows a polar plot of $\frac{d\sigma}{d\theta}(\theta)$, displaying the forward scattered light and the two diffraction peaks, one of which is captured by our imaging system (gray shaded region). If only every second lattice site is occupied (e.g. after removing one spin component in an antiferromagnetically ordered sample), the periodicity of the system is doubled. In this case, there are two possible diffraction orders (in the upper half plane) at $\theta_{-1}^{\text{AFM}} = 15.5°$ and $\theta_{-2}^{\text{AFM}} = \theta_{-1} = -27.8°$ [green curve in Fig. 8.1(b)].

It is straight-forward to extend this simple model to the two-dimensional case, if one assumes a rectangular instead of elliptical profile of the cloud. In this case, the two directions separate and one finds only the zeroth diffraction order in the direction perpendicular to the incoming beam.

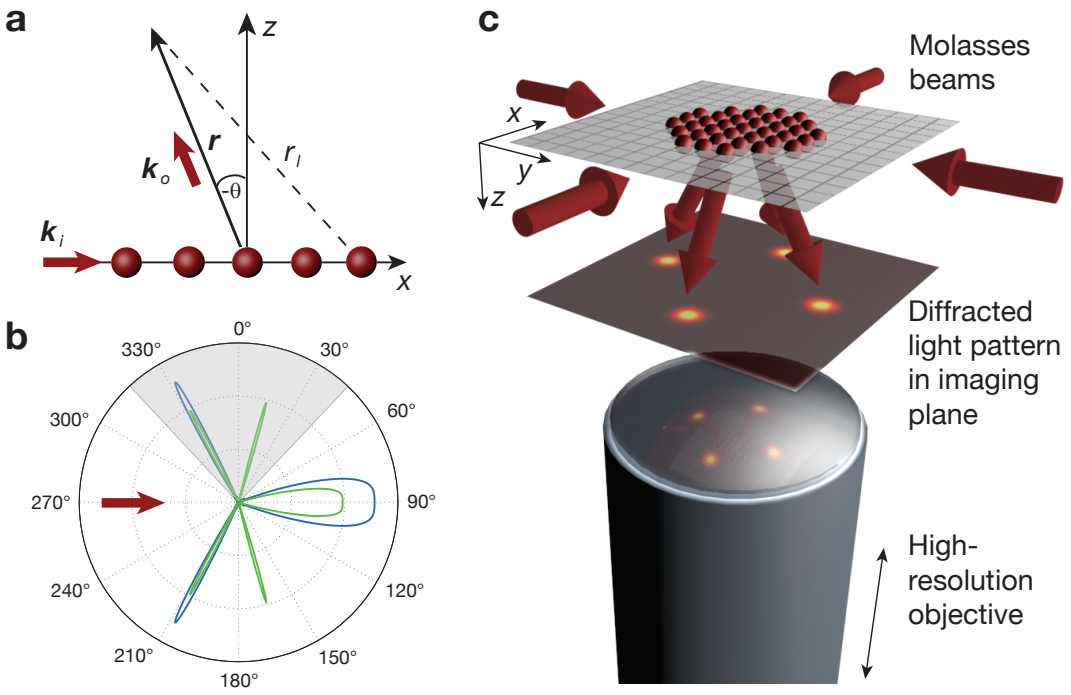

Figure 8.1: Schematics of light scattering from a Mott insulator. (a) Light diffraction from atoms in a 1D lattice. An incoming plane wave with wave vector $\mathbf{k}_i$ is diffracted under an angle θ. (b) Resulting differential scattering cross section $\frac{d\sigma}{d\theta}(\theta)$, as given by Eq. (8.2) for our experimental parameters. Shown are the cases for unity filling of the lattice and atom number $N = 16$ (blue curve) and for a z-Néel antiferromagnet along one direction ($N = 28$), from which only one spin component is detected (green curve). The grey shaded area indicates the opening angle of our imaging system. (c) Experimental setup. Atoms in a 2D optical lattice are illuminated with four in-plane molasses beams. *In situ* and far-field diffraction images are recorded with a high-resolution optical imaging system.

8.3 Far-field diffraction pattern

Imaging the far-field

The atoms are detected via fluorescence imaging using a high numerical aperture objective. The objective can be moved by 100 μm in the z direction within 50 ms using a piezo scanning device, thus shifting the focal plane by a distance Δz away from the atom position. The high numerical aperture corresponds to a half opening angle $\alpha = 43°$, which allows to measure a large angular range, when the objective is displaced to image the far-field. In particular, the diffraction peaks at θ_{-1} lie well within this range. However, the method does not rely on the high aperture of our imaging system, as the diffraction peaks could also be detected in a restricted angular range.

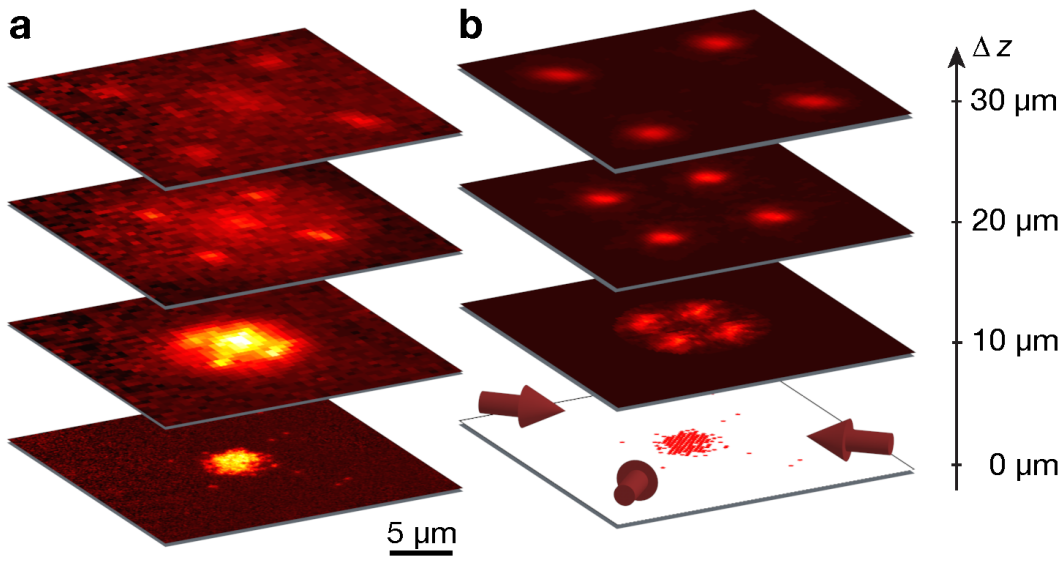

Figure 8.2: Light scattering from a 2D Mott insulator. (a) Experimental images from the same atomic sample for four different distances Δz of the focal plane with respect to the atom position. The bottom image shows the *in situ* atom number distribution, whereas the upper image shows the far-field diffraction pattern. (b) Simulated diffraction patterns obtained from a 2D numerical model (see text for details), using the reconstructed atom distribution (bottom image) from (a). Red arrows indicate the directions of the optical molasses beams.

Our experimentally obtained diffraction images are shown in Fig. 8.2(a) for four different distances Δz and an illumination time of 200 ms for each image. All four images are from the same sample. For $\Delta z = 0$ we observed the *in situ* atom number distribution, consisting in this case of 147 atoms in a Mott insulator shell with unit occupancy and diameter of 6 μm. For larger Δz, we observe the build up of the far-field distribution with distinct diffraction peaks.

Simulation of the far-field pattern

We compared the experimental data with a numerical calculation of $\frac{d\sigma}{d\theta}(\mathbf{K})$ using the actual atom distribution of the image at $\Delta z = 0$ [Fig. 8.2(b)]. For this purpose, we coherently summed over all spherical waves $F_l(r_l)$ emitted by the atoms with phases δ_l given by the incident driving fields. Our model assumes that all four horizontal molasses beams are diffracted independently. A spherical wave for the emission pattern is used, because the different local polarizations in the molasses result in all possible orientations of the atomic dipole. The average over all orientations of the dipole patterns, which the atoms emit, reproduces a spherical wave. The calculated far-field distribution is in good qualitative agreement with the experimental images.

The simulation in Fig. 8.2(b) only includes the coherently scattered light, whereas the experimental data in Fig. 8.2(a) also shows a significant incoherent background.

Evaluation of the diffraction peaks

For a more quantitative analysis, we recorded diffraction patterns of Mott insulators for different atom numbers [Fig. 8.3(a)-(c)]. We evaluated cuts (angular sectors of width 4 °) through the diffraction peaks and through the background signal [see Fig. 8.3(c)] and applied a coordinate transformation from the position x and y in the far-field plane to polar coordinates θ and ϕ. We determined the center of the cloud from the *in situ* image and transformed to polar coordinates in the far-field plane with the radial coordinate $r = \sqrt{x^2 + y^2}$ and the polar angle ϕ with the x axis. Then we transformed from the radius r to the angle θ with the z axis as $\tan(\theta) = r/\Delta z$, where Δz is the distance between the *in situ* plane and the far-field plane. The differential cross section is transformed as

$$\frac{\mathrm{d}\sigma}{\mathrm{d}\theta \mathrm{d}\phi} = \frac{\mathrm{d}\sigma}{\mathrm{d}x\mathrm{d}y} \det \frac{\partial(x,y)}{\partial(\theta,\phi)} = \frac{\mathrm{d}\sigma}{\mathrm{d}x\mathrm{d}y}(\Delta z + \frac{r^2}{\Delta z})\Delta z. \tag{8.4}$$

Fig. 8.3(d) shows the resulting angular distribution $\frac{\mathrm{d}\sigma}{\mathrm{d}\theta}(\theta)$ of the differential scattering cross section. We fitted the resulting peaks with a Gaussian (height A, $1/\sqrt{\mathrm{e}}$ width w, center position θ_{-1}, and offset fixed at the background value). The peak position, averaged over all experimental runs is $|\theta_{-1}| = 27.4(6)\,^\circ$, in excellent agreement with the expected value of $|\theta_{-1}| = 27.8\,^\circ$. The error is dominated by the systematic uncertainty of $\pm 1\,\mu$m in the determination of Δz. The systematic deviation of the diffraction angle might also be due to a small angle between the molasses beams and the lattice beams.

The peak height scales quadratically with the atom number [Fig. 8.3(e)], illustrating the coherent nature of the scattering. The peak width scales as $w \propto 1/\sqrt{N}$ [Fig. 8.3(f)], in agreement with the result from the 1D model [Eq. (8.2)], assuming $N_x = \sqrt{N}$ atoms in one dimension.

In addition to the four diffraction peaks from the horizontal molasses beams, a fifth weaker peak is clearly visible in the center left part of the far-field images [see white circle in Fig. 8.3(c)]. This peak results from the diffraction of the fifth molasses beam which is shone in from the direction of the imaging system. This shows that our single plane of a few hundred atoms in the optical lattice acts as a "mirror" for the incoming beam. In contrast to Bragg scattering from a 3D lattice, we expect reflection for any incidence angle, because there is only a single lattice plane.

Power fraction in the peaks

We used the far-field images to extract the power scattered into the detected diffraction peaks and the power scattered into the background. We know from Sec. 8.2 that

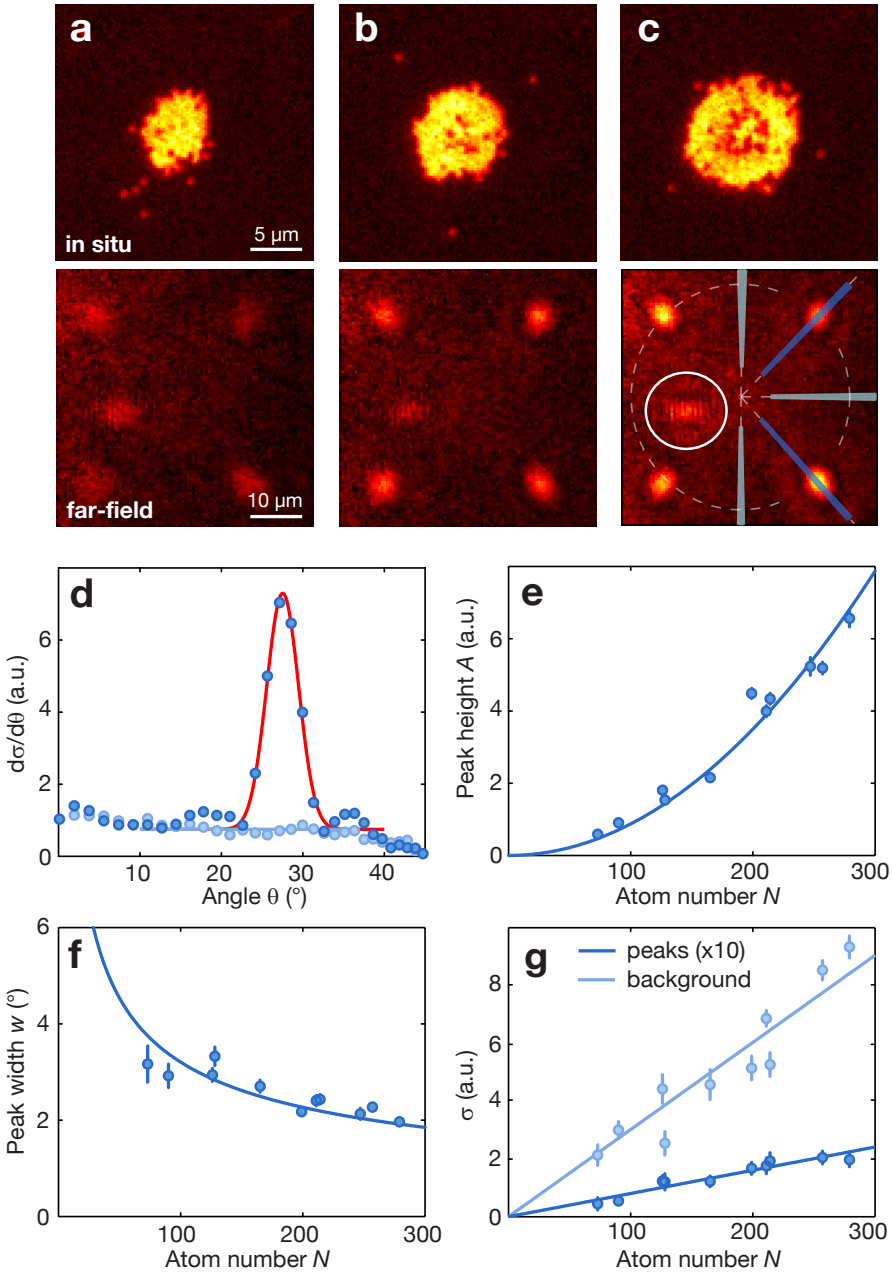

Figure 8.3: Analysis of the diffraction patterns. (a)-(c) *In situ* images ($N = 126$, 199 and 279 atoms) and the corresponding far-field diffraction patterns ($\Delta z = 40\,\mu$m) from the same experimental run, with an illumination time of 500 ms each. The white circle in (c) marks the diffraction peak from the fifth molasses beam, which is shone in from below. (d) Angular distribution of the differential scattering cross section obtained from cuts in (c) through the diffraction peaks (dark blue) and the background signal (light blue). The peak is fitted with a Gaussian (red line). (e) Peak height A versus atom number N together with a quadratic fit. (f) Peak width w versus atom number N, with a fit to $w \propto 1/\sqrt{N}$. (g) Total background signal σ_b (light blue) as obtained from the constant background in (d) and total signal in the peaks σ_p (dark blue, scaled by a factor of 10 for better visibility) obtained from the fits to the diffraction peaks (see text).

there are three peaks per beam one of which is detected. We exclude here the forward scattering light and consider the power in the detected peak and its symmetric counterpart in the other direction.

In the cuts outside the diffraction peaks [see light blue data in Fig. 8.3(d)], we found a constant background differential cross section $(\frac{\mathrm{d}\sigma}{\mathrm{d}\theta})_b$ and calculated the total incoherent scattering cross section $\sigma_b = 4\pi(\frac{\mathrm{d}\sigma}{\mathrm{d}\theta})_b$, assuming an isotropic intensity distribution. In the data, the background actually drops to zero for angles larger than the half opening angle 43° of our imaging system. We also corrected for a global offset, that was due to imperfect stray light substraction.

The total scattering cross section of one peak is given by an integral over the full solid angle

$$\sigma_p^{(1)} = \int\int \frac{\mathrm{d}\sigma}{\mathrm{d}\theta\mathrm{d}\phi}(\theta,\phi)\sin(\theta)\mathrm{d}\theta\mathrm{d}\phi, \tag{8.5}$$

where the differential scattering cross section $\frac{\mathrm{d}\sigma}{\mathrm{d}\theta\mathrm{d}\phi}(\theta,\phi)$ is a peaked function, which we can approximate by a Gaussian with height A, width w in the radial direction and $w\cos(\theta_{-1})$ in the azimuthal direction. The factor $\cos(\theta_{-1})$ accounts for the ellipticity of the diffraction peaks due to the effective ellipticity of the atomic cloud, when viewed under the angle θ_{-1}. We obtain these parameters from a Gaussian fit to a cut through the peak [see dark blue data and red line in Fig. 8.3(d)].

Because the peak covers only a small range of θ, we can evaluate the factor $\sin(\theta)$ at the position of the peak and pull it out of the integral. We then obtain for the total scattering cross section of one peak

$$\sigma_p^{(1)} \approx \sin(\theta_{-1})2\pi A w^2 \cos(\theta_{-1}). \tag{8.6}$$

As there are five molasses beams and a symmetric counterpart in the other direction for each detected peak, the total scattering cross section in the peaks (excluding the forward scattered light) is $\sigma_p = 10 \cdot \sigma_p^{(1)}$.

Fig. 8.3(g) shows σ_b and σ_p, which both scale linearly with the number of atoms. From the slopes, we find a fraction $f_p = \sigma_p/(\sigma_b + \sigma_p) \approx 3\%$ of the power scattered into the detected peaks.

8.4 Coherence of the fluorescence light

In Sec. 8.3 we compared the power in the detected diffraction peaks to that in the constant background and found a fraction of $f_\mathrm{p} = 3\%$ in the peaks. Here we discuss the various mechanisms that lead to this reduced interference and to the background signal outside the diffraction peaks. We find that the localization of the atoms, the atomic distribution, and the coherence and elasticity of the scattering process play a role.

Forward scattered light

We only detect the peaks of the minus first diffraction order, while the coherently forward scattered light (zeroth diffraction order) is not detected. Therefore we measure a reduced coherent fraction. We evaluate the fraction f_{-1} of the coherent light that is scattered into the minus first diffraction order by using the calculated far-field patterns (see Sec. 8.3) and integrating the power over two angular ranges ($\theta \in [-90°, -45°] \cup [45°, 90°]$ for the zeroth order and $\theta \in [-45°, 45°]$ for the minus first order). The fraction f_{-1} does depend on the atom number, but has a weak dependence in the relevant range and we can use $f_{-1} = 20\%$.

Debye-Waller factor

It is well known from x-ray diffraction from crystals, that the degree of localization of the scatterers changes the strength of the signal (see e.g. [183]). If the atoms are localized to a size Δr and the momentum transfer is $\mathbf{K}$, the Debye-Waller factor

$$\beta^2 = (\overline{e^{i\mathbf{K}\cdot\mathbf{r}}})^2 = \exp(-K^2\Delta r^2) \tag{8.7}$$

describes the reduction of the height of the diffraction peak compared to point sources fixed at their lattice site. Because the peak width is independent of the localization, the power in the peak is reduced by this factor and the missing power goes into an isotropic background. In our case, the momentum transfer for scattering into the minus first diffraction order θ_{-1} is given by

$$|\mathbf{K}| = |\mathbf{k}_o - \mathbf{k}_i| = k\sqrt{2\lambda/a_{\mathrm{lat}}} = 1.713\,k. \tag{8.8}$$

The localization at a temperature of $T \approx 22\,\mu$K and a lattice depth of $V_0 \sim k_B \cdot 200\,\mu$K is $\Delta r = 1/k_{\mathrm{lat}}\sqrt{(k_B T)/(2V_0)} \approx \lambda_{\mathrm{lat}}/27 \approx \lambda_{\mathrm{probe}}/20$. The Debye-Waller factor is then evaluated to be $\beta^2 = 0.75$. This is a typical value for diffraction from cold atoms, $\beta^2 = 0.2$ [177] and $\beta^2 = 0.76$ [178] have been reported for near-resonant 3D optical lattices and $\beta^2 = 0.64$ [182] for a far off-resonant 1D lattice. In these experiments, the exponential dependence of the Debye-Waller factor on the momentum transfer $\mathbf{K}$ has been used to directly measure the localization of the atoms by the comparison of two diffraction peaks with different momentum transfer [179].

Density fluctuations

Another mechanism, which reduces the power in the diffraction peaks, is the deviation from unity occupation of the lattice sites caused by density fluctuations in the system. This is quite intuitive, as the width of the diffraction peaks is given by the number of irradiated sites, independent of the degree of occupancy, whereas the peak height scales as the square of the contributing atoms. Distributing the same number

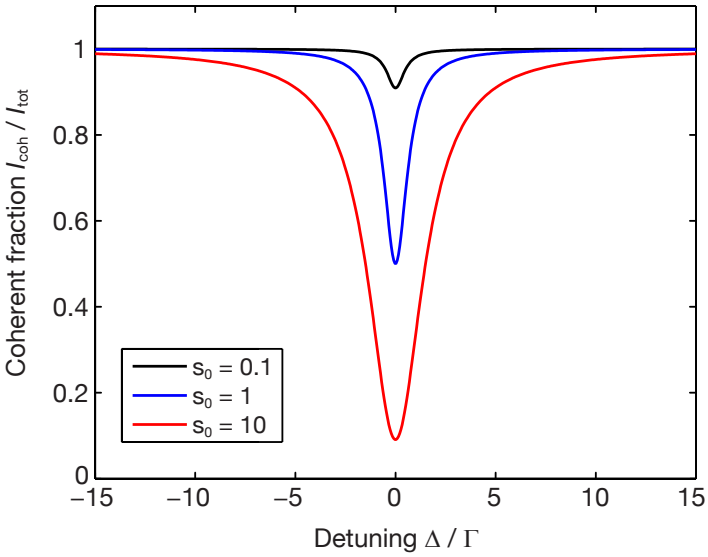

Figure 8.4: Coherent fraction in the fluorescence light of a two level system as given by Eq. (8.9) for three different saturation parameters.

of atoms over a larger region of the lattice will therefore lead to narrower peaks with the same peak height, i.e. less power in these peaks. In the case where the other mechanisms are weak, the power scattered into the background can be used as a sensitive tool for measuring the density fluctuations [172].

In order to quantify this mechanism for our system, we compared the calculated diffraction pattern from the actual atom distribution with that from a perfectly filled Mott insulator shell of the same atom number. We found that the power in the diffraction peaks is reduced by 30% due to the deviations from unity filling, which is caused by the finite temperature of the Mott insulators.

Coherence of the scattering process

During the light scattering, the atoms are continuously driven by a classical field. In a classical description via the Lorentz model, the atomic dipole oscillates with a fixed phase relation to the driving field, and emits a dipole pattern. In a quantum mechanical description, the situation changes, because spontaneous emission comes into play. Mollow calculates the coherently scattered intensity fraction of a continuously driven two-level system in equilibrium as [184]

$$\frac{I_{\text{coh}}}{I_{\text{tot}}} = \frac{\Delta^2 + (\Gamma/2)^2}{\Delta^2 + (s_0 + 1)(\Gamma/2)^2}. \tag{8.9}$$

Fig. 8.4 shows the coherent fraction for different detunings Δ (in units of the line width Γ) and saturation parameters s_0. The coherent fraction approaches unity for

Effect	Reduction factor
Forward scattering not detected	20%
Debye-Waller factor β^2	75%
Density fluctuations	70%
Coherence of scattering	99%
Inelasticity (change vibrational level)	98%
Inelasticity (change m_F level)	33%
Expected power in detected peaks	3%
Measured power in detected peaks	3%

Table 8.1: Reduction of the power scattered into the detected peaks. The table lists the different effects that lead to a reduction of the power in the peaks together with the reduction factor. The measured reduction agrees well with the expectations, as deduced from multiplying the reduction factor of all effects. For a discussion of the effects see the main text.

small saturation parameters and for large detunings and is above 99% for our parameters ($s_0 \approx 3, \Delta \approx 14\,\Gamma$). From this two-level point of view, the scattering should be almost completely coherent.

Inelastic scattering processes

Another source of incoherence is the inelasticity of the scattering process, which can change both the vibrational state of the atom and its magnetic sublevel. On average, each scattered photon leads to the transfer of two times the recoil energy $E_{\mathrm{rec}}^{\mathrm{probe}} = (\hbar k_{\mathrm{probe}})^2/(2m) = h \cdot 3.9\,\mathrm{kHz}$ to the atom. When the atom is confined in a trap, it cannot absorb this energy, but only multiples of the vibrational energy $h\nu_{\mathrm{trap}}$, where $\nu_{\mathrm{trap}} \approx 200\,\mathrm{kHz}$ is the trapping frequency. The Lamb-Dicke parameter $\eta = \sqrt{E_{\mathrm{rec}}^{\mathrm{probe}}/(h\nu_{\mathrm{trap}})}$ quantifies the ratio of these two energy scales. In the Lamb-Dicke regime $\eta \ll 1$, where the trap frequency is much larger than the recoil energy, the probability for a scattering process to change the vibrational state is given by η^2, which in our case is just $\eta^2 = 0.02$. Therefore most of the scattering events are elastic with respect to the vibrational state, even though the argument is weakened for atoms in higher vibrational states.

The scattering can also change the magnetic sublevel of the atom, emitting photons of different polarization, which do not interfere. Because for most m_F states there are three decay channels, one can assume in a rough estimate that one third of the scattering events preserves the magnetic sublevel. This dominant mechanism could be circumvented by using a single circular polarized beam, which drives a closed transition. However, using a molasses, which simultaneously cools the atoms, will still yield the overall largest signal.

Summary of the effects

Tab. 8.1 sums up all the different contributions discussed above. Multiplying the reduction factors of all effects, we find that the measured fraction in the detected peaks agrees well with the expectations. We can only compare the orders of magnitude, because the expected power in the peaks is the product of six different effects and can only be considered as an estimate. The dominant contribution to the incoherent background is inelastic scattering, which changes the magnetic sublevels of the atoms.

We verified our method of extracting the fraction of power scattered into the peaks [Eq. (8.6)], by running the same analysis as in Sec. 8.3 over simulated data as calculated in Sec. 8.3. When we include a coherent fraction in the simulation, we find about the same coherent fraction from the analysis when taking into account the relevant effects discussed above.

8.5 Detecting antiferromagnetic order in the density

Finally, we demonstrated that light scattering can be used for the detection of spin correlations. As an example, we created a 1D z-Néel antiferromagnetic order along the x direction of the lattice using our single-site addressing technique described in Ch. 6. We sequentially flipped all atomic spins in every second row of the lattice from $F = 1$ to $F = 2$ before we applied a resonant laser that removed all atoms in $F = 2$. Figs. 8.5(a) and (b) show the resulting fluorescence image in the focal plane together with the reconstructed atom number distribution. The corresponding experimental and theoretical diffraction patterns are displayed in Figs. 8.5(c) and (d). The two predicted diffraction peaks of -1$^{\text{st}}$ and -2$^{\text{nd}}$ order along x are clearly visible in the experimental picture, although our atomic sample consisted of only 57 atoms. We obtain the usual peak position of $|\theta^y_{-1}| = 27.7(6)^\circ$ along the y direction, whereas the two peaks along x are found at $|\theta^x_{-1}| = 14.5(6)^\circ$ and $|\theta^x_{-2}| = 27.4(6)^\circ$ [see Fig. 8.5(e),(f)], in good agreement with the expected values.

We prepared a 1D antiferromagnetic order, because the additional diffraction peaks that would arise for a 2D antiferromagnetic order lie outside the opening angle of our imaging system. However, the position of the diffraction peaks could be varied in a 2D geometry by changing the incidence angle of the molasses beams. For an in-plane angle between the lattice and the molasses beams of $\alpha = 15^\circ$, the additional peaks are shifted to smaller angles θ (see Fig. 8.6). An alternative is to use shorter wavelength probe light, e.g. near-resonant with the $5S - 6P$ transition at 420 nm for ^{87}Rb [178].

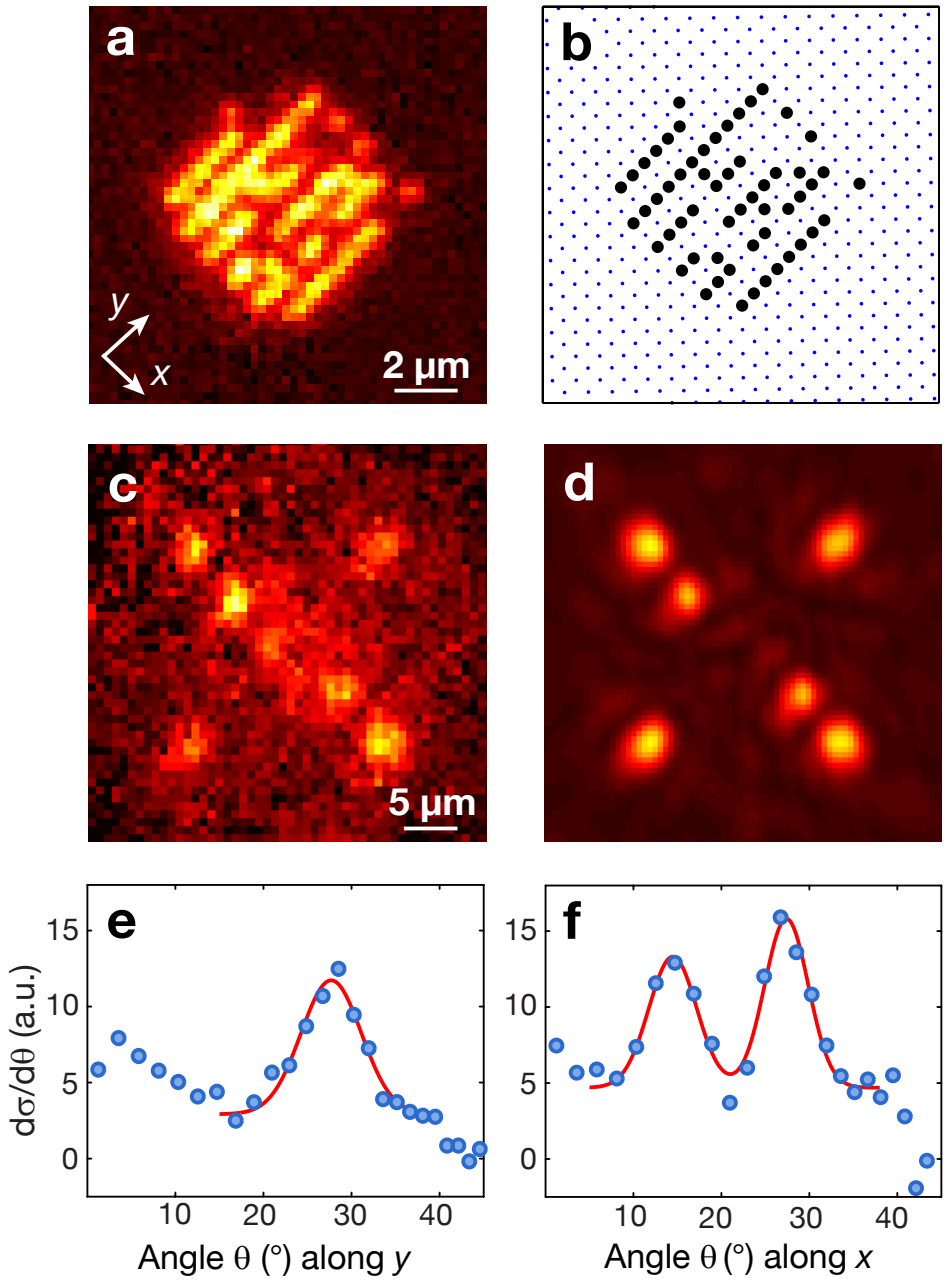

Figure 8.5: Light scattering for a 1D antiferromagnetic order in the density. (a) The atoms in every second row of the optical lattice were removed. (b) Reconstructed atom number distribution from (a). (c) Resulting far-field image ($\Delta z = 25\mu$m) with two diffraction orders in the x direction. (d) Simulated diffraction pattern using the atom number distribution of (b). (e),(f) Angular distribution of the differential scattering cross section obtained from cuts along the x and y directions together with Gaussian fits.

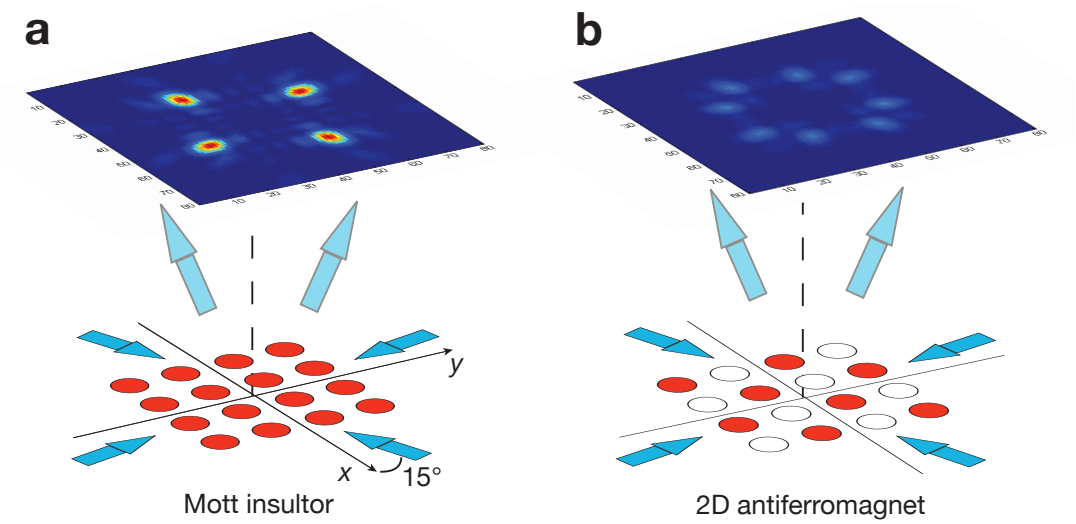

Figure 8.6: Simulation of light scattering for a 2D antiferromagnetic order in the density. The molasses beams have an in-plane angle of $\alpha = 15°$ with respect to the lattice axis, which changes the diffraction pattern. (a) For a Mott insulator with unity filling, there is a single diffraction peak for every molasses beam (b) For a checker-board occupation (2D antiferromagnetic order), there appear additional peaks at a convenient angle.

8.6 Conclusion and outlook

In this chapter, we have demonstrated coherent light scattering from a two-dimensional atomic Mott insulator, which shows distinct peaks in the far-field diffraction pattern. We quantitatively analyzed these peaks and studied the scaling of the peak height and width with the atom number. We found that 3% of the power is scattered into the detected peaks and discuss the different mechanisms, which lead to this reduced interference. These include the density fluctuations in the atom distribution, the finite localization of the atoms in their potential wells, and the inelastic scattering events which change the magnetic sublevels of the atoms.

Moreover, we prepared a one-dimensional antiferromagnetic order in the density and observed additional diffraction peaks, thus demonstrating the feasibility of detecting global spin correlations via light scattering.

Our results could be extended to the study of various density [172–174] or spin [167, 168, 170] correlations in optical lattices. Most proposals suggest weak non-destructive probing, which restricts the signal to only a few photons per atom. In our alternative approach, we projected the correlations onto the density before the detection by means of an optical molasses, which yields a signal of thousands of photons per atom. This is possible for density correlations, e.g. the number squeezing in a Mott insulator can be mapped on the mean density by parity projection [46, 47].

For spin correlations, we have demonstrated the feasibility of removing one spin state and observing the additional diffraction peaks from the density structure. This avoids spin selective coupling of the probe light to the atoms [170], which is incompatible with simultaneous laser cooling.

In the 3D case, antiferromagnetic order allows scattering from an additional plane, but it requires careful alignment of the probe beam angle to match the Bragg condition. In contrast, light scattering from a 2D system yields additional peaks from the same incident beam, which is also convenient for the extraction of the spin correlation length from the relative height or width of the diffraction peaks.

Finally, we note that the detection of spin correlations via light scattering does not rely on the high aperture of our imaging system. The diffraction peaks could also be detected in a restricted angular range.

9 Conclusion and outlook

This thesis presents novel experimental methods for the study of ultracold atoms in optical lattices. While most experiments so far probed the atoms globally, we have developed single-site resolved imaging and manipulation of single atoms in the strongly correlated regime.

We used a high numerical aperture imaging system to resolve single lattice sites. Fluorescence imaging allowed to detect single atoms with a large signal and to reconstruct the atom distribution on the lattice. With this technique we can study strongly correlated states at the single particle level. This is complementary to many existing methods like time-of-flight imaging, because it allows to probe the density correlations instead of the coherences.

We applied the technique to Mott insulators in the atomic limit and directly observed number squeezing and the shell structure. We determined the temperature in a single image by fitting the radial density profiles with a simple grand-canonical model. Our pictures show with unprecendented clarity that the entropy is concentrated in the transition regions between the Mott insulator shells and that it is essentially zero in the center of the shells. For our parameters, we calculated an entropy per particle which is around the critical entropy for quantum magnetism.

Moreover, we were able to address single atoms in the lattice and to manipulate their spin. We used the differential light shift of a tightly focused laser beam to shift selected atoms into resonance with a microwave driving the spin flip. This allowed us to reach a high spin-flip fidelity and sub-diffraction-limited resolution. Starting from a Mott insulator with unity filling, we we able to prepare arbitrary spin patterns of individual atoms, thus realizing a scalable single-atom source.

This ability to locally manipulate a strongly correlated atomic gas and to prepare arbitrary atom distributions opens many perspectives in quantum simulation and computation. As an example, we studied the single particle tunneling dynamics in a lattice and directly mapped out the wave function after coherent evolution. We discriminated the dynamics of atoms in the ground state and in the first excited band and found that our addressing scheme leaves most atoms in the ground state. The preparation of atoms in the ground state is important for the study of further non-equilibrium quantum dynamics.

Finally, we investigated coherent light scattering as an alternative method to detect antiferromagnetic order also when single-site resolution is not available. We imaged the far-field diffraction pattern while simultaneously laser cooling the atoms with the probe beams and found distinct peaks. We quantitatively analyzed the diffraction pattern and found the expected scalings of the peak parameters with the atom

number. From the power fraction in the peaks we deduced the coherence of the fluorescence light and we discuss the mechanisms that reduce the coherence. We artificially prepared 1D antiferromagnetic order as a density wave and observed additional diffraction peaks, thus demonstrating the usability of light scattering for the detection of global spin correlations.

The following paragraphs will give an outlook on some of the possible future applications of the techniques demonstrated in this thesis.

Even without local manipulation, imaging of single particles in the strongly correlated regime is a major step forward. This is valuable in a system with an external confinement, where one can have different phases at different positions in the trap, as in the prominent example of the shell structure of a Mott insulator. The measurement of the number statistics can be extended to the phase transition [46] and also to one-dimensional systems. A measurement of the density-density correlations [185] should reveal the coherent particle-hole excitations, when switching on tunneling coming from the insulating state. While thermal excitations are uncorrelated, these coherent excitations are expected to have long-range correlations. Furthermore one could observe the dynamics after a sudden quench from the Mott insulator to the superfluid regime [186] or from 1D to 2D. Also higher-order correlators that are inaccessible in condensed matter experiments can be tackled. For future work it would be interesting to investigate how entropy propagates in strongly correlated systems, after injecting it on a local scale into the system.

The entropies of our Mott insulators should be sufficiently low to observe quantum magnetism in a two-component system with unity total density [29, 119]. We plan to separate two spin states with a magnetic gradient and observe the mixing dynamics after switching off the gradient, which is mediated by second order hopping processes.

We can also investigate one-dimensional systems, which are particularly interesting due to the enhanced role of quantum fluctuations and the accessibility to numerical simulation also of the dynamics. At strong interactions, in the Tonks-Girardeau regime, the bosonic atoms are fermionized, and it would be interesting to detect the fermionized density-density correlations or Friedel oscillations [187–189].

The coherent manipulation of single spins in a Mott insulator opens the path for many new experiments. It will e.g. allow us to create out-of-equilibrium states or local perturbations in order to observe the ensuing dynamics of the many-body system, such as spin-charge separation [190, 191] or spin impurity dynamics beyond the Luttinger liquid theory [192]. Our studies of the tunnelling dynamics at the single-atom level can be extended to correlated particle tunneling [98, 160, 193], also in higher dimensions, or to observe transport across local impurities [194] or potential barriers. Further prospects are the implementation of novel cooling schemes relying on the local removal of regions with high entropy [7, 195].

Atoms in a Mott insulating state with one atom per lattice site are also very promis-

ing as a quantum register for scalable quantum computing, especially with the very low defect density shown in this work. Combining single-qubit manipulation with local readout and a global entanglement operation in a spin-dependent lattice [53, 54] would be the basis of a one-way quantum computer [51, 52]. For the circuit model of a quantum computer, two-qubit operations can be realized by Rydberg gates, which where already demonstrated in single dipole traps [56, 57]. Implementing them in an optical lattice will put tens of atoms within the blockade radius, thus allowing gates between selected atom pairs in the lattice without any atom movement.

A Rydberg laser system is currently being set up and will also be used to study condensed matter physics. E.g., one can generate long-range interactions between the atoms by weakly admixing excited Rydberg states with laser light [196]. Our high-resolution imaging would also allow to directly observe the blockade radius in the adiabatic formation of Rydberg crystals [197].

Finally, combining the high resolution imaging system with a spatial light modulator [37, 198–200] allows to project arbitrary potential shapes with small structure size, e.g. box potentials, arbitrary lattice geometries [45, 201] or controlled disorder [21, 202]. Using a wavelength with a differential light shift, one can also flip the spin of many selected atoms simultaneously and use this for selective entropy removal [7].

Danksagung

Hiermit möchte ich mich bei allen herzlich bedanken, die zum Gelingen dieser Arbeit beigetragen haben. Mein ganz besonderer Dank gilt dabei

Meinen Betreuern Prof. Immanuel Bloch und Prof. Stefan Kuhr, die mir die Möglichkeit gegeben haben an diesem spannenden Projekt zu arbeiten, für ihre Begeisterungsfähigkeit und tatkräftige Unterstützung. Sie waren stets ansprechbar und offen für Diskussionen und von ihrer dynamischen und motivierenden Anleitung habe ich sehr profitiert.

Meinen Laborkollegen Dr. Jacob Sherson, Manuel Endres und Dr. Marc Cheneau, mit denen zusammen ich dieses ehrgeizige Experiment aufbauen durfte, für die gute Zusammenarbeit und die erhellenden Diskussionen.

Dr. Takeshi Fukuhara, Peter Schauß und Dr. Christian Gross, die im letzten Jahr dazu gestoßen sind und von Anfang an im Labor eine große Hilfe waren.

Prof. Wolfgang Ketterle, der sein Sabbatical am MPQ verbracht hat und unser Labor mit wertvollen Ideen und inspirierenden Diskussionen bereichert hat.

Unseren Diplomanden, die im Laufe der vier Jahre am Experiment beteiligt waren: Oliver Loesdau, Jan Petersen, Rosa Glöckner, Ralf Labouvie, David Bellem und Ahmed Omran.

Allen weiteren Mitgliedern der Arbeitsgruppe für die guten Diskussionen und die stetige Hilfsbereitschaft.

Allen nicht wissenschaftlichen Mitarbeitern, die das Team engagiert unterstützt haben: Christine Best, Marianne Kargl, Heinz Lenk, Karsten Förster, Markus Böhm und Michael Pruscha.

Meinen Eltern und Geschwistern.

Es war eine besondere Erfahrung, in einem so motivierten Team zu arbeiten und ich bin gespannt auf die Experimente, die noch folgen werden.

Bibliography

[1] D. Jaksch, C. Bruder, J. I. Cirac, C. Gardiner, and P. Zoller. *Cold bosonic atoms in optical lattices*. Phys. Rev. Lett. **81**, 3108–3111 (1998).

[2] M. Greiner, O. Mandel, T. Esslinger, T. W. Hänsch, and I. Bloch. *Quantum phase transition from a superfluid to a Mott insulator in a gas of ultracold atoms*. Nature **415**, 39–44 (2002).

[3] M. Lewenstein, A. Sanpera, V. Ahufinger, B. Damski, A. Sen, and U. Sen. *Ultracold atomic gases in optical lattices: mimicking condensed matter physics and beyond*. Adv. Phys. **56**, 243–379 (2007).

[4] I. Bloch, J. Dalibard, and W. Zwerger. *Many-body physics with ultracold gases*. Rev. Mod. Phys. **80**, 885–964 (2008).

[5] R. P. Feynman. *Simulating physics with computers*. Intern. J. Theor. Phys. **21**, 467–488 (1982).

[6] C. Chin, R. Grimm, P. Julienne, and E. Tiesinga. *Feshbach resonances in ultracold gases*. Rev. Mod. Phys. **82**, 1225–1286 (2010).

[7] J.-S. Bernier, C. Kollath, A. Georges, L. De Leo, F. Gerbier, C. Salomon, and M. Köhl. *Cooling fermionic atoms in optical lattices by shaping the confinement*. Phys. Rev. A **79**, 061601(R) (2009).

[8] D. C. McKay and B. DeMarco. *Cooling in strongly correlated optical lattices : prospects and challenges*. Rep. Prog. Phys. **74**, 054401 (2011).

[9] B. DeMarco and D. S. Jin. *Onset of Fermi degeneracy in a trapped atomic gas*. Science **285**, 1703–1706 (1999).

[10] U. Schneider, L. Hackermüller, S. Will, I. Bloch, T. Best, T. Costi, R. Helmes, D. Rasch, and A. Rosch. *Metallic and insulating phases of repulsively interacting Fermions in a 3D optical lattice*. Science **322**, 1520–1525 (2008).

[11] R. Jördens, N. Strohmaier, K. Günter, H. Moritz, and T. Esslinger. *A Mott insulator of fermionic atoms in an optical lattice*. Nature **455**, 204–207 (2008).

[12] B. Paredes, A. Widera, V. Murg, O. Mandel, S. Fölling, J. I. Cirac, G. V. Shlyapnikov, T. Hänsch, and I. Bloch. *Tonks-Girardeau gas of ultracold atoms in an optical lattice*. Nature **429**, 277–281 (2004).

[13] T. Kinoshita, T. Wenger, and D. S. Weiss. *Observation of a one-dimensional Tonks-Girardeau gas*. Science **305**, 1125–1128 (2004).

[14] Z. Hadzibabic, P. Krüger, M. Cheneau, B. Battelier, and J. Dalibard. *Berezinskii-Kosterlitz-Thouless crossover in a trapped atomic gas*. Nature **441**, 1118–1121 (2006).

[15] J. G. Danzl, E. Haller, M. Gustavsson, M. J. Mark, R. Hart, N. Bouloufa, O. Dulieu, H. Ritsch, and H.-C. Nägerl. *Quantum gas of deeply bound ground state molecules*. Science **321**, 1062–1066 (2008).

[16] K.-K. Ni, S. Ospelkaus, M. H. G. de Miranda, A. Pe'er, B. Neyenhuis, J. J. Zirbel, S. Kotochigova, P. S. Julienne, D. S. Jin, and J. Ye. *A high phase-space-density gas of polar molecules*. Science **322**, 231–235 (2008).

[17] J. Billy, V. Josse, Z. Zuo, A. Bernard, B. Hambrecht, P. Lugan, D. Clément, L. Sanchez-Palencia, P. Bouyer, and A. Aspect. *Direct observation of Anderson localization of matter waves in a controlled disorder*. Nature **453**, 891–894 (2008).

[18] V. Gurarie, L. Pollet, N. V. Prokofev, B. V. Svistunov, and M. Troyer. *Phase diagram of the disordered Bose-Hubbard model*. Phys. Rev. B **80**, 214519 (2009).

[19] U. Bissbort and W. Hofstetter. *Stochastic mean-field theory for the disordered Bose-Hubbard model*. Europhys. Lett. **86**, 50007 (2009).

[20] L. Sanchez-Palencia and M. Lewenstein. *Disordered quantum gases under control*. Nature Phys. **6**, 87–95 (2010).

[21] M. Pasienski, D. McKay, M. White, and B. DeMarco. *A disordered insulator in an optical lattice*. Nature Phys. **6**, 677–680 (2010).

[22] M. R. Matthews, B. P. Anderson, P. C. Haljan, D. S. Hall, C. E. Wieman, and E. A. Cornell. *Vortices in a Bose-Einstein condensate*. Phys. Rev. Lett. **83**, 2498–2501 (1999).

[23] K. Madison, F. Chevy, W. Wohlleben, and J. Dalibard. *Vortex formation in a stirred Bose-Einstein condensate*. Phys. Rev. Lett. **84**, 806–809 (2000).

[24] J. R. Abo-Shaeer, C. Raman, J. M. Vogels, and W. Ketterle. *Observation of vortex lattices in Bose-Einstein condensates*. Science **292**, 476–479 (2001).

[25] Y.-J. Lin, R. L. Compton, K. Jiménez-García, J. V. Porto, and I. B. Spielman. *Synthetic magnetic fields for ultracold neutral atoms*. Nature **462**, 628–632 (2009).

[26] N. R. Cooper. *Rapidly rotating atomic gases*. Adv. Phys. **57**, 539–616 (2008).

[27] N. Gemelke, E. Sarajlic, and S. Chu. *Rotating few-body atomic systems in the fractional quantum Hall regime*. arXiv:1007.2677v1 [cond-mat.quant-gas] (2010).

[28] S. Trotzky, P. Cheinet, S. Fölling, M. Feld, U. Schnorrberger, A. M. Rey, A. Polkovnikov, E. A. Demler, M. D. Lukin, and I. Bloch. *Time-resolved observation and control of superexchange interactions with ultracold atoms in optical lattices*. Science **319**, 295–299 (2008).

[29] L.-M. Duan, E. Demler, and M. Lukin. *Controlling spin exchange interactions of ultracold atoms in optical lattices*. Phys. Rev. Lett. **91**, 090402 (2003).

[30] J. Simon, W. S. Bakr, R. Ma, M. E. Tai, P. M. Preiss, and M. Greiner. *Quantum simulation of antiferromagnetic spin chains in an optical lattice*. Nature **472**, 307–312 (2011).

[31] P. Soltan-Panahi, J. Struck, P. Hauke, A. Bick, W. Plenkers, G. Meineke, C. Becker, P. Windpassinger, M. Lewenstein, and K. Sengstock. *Multi-component quantum gases in spin-dependent hexagonal lattices*. Nature Phys. **7**, 434–440 (2011).

[32] A. Gezerlis and J. Carlson. *Strongly paired fermions: Cold atoms and neutron matter*. Phys. Rev. C **77**, 032801(R) (2008).

[33] A. Rapp, G. Zaránd, C. Honerkamp, and W. Hofstetter. *Color superfluidity and 'Baryon' formation in ultracold Fermions*. Phys. Rev. Lett. **98**, 160405 (2007).

[34] R. Blatt and D. Wineland. *Entangled states of trapped atomic ions.* Nature **453**, 1008–1015 (2008).

[35] N. Schlosser, G. Reymond, I. Protsenko, and P. Grangier. *Sub-poissonian loading of single atoms in a microscopic dipole trap.* Nature **411**, 1024–1027 (2001).

[36] R. Scheunemann, F. S. Cataliotti, T. W. Hänsch, and M. Weitz. *Resolving and addressing atoms in individual sites of a CO2-laser optical lattice*. Phys. Rev. A **62**, 051801(R) (2000).

[37] R. Dumke, M. Volk, T. Müther, F. Buchkremer, G. Birkl, and W. Ertmer. *Micro-optical realization of arrays of selectively addressable dipole traps: A scalable configuration for quantum computation with atomic qubits*. Phys. Rev. Lett. **89**, 097903 (2002).

[38] K. D. Nelson, X. Li, and D. S. Weiss. *Imaging single atoms in a three-dimensional array*. Nature Physics **3**, 556–560 (2007).

[39] A. Itah, H. Veksler, O. Lahav, A. Blumkin, C. Moreno, C. Gordon, and J. Steinhauer. *Direct observation of a sub-Poissonian number distribution of atoms in an optical lattice*. Phys. Rev. Lett. **104**, 113001 (2010).

[40] V. Ossadnik. *Direkter Nachweis lichtinduzierter Atomgitter*. PhD thesis, Ludwig-Maximilians-Universität München (1996).

[41] D. Schrader, I. Dotsenko, M. Khudaverdyan, Y. Miroshnychenko, A. Rauschenbeutel, and D. Meschede. *Neutral atom quantum register*. Phys. Rev. Lett. **93**, 150501 (2004).

[42] M. Karski, L. Förster, J. Choi, W. Alt, A. Widera, and D. Meschede. *Nearest-neighbor detection of atoms in a 1D optical lattice by fluorescence imaging*. Phys. Rev. Lett. **102**, 053001 (2009).

[43] T. Gericke, P. Würtz, D. Reitz, T. Langen, and H. Ott. *High-resolution scanning electron microscopy of an ultracold quantum gas*. Nature Phys. **4**, 949–953 (2008).

[44] P. Würtz, T. Langen, T. Gericke, A. Koglbauer, and H. Ott. *Experimental demonstration of single-site addressability in a two-dimensional optical lattice*. Phys. Rev. Lett. **103**, 80404 (2009).

[45] W. S. Bakr, J. I. Gillen, A. Peng, S. Fölling, and M. Greiner. *A quantum gas microscope for detecting single atoms in a Hubbard-regime optical lattice*. Nature **462**, 74–77 (2009).

[46] W. S. Bakr, A. Peng, M. E. Tai, R. Ma, J. Simon, J. I. Gillen, S. Fölling, L. Pollet, and M. Greiner. *Probing the superfluid-to-Mott insulator transition at the single-atom level*. Science **329**, 547–550 (2010).

[47] J. F. Sherson, C. Weitenberg, M. Endres, M. Cheneau, I. Bloch, and S. Kuhr. *Single-atom-resolved fluorescence imaging of an atomic Mott insulator.* Nature **467**, 68–72 (2010).

[48] C. Weitenberg, M. Endres, J. F. Sherson, M. Cheneau, P. Schauß, T. Fukuhara, I. Bloch, and S. Kuhr. *Single-spin addressing in an atomic Mott insulator*. Nature **471**, 319–324 (2011).

[49] C. Deutsch, F. Ramirez-Martinez, C. Lacroûte, F. Reinhard, T. Schneider, J. N. Fuchs, F. Piéchon, F. Laloë, J. Reichel, and P. Rosenbusch. *Spin self-rephasing and very long coherence times in a trapped atomic ensemble*. Phys. Rev. Lett. **105**, 020401 (2010).

[50] M. A. Nielsen and I. L. Chuang. *Quantum Computation and Quantum Information*. Cambridge University Press, Cambridge (2000).

[51] R. Raussendorf and H. J. Briegel. *A one-way quantum computer*. Phys. Rev. Lett. **86**, 5188–5191 (2001).

[52] H. J. Briegel, D. E. Browne, W. Dür, R. Raussendorf, and M. Van Den Nest. *Measurement-based quantum computation*. Nature Phys. **5**, 19–26 (2009).

[53] D. Jaksch, H.-J. Briegel, J. I. Cirac, C. W. Gardiner, and P. Zoller. *Entanglement of atoms via cold controlled collisions*. Phys. Rev. Lett. **82**, 1975–1978 (1999).

[54] O. Mandel, M. Greiner, A. Widera, T. Rom, T. Hänsch, and I. Bloch. *Controlled collisions for multiparticle entanglement of optically trapped atoms*. Nature **425**, 937–940 (2003).

[55] D. Jaksch, J. I. Cirac, P. Zoller, S. L. Rolston, R. Cote, and M. D. Lukin. *Fast quantum gates for neutral atoms*. Phys. Rev. Lett. **85**, 2208–2211 (2000).

[56] T. Wilk, A. Gaetan, C. Evellin, J. Wolters, Y. Miroshnychenko, P. Grangier, and A. Browaeys. *Entanglement of two individual neutral atoms using Rydberg blockade*. Phys. Rev. Lett. **104**, 10502 (2010).

[57] L. Isenhower, E. Urban, X. L. Zhang, A. T. Gill, T. Henage, T. A. Johnson, T. G. Walker, and M. Saffman. *Demonstration of a neutral atom controlled-NOT quantum gate*. Phys. Rev. Lett. **104**, 010503 (2010).

[58] D. Jaksch. *Bose-Einstein condensation and applications*. PhD thesis, Leopold-Franzens-Universität Innsbruck (1999).

[59] W. Zwerger. *Mott-Hubbard transition of cold atoms in optical lattices*. J. Opt. B: Quantum Semiclass. Opt. **5**, 9–16 (2003).

[60] M. Greiner. *Ultracold quantum gases in three-dimensional optical lattice potentials*. PhD thesis, Ludwig-Maximilians-Universität München (2003).

[61] D. Jaksch and P. Zoller. *The cold atom Hubbard toolbox*. Annals Phys. **315**, 52–79 (2005).

[62] S. Fölling. *Probing strongly correlated states of ultracold atoms in optical lattices*. PhD thesis, Johannes-Gutenberg-Universität Mainz (2008).

[63] J. Hubbard. *Electron correlation in narrow energy bands*. Proc. Roy. Soc. A **276**, 238–257 (1963).

[64] M. P. A. Fisher, P. B. Weichman, G. Grinstein, and D. S. Fisher. *Boson localization and the superfluid-insulator transition*. Phys. Rev. B **40**, 546–570 (1989).

[65] S. Will, T. Best, U. Schneider, L. Hackermüller, D.-S. Lühmann, and I. Bloch. *Time-resolved observation of coherent multi-body interactions in quantum phase revivals*. Nature **465**, 197–201 (2010).

[66] W. Krauth and N. Trivedi. *Mott and Superfluid Transitions in a Strongly Interacting Lattice Boson System*. Europhys. Lett. **14**, 627–632 (1991).

[67] M. Rigol, G. G. Batrouni, V. G. Rousseau, and R. T. Scalettar. *State diagrams for harmonically trapped bosons in optical lattices*. Phys. Rev. A **79**, 053605 (2009).

[68] S. Fölling, A. Widera, T. Müller, F. Gerbier, and I. Bloch. *Formation of spatial shell structure in the superfluid to Mott insulator transition*. Phys. Rev. Lett. **97**, 060403 (2006).

[69] M. Anderson, J. R. Ensher, M. R. Matthews, C. E. Wieman, and E. A. Cornell. *Observation of Bose-Einstein condensation in a dilute atomic vapor*. Science **269**, 198–201 (1995).

[70] K. B. Davis, M.-O. Mewes, M. R. Andrews, N. J. van Druten, D. S. Durfee, D. M. Kurn, and W. Ketterle. *Bose-Einstein condensation in a gas of sodium atoms*. Phys. Rev. Lett. **75**, 3969 (1995).

[71] W. Ketterle, D. S. Durfee, and D. M. Stamper-Kurn. *Making, probing and understanding Bose-Einstein condensates*. In M. Inguscio, S. Stringari, and C. E. Wieman, editors, *Bose-Einstein condensates in atomic gases*, pages 67–176, Amsterdam (1999). IOS Press.

[72] T. Rom. *Bosonische und fermionische Quantengase in dreidimensionalen optischen Gittern*. PhD thesis, Ludwig-Maximilians-Universität München (2009).

[73] O. Loesdau. *Aufbau und Charakterisierung eines Doppel-MOT-Systems*. Diploma thesis, Johannes-Gutenberg-Universität Mainz (2008).

[74] C.-L. Hung, X. Zhang, N. Gemelke, and C. Chin. *Accelerating evaporative cooling of atoms into Bose-Einstein condensation in optical traps*. Phys. Rev. A **78**, 011604 (2008).

[75] Y.-J. Lin, A. R. Perry, R. L. Compton, I. B. Spielman, and J. V. Porto. *Rapid production of ^{87}Rb Bose-Einstein condensates in a combined magnetic and optical potential*. Phys. Rev. A **79**, 063631 (2009).

[76] M. Greiner, I. Bloch, T. W. Hänsch, and T. Esslinger. *Magnetic transport of trapped cold atoms over a large distance*. Phys. Rev. A **63**, 031401(R) (2001).

[77] W. Hänsel, J. Reichel, P. Hommelhoff, and T. W. Hänsch. *Magnetic conveyor belt for transporting and merging trapped atom clouds*. Phys. Rev. Lett. **86**, 608–611 (2001).

[78] D. Pertot, D. Greif, S. Albert, B. Gadway, and D. Schneble. *Versatile transporter apparatus for experiments with optically trapped Bose-Einstein condensates*. J. Phys. B: At. Mol. Opt. Phys. **42**, 215305 (2009).

[79] T. L. Gustavson, A. P. Chikkatur, A. E. Leanhardt, A. Görlitz, S. Gupta, D. E. Pritchard, and W. Ketterle. *Transport of Bose-Einstein condensates with optical tweezers*. Phys. Rev. Lett. **88**, 020401 (2002).

[80] A. P. Chikkatur, Y. Shin, A. E. Leanhardt, D. Kielpinski, E. Tsikata, T. L. Gustavson, D. E. Pritchard, and W. Ketterle. *A continuous source of Bose-Einstein condensed atoms*. Science **296**, 2193–2195 (2002).

[81] A. Couvert, T. Kawalec, G. Reinaudi, and D. Guéry-Odelin. *Optimal transport of ultracold atoms in the non-adiabatic regime*. Europhys. Lett. **83**, 13001 (2008).

[82] D. Schrader, S. Kuhr, W. Alt, M. Müller, V. Gomer, and D. Meschede. *An optical conveyor belt for single neutral atoms*. Appl. Phys. B **73**, 819–824 (2001).

[83] S. Schmid, G. Thalhammer, K. Winkler, F. Lang, and J. Hecker Denschlag. *Long distance transport of ultracold atoms using a 1D optical lattice*. New J. Phys. **8**, 159 (2006).

[84] J. Petersen. *Optischer Transport ultrakalter Atome*. Diploma thesis, Johannes-Gutenberg-Universität Mainz (2009).

[85] S. Burger, F. S. Cataliotti, C. Fort, P. Maddaloni, F. Minardi, and M. Inguscio. *Quasi-2D Bose-Einstein condensation in an optical lattice*. Europhys. Lett. **57**, 1–6 (2002).

[86] A. Görlitz, J. M. Vogels, A. E. Leanhardt, C. Raman, T. Gustavson, J. R. Abo-Shaeer, A. P. Chikkatur, S. Gupta, S. Inouye, T. Rosenband, and W. Ketterle. *Realization of Bose-Einstein condensates in lower dimensions*. Phys. Rev. Lett. **87**, 130402 (2001).

[87] N. L. Smith, W. H. Heathcote, G. Hechenblaikner, E. Nugent, and C. J. Foot. *Quasi-2D confinement of a BEC in a combined optical and magnetic potential*. J. Phys. B: At. Mol. Opt. Phys. **38**, 223–235 (2005).

[88] S. P. Rath, T. Yefsah, K. J. Günter, M. Cheneau, R. Desbuquois, M. Holzmann, W. Krauth, and J. Dalibard. *The equilibrium state of a trapped two-dimensional Bose gas*. Phys. Rev. A **82**, 013609 (2010).

[89] D. Rychtarik, B. Engeser, H.-C. Nägerl, and R. Grimm. *Two-dimensional Bose-Einstein condensate in an optical surface trap*. Phys. Rev. Lett. **92**, 173003 (2004).

[90] J. Gillen, W. Bakr, A. Peng, P. Unterwaditzer, S. Fölling, and M. Greiner. *Two-dimensional quantum gas in a hybrid surface trap*. Phys. Rev. A **80**, 021602 (2009).

[91] N. Gemelke, X. Zhang, C.-L. Hung, and C. Chin. *In situ observation of incompressible Mott-insulating domains in ultracold atomic gases*. Nature **460**, 995–998 (2009).

[92] K. Jiménez-Garcia, R. Compton, Y. Lin, W. Phillips, J. Porto, and I. Spielman. *Phases of a two-dimensional Bose gas in an optical lattice*. Phys. Rev. Lett. **105**, 110401 (2010).

[93] M. Karski, L. Förster, J.-M. Choi, A. Steffen, N. Belmechri, W. Alt, D. Meschede, and A. Widera. *Imprinting patterns of neutral atoms in an optical lattice using magnetic resonance techniques*. New J. Phys. **12**, 065027 (2010).

[94] D. A. Steck. *Rubidium 87 D Line Data*. available online at http://steck.us/alkalidata page (revision 2.1.4) (2010).

[95] Y. Miroshnychenko, D. Schrader, S. Kuhr, W. Alt, I. Dotsenko, M. Khudaverdyan, A. Rauschenbeutel, and D. Meschede. *Continued imaging of the transport of a single neutral atom*. Opt. Expr. **11**, 3498–3502 (2003).

[96] I. B. Spielman, W. D. Phillips, and J. V. Porto. *Mott-insulator transition in a two-dimensional atomic Bose gas*. Phys. Rev. Lett. **98**, 080404 (2007).

[97] J. Mun, P. Medley, G. Campbell, L. Marcassa, D. Pritchard, and W. Ketterle. *Phase diagram for a Bose-Einstein condensate moving in an optical lattice*. Phys. Rev. Lett. **99**, 150604 (2007).

[98] S. Fölling, S. Trotzky, P. Cheinet, M. Feld, R. Saers, A. Widera, T. Müller, and I. Bloch. *Direct observation of second-order atom tunnelling*. Nature **448**, 1029–1032 (2007).

[99] B. Zimmermann, T. Müller, J. Meineke, T. Esslinger, and H. Moritz. *High-resolution imaging of ultracold fermions in microscopically tailored optical potentials*. New J. Phys. **13**, 043007 (2011).

[100] M. Born and E. Wolf. *Principles of optics*. Cambridge University Press, Cambridge, 7th ed. edition (1999).

[101] S. Van Aert, K. J. Batenburg, M. D. Rossell, R. Erni, and G. Van Tendeloo. *Three-dimensional atomic imaging of crystalline nanoparticles*. Nature **470**, 374–377 (2011).

[102] E. Brainis, C. Muldoon, L. Brandt, and A. Kuhn. *Coherent imaging of extended objects*. Opt. Comm. **282**, 465–472 (2009).

[103] R. Gloeckner. *Ortsaufgelöster Nachweis ultrakalter Atome in einem optischen Gitter*. Diploma thesis, Johannes-Gutenberg-Universität Mainz (2010).

[104] H. F. Talbot. *Facts relating to optical science*. No. IV, Phil. Mag. **9**, 401 (1836).

[105] W. D. Montgomery. *Algebraic formulation of diffraction applied to self imaging*. J. Opt. Soc. Am. **58**, 1112–1124 (1968).

[106] M. T. DePue, C. McCormick, S. L. Winoto, S. Oliver, and D. S. Weiss. *Unity occupation of sites in a 3D optical lattice*. Phys. Rev. Lett. **82**, 2262–2265 (1999).

[107] T. Grünzweig, A. Hilliard, M. McGovern, and M. F. Andersen. *Near-deterministic preparation of a single atom in an optical microtrap*. Nature Phys. **6**, 951–954 (2010).

[108] C. Valentin, M.-C. Gagné, J. Yu, and P. Pillet. *One-dimension sub-Doppler molasses in the presence of static magnetic field*. Europhys. Lett. **17**, 133–138 (1992).

[109] D. Boiron, C. Triché, D. R. Meacher, P. Verkerk, and G. Grynberg. *Three-dimensional cooling of cesium atoms in four-beam gray optical molasses*. Phys. Rev. A **52**, R3425 (1995).

[110] S. Al-Assam, R. Williams, and C. Foot. *Ultracold atoms in an optical lattice with dynamically variable periodicity*. Phys. Rev. A **82**, 021604(R) (2010).

[111] M. D. Shotter. *Design of a technique to measure the density of ultracold atoms in a short-period optical lattice in three dimensions with single-atom sensitivity*. Phys. Rev. A **83**, 033617 (2011).

[112] S. Wolf, S. J. Oliver, and D. S. Weiss. *Suppression of recoil heating by an optical lattice*. Phys. Rev. Lett. **85**, 4249–4252 (2000).

[113] J. Barth. *Transport of adsorbates at metal surfaces: from thermal migration to hot precursors*. Surf. Sci. Rep. **40**, 75–149 (2000).

[114] T. Tansel and O. Magnussen. *Video STM studies of adsorbate diffusion at electrochemical interfaces*. Phys. Rev. Lett. **96**, 026101 (2006).

[115] J. Dalibard and C. Cohen-Tannoudji. *Laser cooling below the Doppler limit by polarization gradients: simple theoretical models*. J. Opt. S. Am. B **6**, 2023–2045 (1989).

[116] C. Salomon, J. Dalibard, W. D. Phillips, A. Clairon, and S. Guellati. *Laser cooling of cesium atoms below 3 μK*. Europhys. Lett. **12**, 683–688 (1990).

[117] A. M. Steane and C. J. Foot. *Laser cooling below the Doppler limit in a magneto-optical trap*. Europhys. Lett. **14**, 231–236 (1991).

[118] P. D. Lett, W. D. Phillips, S. L. Rolston, C. E. Tanner, R. N. Watts, and C. I. Westbrook. *Optical molasses*. J. Opt. Soc. Am. B **6**, 2084–2107 (1989).

[119] A. Kuklov and B. Svistunov. *Counterflow superfluidity of two-species ultracold atoms in a commensurate optical lattice*. Phys. Rev. Lett. **90**, 100401 (2003).

[120] I. Spielman, W. Phillips, and J. Porto. *Condensate fraction in a 2D Bose gas measured across the Mott-insulator transition*. Phys. Rev. Lett. **100**, 120402 (2008).

[121] T. Stöferle, H. Moritz, C. Schori, M. Köhl, and T. Esslinger. *Transition from a strongly interacting 1D superfluid to a Mott insulator*. Phys. Rev. Lett. **92**, 130403 (2004).

[122] F. Gerbier, S. Fölling, A. Widera, O. Mandel, and I. Bloch. *Probing number squeezing of ultracold atoms across the superfluid-Mott insulator transition*. Phys. Rev. Lett. **96**, 090401 (2006).

[123] P. Cheinet, S. Trotzky, M. Feld, U. Schnorrberger, M. Moreno-Cardoner, S. Fölling, and I. Bloch. *Counting atoms using interaction blockade in an optical superlattice*. Phys. Rev. Lett. **101**, 090404 (2008).

[124] G. K. Campbell, J. Mun, M. Boyd, P. Medley, A. E. Leanhardt, L. Marcassa, D. Pritchard, and W. Ketterle. *Imaging the Mott insulator shells by using atomic clock shifts*. Science **313**, 649–652 (2006).

[125] J. Mun. *Bose-Einstein condensates in optical lattices : The superfluid to Mott insulator phase transition*. PhD thesis, Massachusetts Institute of Technology (2008).

[126] C.-L. Hung, X. Zhang, N. Gemelke, and C. Chin. *Slow mass transport and statistical evolution of an atomic gas across the superfluid-Mott-insulator transition*. Phys. Rev. Lett. **104**, 160403 (2010).

[127] S. Wessel. *Critical entropy of quantum Heisenberg magnets on simple-cubic lattices*. Phys. Rev. B **81**, 052405 (2010).

[128] B. Capogrosso-Sansone, S. G. Soeyler, N. V. Prokofev, and B. V. Svistunov. *Critical entropies for magnetic ordering in bosonic mixtures on a lattice*. Phys. Rev. A **81**, 053622 (2010).

[129] S. Trotzky, L. Pollet, F. Gerbier, U. Schnorrberger, I. Bloch, N. V. Prokofev, B. Svistunov, and M. Troyer. *Suppression of the critical temperature for superfluidity near the Mott transition*. Nature Phys. **6**, 998–1004 (2010).

[130] R. Jördens, L. Tarruell, D. Greif, T. Uehlinger, N. Strohmaier, H. Moritz, T. Esslinger, L. De Leo, C. Kollath, A. Georges, V. Scarola, L. Pollet, E. Burovski, E. Kozik, and M. Troyer. *Quantitative determination of temperature in the approach to magnetic order of ultracold Fermions in an optical lattice*. Phys. Rev. Lett. **104**, 180401 (2010).

[131] F. Gerbier. *Boson Mott insulators at finite temperatures*. Phys. Rev. Lett. **99**, 120405 (2007).

[132] M. Saffman. *Addressing atoms in optical lattices with Bessel beams*. Opt. Lett. **29**, 1016–1018 (2004).

[133] J. Joo, Y. L. Lim, A. Beige, and P. L. Knight. *Single-qubit rotations in two-dimensional optical lattices with multiqubit addressing*. Phys. Rev. A **74**, 042344 (2006).

[134] J. Cho. *Addressing individual atoms in optical lattices with standing-wave driving fields*. Phys. Rev. Lett. **99**, 020502 (2007).

[135] A. V. Gorshkov, L. Jiang, M. Greiner, P. Zoller, and M. D. Lukin. *Coherent quantum optical control with subwavelength resolution*. Phys. Rev. Lett. **100**, 093005 (2008).

[136] S. W. Hell and J. Wichmann. *Breaking the diffraction resolution limit by stimulated emission: stimulated-emission-depletion fluorescence microscopy*. Opt. Lett. **19**, 780–782 (1994).

[137] L. You and M. Chapman. *Quantum entanglement using trapped atomic spins*. Phys. Rev. A **62**, 052302 (2000).

[138] T. Calarco, U. Dorner, P. S. Julienne, C. J. Williams, and P. Zoller. *Quantum computations with atoms in optical lattices: Marker qubits and molecular interactions*. Phys. Rev. A **70**, 012306 (2004).

[139] N. Lundblad, J. M. Obrecht, I. B. Spielman, and J. V. Porto. *Field-sensitive addressing and control of field-insensitive neutral-atom qubits*. Nature Phys. **5**, 575–580 (2009).

[140] D. Weiss, J. Vala, A. Thapliyal, S. Myrgren, U. Vazirani, and K. Whaley. *Another way to approach zero entropy for a finite system of atoms*. Phys. Rev. A **70**, 40302 (2004).

[141] C. Zhang, S. L. Rolston, and S. Das Sarma. *Manipulation of single neutral atoms in optical lattices*. Phys. Rev. A **74**, 042316 (2006).

[142] K. Shibata, S. Kato, A. Yamaguchi, S. Uetake, and Y. Takahashi. *A scalable quantum computer with ultranarrow optical transition of ultracold neutral atoms in an optical lattice*. Appl. Phys. B **97**, 753–758 (2009).

[143] M. Garwood and L. DelaBarre. *The return of the frequency sweep: Designing adiabatic pulses for contemporary NMR*. J. Magn. Reson. **153**, 155–177 (2001).

[144] S. Kuhr, W. Alt, D. Schrader, M. Müller, V. Gomer, and D. Meschede. *Deterministic delivery of a single atom.* Science **293**, 278–280 (2001).

[145] R. Labouvie. *Parametrisches Heizen in optischen Gittern und Charakterisierung eines akusto-optischen Deflektors für die Erzeugung von zeitgemittelten Potentialen*. Diploma thesis, Johannes-Gutenberg-Universität Mainz (2010).

[146] F. K. Fatemi, M. Bashkansky, and Z. Dutton. *Dynamic high-speed spatial manipulation of cold atoms using acousto-optic and spatial light modulation*. Opt. Expr. **15**, 3589–3596 (2007).

[147] S. K. Schnelle, E. D. van Ooijen, M. J. Davis, N. R. Heckenberg, and H. Rubinsztein-Dunlop. *Versatile two-dimensional potentials for ultra-cold atoms*. Opt. Expr. **16**, 159–165 (2008).

[148] K. Henderson, C. Ryu, C. MacCormick, and M. G. Boshier. *Experimental demonstration of painting arbitrary and dynamic potentials for Bose-Einstein condensates*. New J. Phys. **11**, 043030 (2009).

[149] W. Dür, R. Raussendorf, V. Kendon, and H.-J. Briegel. *Quantum walks in optical lattices*. Phys. Rev. A **66**, 052319 (2002).

[150] J. Kempe. *Quantum random walks: an introductory overview*. Contemp. Phys. **44**, 307–327 (2003).

[151] V. I. V. Kendon. *Decoherence in quantum walks - a review*. Mathematical Structures in Computer Science **17**, 1169–1220 (2007).

[152] A. Childs. *Universal computation by quantum walk*. Phys. Rev. Lett. **102**, 180501 (2009).

[153] M. Hillery, D. Reitzner, and V. Bužek. *Searching via walking: How to find a marked clique of a complete graph using quantum walks*. Phys. Rev. A **81**, 062324 (2010).

[154] J. Du, H. Li, X. Xu, M. Shi, J. Wu, X. Zhou, and R. Han. *Experimental implementation of the quantum random-walk algorithm*. Phys. Rev. A **67**, 042316 (2003).

[155] C. A. Ryan, M. Laforest, J. C. Boileau, and R. Laflamme. *Experimental implementation of a discrete-time quantum random walk on an NMR quantum-information processor*. Phys. Rev. A **72**, 062317 (2005).

[156] D. Bouwmeester, I. Marzoli, G. P. Karman, W. Schleich, and J. P. Woerdman. *Optical Galton board*. Phys. Rev. A **61**, 013410 (1999).

[157] B. Do, M. L. Stohler, S. Balasubramanian, D. S. Elliott, C. Eash, E. Fischbach, M. A. Fischbach, A. Mills, and B. Zwickl. *Experimental realization of a quantum quincunx by use of linear optical elements*. J. Opt. Soc. Am. B **22**, 499 (2005).

[158] A. Schreiber, K. N. Cassemiro, V. Potoček, A. Gábris, P. J. Mosley, E. Andersson, I. Jex, and C. Silberhorn. *Photons walking the line: A quantum walk with adjustable coin operations*. Phys. Rev. Lett. **104**, 050502 (2010).

[159] H. B. Perets, Y. Lahini, F. Pozzi, M. Sorel, R. Morandotti, and Y. Silberberg. *Realization of quantum walks with negligible decoherence in waveguide lattices*. Phys. Rev. Lett. **100**, 170506 (2008).

[160] A. Peruzzo, M. Lobino, J. C. F. Matthews, N. Matsuda, A. Politi, K. Poulios, X.-Q. Zhou, Y. Lahini, N. Ismail, K. Wörhoff, Y. Bromberg, Y. Silberberg, M. G. Thompson, and J. L. OBrien. *Quantum walks of correlated photons*. Science **329**, 1500–1503 (2010).

[161] H. Schmitz, R. Matjeschk, C. Schneider, J. Glueckert, M. Enderlein, T. Huber, and T. Schaetz. *Quantum walk of a trapped ion in phase space*. Phys. Rev. Lett. **103**, 090504 (2009).

[162] F. Zähringer, G. Kirchmair, R. Gerritsma, E. Solano, R. Blatt, and C. F. Roos. *Realization of a quantum walk with one and two trapped ions*. Phys. Rev. Lett. **104**, 100503 (2010).

[163] M. Karski, L. Förster, J.-M. Choi, A. Steffen, W. Alt, D. Meschede, and A. Widera. *Quantum walk in position space with single optically trapped atoms*. Science **325**, 174–177 (2009).

[164] U. Schneider, L. Hackermüller, J. P. Ronzheimer, S. Will, S. Braun, T. Best, I. Bloch, E. Demler, S. Mandt, D. Rasch, and A. Rosch. *Breakdown of diffusion: From collisional hydrodynamics to a continuous quantum walk in a homogeneous Hubbard model*. arXiv:1005.3545v1 [cond-mat.quant-gas] (2010).

[165] C. Weitenberg, P. Schauß, T. Fukuhara, M. Cheneau, M. Endres, I. Bloch, and S. Kuhr. *Coherent light scattering from a two-dimensional Mott insulator*. Phys. Rev. Lett. **106**, 215301 (2011).

[166] J. Javanainen and J. Ruostekoski. *Optical detection of fractional particle number in an atomic Fermi-Dirac gas*. Phys. Rev. Lett. **91**, 150404 (2003).

[167] I. de Vega, J. I. Cirac, and D. Porras. *Detection of spin correlations in optical lattices by light scattering*. Phys. Rev. A **77**, 051804(R) (2008).

[168] K. Eckert, O. Romero-Isart, M. Rodriguez, M. Lewenstein, E. S. Polzik, and A. Sanpera. *Quantum non-demolition detection of strongly correlated systems*. Nature Phys. **4**, 50–54 (2007).

[169] J. Douglas and K. Burnett. *Quantum imaging of spin states in optical lattices*. Phys. Rev. A **82**, 033434 (2010).

[170] T. A. Corcovilos, S. K. Baur, J. M. Hitchcock, E. J. Mueller, and R. G. Hulet. *Detecting antiferromagnetism of atoms in an optical lattice via optical Bragg scattering*. Phys. Rev. A **81**, 013415 (2010).

[171] J. Ruostekoski, C. J. Foot, and A. B. Deb. *Light scattering for thermometry of Fermionic atoms in an optical lattice*. Phys. Rev. Lett. **103**, 170404 (2009).

[172] I. B. Mekhov, C. Maschler, and H. Ritsch. *Light Scattering from ultracold atoms in optical lattices as an optical probe of quantum statistics*. Phys. Rev. A **76**, 053618 (2007).

[173] K. Lakomy, Z. Idziaszek, and M. Trippenbach. *Thermal effects in light scattering from ultracold bosons in an optical lattice*. Phys. Rev. A **80**, 043404 (2009).

[174] S. Rist, C. Menotti, and G. Morigi. *Light scattering by ultracold atoms in an optical lattice*. Phys. Rev. A **81**, 013404 (2010).

[175] I. B. Mekhov, C. Maschler, and H. Ritsch. *Probing quantum phases of ultracold atoms in optical lattices by transmission spectra in cavity quantum electrodynamics*. Nature Phys. **3**, 319–323 (2007).

[176] W. Chen, D. Meiser, and P. Meystre. *Cavity QED determination of atomic number statistics in optical lattices*. Phys. Rev. A **75**, 023812 (2007).

[177] G. Birkl, M. Gatzke, I. H. Deutsch, S. L. Rolston, and W. D. Phillips. *Bragg scattering from atoms in optical lattices*. Phys. Rev. Lett. **75**, 2823–2826 (1995).

[178] M. Weidemüller, A. Hemmerich, A. Görlitz, T. Esslinger, and T. Hänsch. *Bragg diffraction in an atomic lattice bound by light*. Phys. Rev. Lett. **75**, 4583–4586 (1995).

[179] M. Weidemüller, A. Görlitz, T. W. Hänsch, and A. Hemmerich. *Local and global properties of light-bound atomic lattices investigated by Bragg diffraction*. Phys. Rev. A **58**, 4647–4661 (1998).

[180] C. I. Westbrook, C. Jurczak, G. Birkl, B. Desruelle, W. D. Phillips, and A. Aspect. *A study of atom localization in an optical lattice by analysis of the scattered light*. J. Mod. Opt. **44**, 1837–1851 (1997).

[181] G. Raithel, G. Birkl, A. Kastberg, W. D. Phillips, and S. L. Rolston. *Cooling and Localization Dynamics in Optical Lattices*. Phys. Rev. Lett. **78**, 630–633 (1997).

[182] S. Slama, C. von Cube, B. Deh, A. Ludewig, C. Zimmermann, and P. Courteille. *Phase-sensitive detection of Bragg scattering at 1D optical lattices*. Phys. Rev. Lett. **94**, 193901 (2005).

[183] N. W. Ashcroft and N. D. Mermin. *Solid State Physics*. Saunders, Philadelphia (1976).

[184] B. R. Mollow. *Power spectrum of light scattered by two-level systems*. Phys. Rev. **188**, 1969–1975 (1969).

[185] E. Kapit and E. Mueller. *Even-odd correlation functions on an optical lattice*. Phys. Rev. A **82**, 013644 (2010).

[186] D. Chen, M. White, C. Borries, and B. DeMarco. *Quantum quench of an atomic Mott insulator*. Phys. Rev. Lett. **106**, 235304 (2011).

[187] J. Friedel. *Metallic alloys*. Il Nuovo Cimento **7**, 287 (1958).

[188] F. Gleisberg, W. Wonneberger, U. Schlöder, and C. Zimmermann. *Noninteracting fermions in a one-dimensional harmonic atom trap: Exact one-particle properties at zero temperature*. Phys. Rev. A **62**, 063602 (2000).

[189] S. N. Artemenko, G. Xianlong, and W. Wonneberger. *Friedel oscillations in a gas of interacting one-dimensional fermionic atoms confined in a harmonic trap*. J. Phys. B: At. Mol. Opt. Phys. **37**, S49–S58 (2004).

[190] A. Recati, P. O. Fedichev, W. Zwerger, and P. Zoller. *Spin-charge separation in ultracold quantum gases*. Phys. Rev. Lett. **90**, 020401 (2003).

[191] A. Kleine, C. Kollath, I. P. McCulloch, T. Giamarchi, and U. Schollwöck. *Spin-charge separation in two-component Bose gases*. Phys. Rev. A **77**, 13607 (2008).

[192] M. B. Zvonarev, V. V. Cheianov, and T. Giamarchi. *Spin dynamics in a one-dimensional ferromagnetic Bose gas*. Phys. Rev. Lett. **99**, 240404 (2007).

[193] K. Winkler, G. Thalhammer, F. Lang, R. Grimm, J. Hecker Denschlag, A. J. Daley, A. Kantian, H. P. Büchler, and P. Zoller. *Repulsively bound atom pairs in an optical lattice*. Nature **441**, 853–856 (2006).

[194] A. Micheli, A. J. Daley, D. Jaksch, and P. Zoller. *Single atom transistor in a 1D optical lattice*. Phys. Rev. Lett. **93**, 140408 (2004).

[195] J. F. Sherson and K. Mø lmer. *Shaking the entropy out of a lattice: atomic filtering by vibrational excitations*. arXiv:1012.1457v1 (2010).

[196] G. Pupillo, A. Micheli, M. Boninsegni, I. Lesanovsky, and P. Zoller. *Strongly correlated gases of Rydberg-dressed atoms: Quantum and classical dynamics*. Phys. Rev. Lett. **104**, 223002 (2010).

[197] T. Pohl, E. Demler, and M. D. Lukin. *Dynamical crystallization in the dipole blockade of ultracold atoms*. Phys. Rev. Lett. **104**, 043002 (2010).

[198] S. Bergamini, B. Darquié, M. Jones, L. Jacubowiez, A. Browaeys, and P. Grangier. *Holographic generation of microtrap arrays for single atoms by use of a programmable phase modulator*. J. Opt. Soc. Am. B **21**, 1889–1894 (2004).

[199] J. Liang, R. N. Kohn, M. F. Becker, and D. J. Heinzen. *High-precision laser beam shaping using a binary-amplitude spatial light modulator*. Appl. Opt. **49**, 1323–1330 (2010).

[200] J. F. S. Brachmann, W. S. Bakr, J. Gillen, A. Peng, and M. Greiner. *Inducing vortices in a Bose-Einstein condensate using holographically produced light beams*. Opt. Expr. **19**, 12984–12991 (2011).

[201] R. Shen, L. B. Shao, B. Wang, and D. Y. Xing. *Single Dirac cone with a flat band touching on line-centered-square optical lattices*. Phys. Rev. B **81**, 041410(R) (2010).

[202] M. Piraud, A. Aspect, and L. Sanchez-Palencia. *Anderson localization of matter waves in tailored disordered potentials*. arXiv:1104.2314v1 [cond-mat.quant-gas] (2011).